SLIDING VANE PUMP SHAFT STRUCTURAL RESPONSE AND INTERMITTENT FAILURE INVESTIGATION

By

STEPHEN SEYMOUR

Bachelor of Science in Mechanical Engineering Technology

Oklahoma State University

Stillwater, Oklahoma

2000

Submitted to the Faculty of the
Graduate College of the
Oklahoma State University
in partial fulfillment of
the requirements for
the Degree of
MASTER OF SCIENCE
May, 2009

SLIDING VANE PUMP SHAFT STRUCTURAL

RESPONSE AND INTERMITTENT

FAILURE INVESTIGATION

Thesis Approved:

Dr. J. K. Good

Thesis Adviser

Dr. Hongbing Lu

Dr. Andy Arena

Dr. A. Gordon Emslie

Dean of the Graduate College

ACKNOWLEDGMENTS

I would like to express my appreciation to Corken for providing both the opportunity and resources for this thesis project. Without Corken's generosity none of this would have been possible. I would also like to extend a special thank you to Ronnie Williamson of Corken. Ronnie's tireless commitment to providing assistance throughout the course of this project was essential to the overall efficiency and was well appreciated.

I would like to thank my Dad, Michael Seymour, for his never-ending support throughout both my academic and professional careers. Throughout my life he has provided me the right amounts of support and freedom, which has enabled me to grow into the person that I am today. His encouragement and interest in all that I do serve as the motivating force behind my desire to make him proud.

Finally, words simply cannot express my love and appreciation for my wife, Toni Seymour. Toni has not only supported me in all of my academic endeavors, but she has sacrificed much to allow me the opportunity to pursue my educational and professional goals. Without Toni's unrelenting support dating back to the days when we met in college absolutely none of this would have been possible. Toni is the mother of our handsome son Logan and our soon to be born son Lucas. Her overwhelming devotion and dedication is matched only by the kindness of her heart. To Toni I owe all of my success, devotion, and love.

TABLE OF CONTENTS

Chapter Page

LIST OF TABLES

Table Page

LIST OF FIGURES

Figure Page

Figure Page

CHAPTER I

INTRODUCTION

The positive displacement swept vane rotary pump is a common design used in industry today to transport a variety of fluids from one location to another. Specifically, the swept vane pump is a popular design choice among the Liquefied Petroleum Gas (LPG) market where the most common fluids pumped are propane, butane, and anhydrous ammonia. Figure 1.1 provides an illustrative cross section of the typical swept vane rotary pump. Commonly a swept vane pump is comprised of a pump case, cam profile either integral to case or as a separate component, an internal safety relief valve, bearings, seals, rotor, vanes, and shaft.

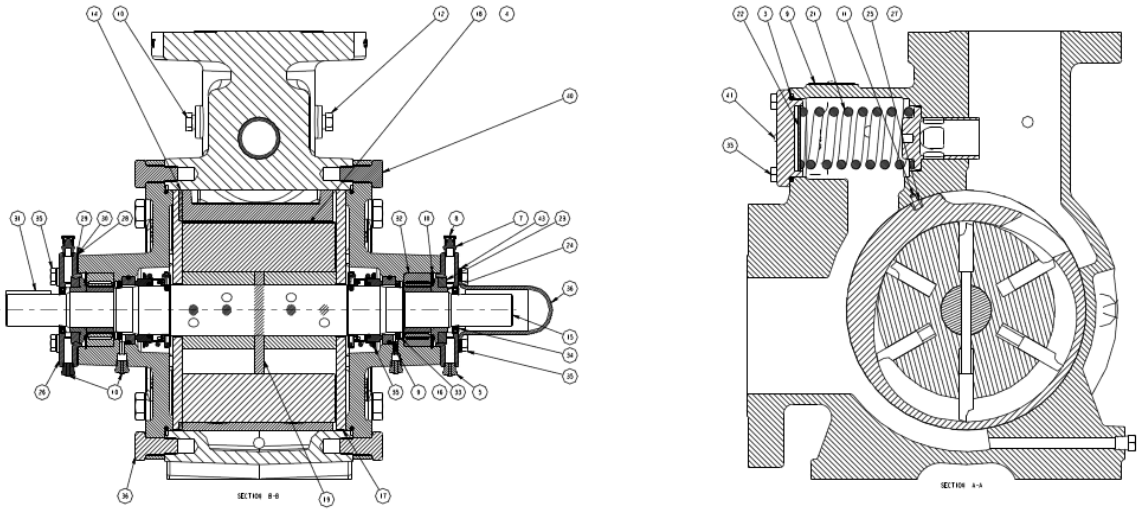

Figure 1.1: Cross Sectional Views of Typical Swept Vane Pump Assembly

Due to the volatile nature of fluids within the LPG market place, leaks must be kept to a minimum. The common sealing method for most swept vane positive displacement pumps is the mechanical seal. The mechanical seal is comprised mainly of a carbon ring that rotates with the pump rotor/shaft and a polished metalic or ceramic ring that remains static. The synchronous rotation of the carbon ring with the pump shaft/rotor is accomplished via a seal drive pin that is press fit into the pump shaft as shown in Figure 1.2.

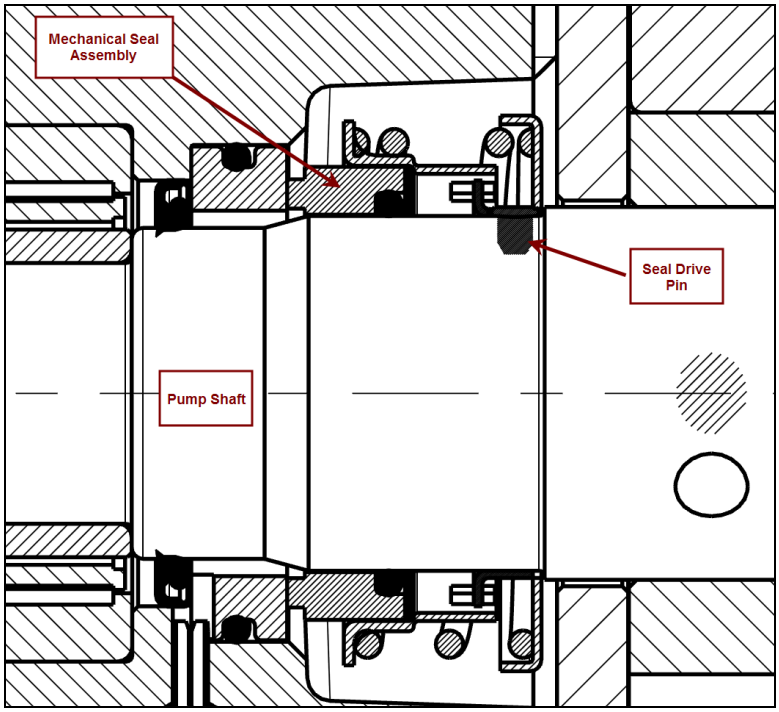

Figure 1.2: Cross Sectional View of Mechanical Seal Assembly

Corken, Inc. of Oklahoma City, Oklahoma is manufacturer of pumps and compressors for the LPG market. Corken, Inc. manufactures a variety of swept vane rotary pumps ranging from small propane pumps used for bottle filling applications to large four inch ASME flange pumps that are used for bulk transfers. For decades Corken

has had to deal with intermittent failures of the pump shafts on the large pump models within its offering. Some of the intermittent failures of the pumps shafts were obvious cases of overload stemming from excessive rotational speed or discharge pressure, while others were ingestion of foreign debris. However, several of the intermittent pump shaft failures over the years occurred in applications where the pump had been operated at or below the recommended discharge pressure and rotational speed, where no presence of foreign debris was found, and had occurred within the standard 12 month warranty period.

Various hypotheses had been made throughout the years regarding the root cause of the pump shaft failures. Some of the more common theories behind the failures were: machining defects during the manufacturing process, material property variation, misalignment errors during initial assembly or repair. However, no substantial proof was ever given indicating any of the various proposed processing or material errors contributed to the overall failure of the pump shaft. Thus, the intermittent failures continued for years without any real understanding as to the root cause behind the failures.

The typical response to an intermittent pump shaft failure by Corken was to replace the failed pump with a newly manufactured pump of the same make and model. In the majority of instances where this replacement occurred the pump shaft failure was never repeated. This lack of repeatability with respect to the pump shaft failure only served to reinforce the intermittent nature of the pump shaft failures.

An examination into past design changes pertaining to the pump shafts revealed that originally the pump shafts were constructed of AISI 1144 stress relieved steel. After

some unknown quantity of failures, the material for these pumps shafts was changed to heat treated AISI 8620 steel. This change to the material constructions of the pump shaft was made during 1995 and all subsequent large swept vane pump designs utilized the heat treated AISI 8620 as the material of construction for the pumps shaft. While this material change may have addressed a subset of the pump shaft failures at the time, intermittent failures continued to occur and still occur in systems operating under normal conditions.

Figure 1.3 through 1.5 are photographs of the typical fracture surface associated with an intermittent pump shaft failure. The fracture surfaces exhibit signs of fatigue failure given the relatively smooth fracture surface and the relatively small final rupture zone. Many of the fractures surfaces were found to pass through or very near the seal drive pin hole that is drilled radially into the shaft. However, the question still remains regarding what are the specific conditions that lead to the intermittent failure of these pump shafts.

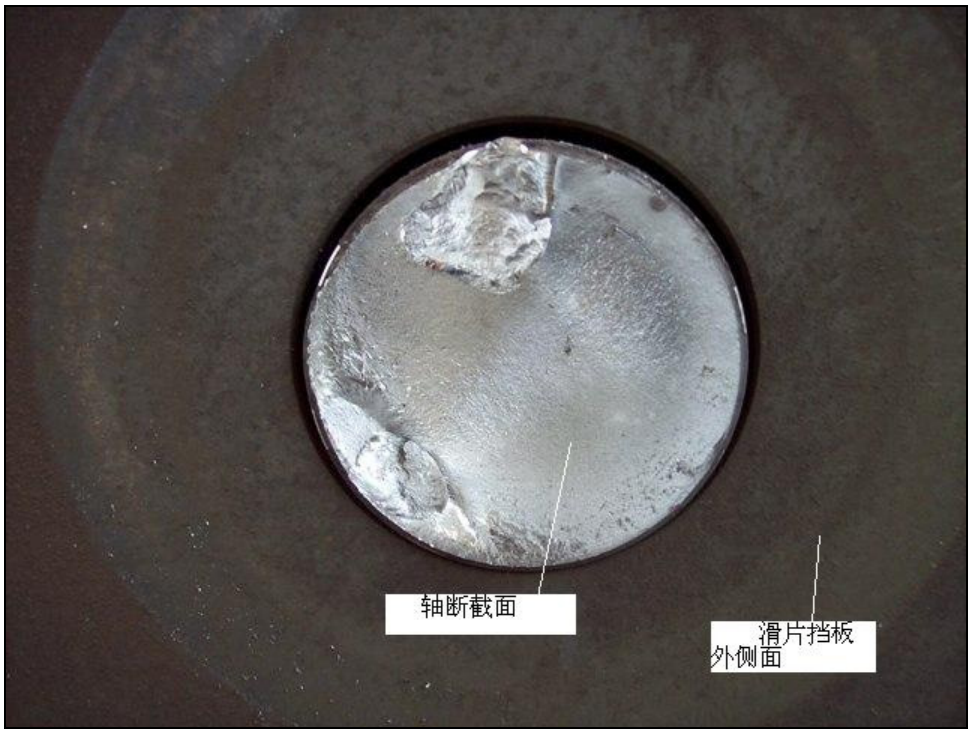

Figure 1.3: Photograph of Typical Pump Fracture Surface Rotor Side

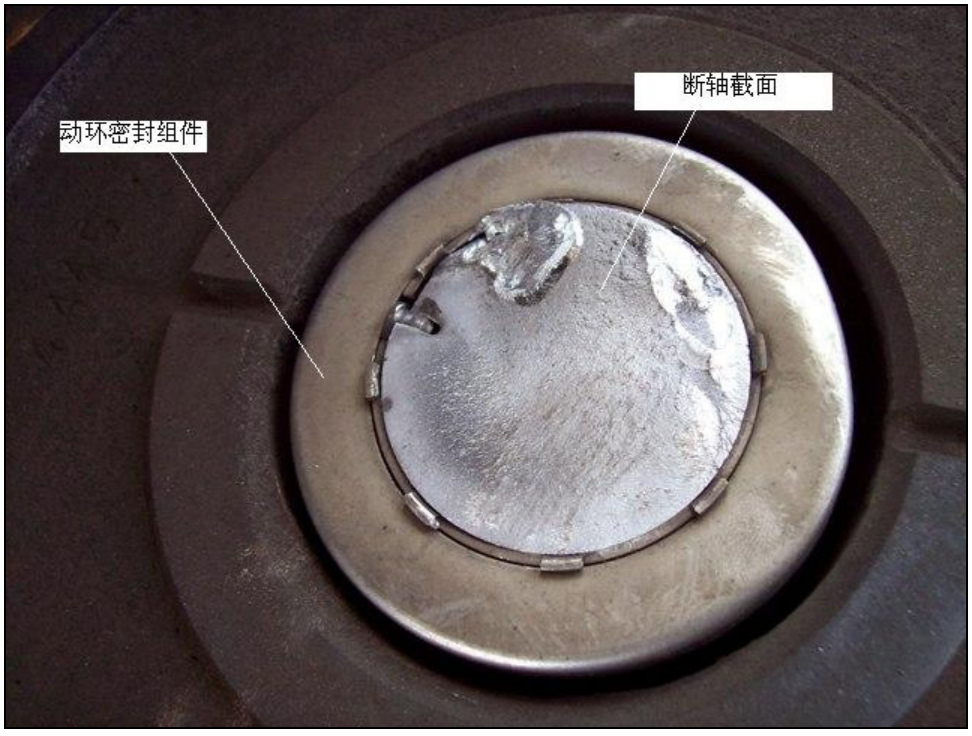

Figure 1.4: Photograph of Typical Pump Fracture Surface Motor Side

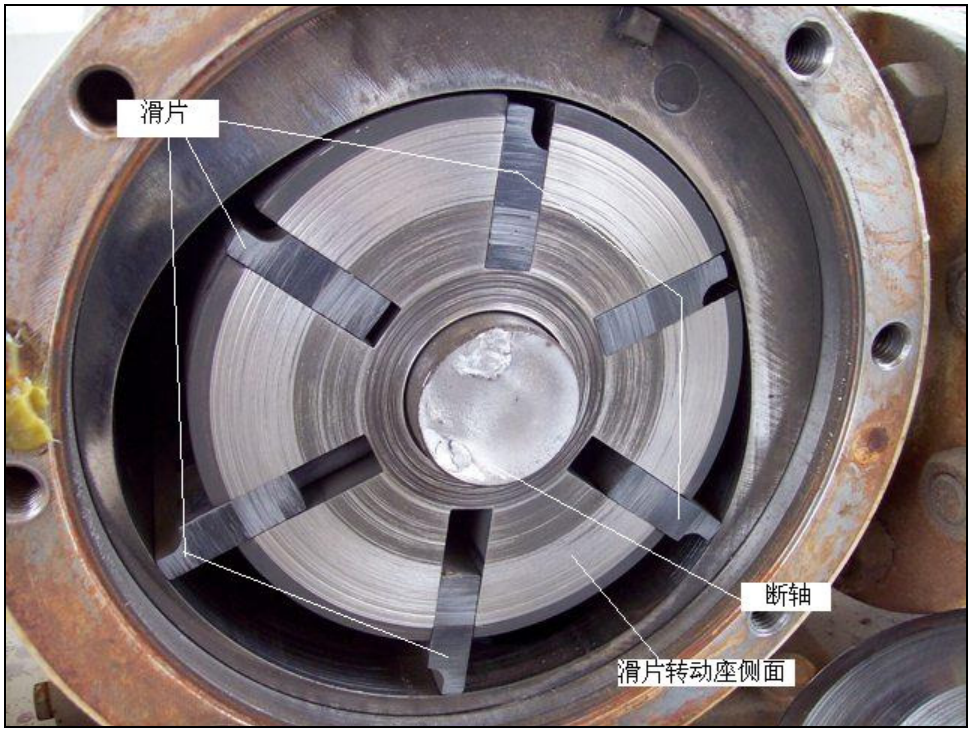

Figure 1.5: Photograph of Typical Pump Fracture Surface Rotor Side

CHAPTER II

REVIEW OF LITERATURE

2.1 Failure Investigations

Throughout the years numerous failure studies have been conducted regarding the fatigue failure of shafts in rotating and power transmission equipment. Berndt and van Bennekom published a compendium of failure studies specifically dealing with pump shaft failures stemming from both corrosion and fatigue [1]. Their analysis attributed the mechanical fatigue failure of the pumps shafts to stress concentrations on the outer surface of the shafts. However, they concluded that these stress concentrations could be the product of geometrical features such as keyways, corrosion pits, or a combination thereof. Figure 2.1 shows a picture of the fracture surface of a pump shaft that began at the corner of a key way slot. It can be seen from the picture shown in Figure 2.1 that the crack was initiated near the keyway and was subject to moderately high stresses due to the relatively large final rupture zone labeled "f" in the picture.

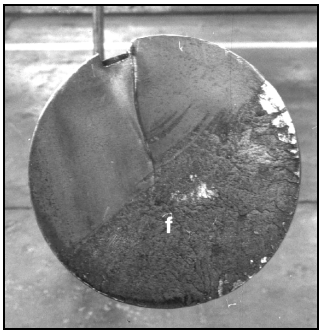

Figure 2.1: Photograph of Shaft Failure Originating at Shaft Keyway

While many shaft failures of rotating equipment can be attributed to stress concentrations arising out of geometrical features or corrosion pitting, some fatigue failures are due to other conditions such as overloading and wear. Xiaolei and Zhiwei conducted a failure analysis of a shaft used in a locomotive turbocharger [2], which a picture of the fracture surface is shown in Figure 2.2. Their study concluded that rotating bending failure was the dominant failure mode stemming from an excessive radial load due to abnormal operation of the locomotive turbocharger. In addition, they also concluded that the failure of the shaft was worsened by large amounts of wear and mechanical damage to the outer journal surfaces of the shaft due to the excessively high radial loads.

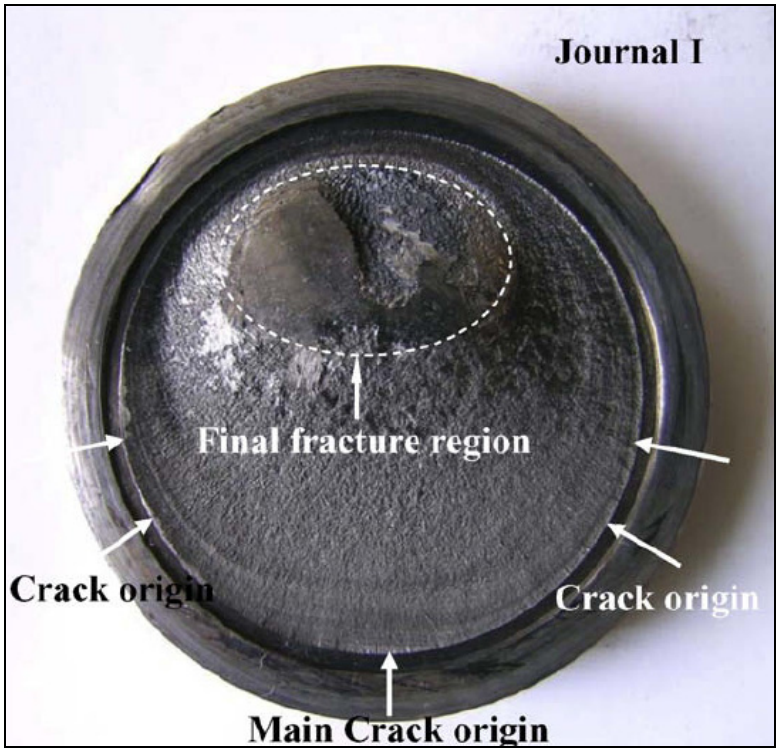

Figure 2.2: Photograph of Diesel Turbo Charger Shaft Fracture

However, not all shaft failures stemming from wear and friction are the result of geometrical stress concentrations on the outer circumference due to scoring or other types of mechanical damage. Lancha, Serrano, and Gomez Briceno [3] conducted a failure analysis of a condensate pump shaft pictured in Figure 2.3 where the material located on the outer surface of the shaft was embrittled via thermal cycling due to friction from a failed shaft sleeve. The shaft sleeve was to serve as a protective barrier between the pump shaft outer surface and a bronze bearing. However, when the protective sleeve seized and relative motion began to occur between the sleeve and the pump shaft large amounts of friction began to occur, which subsequently generated a significant amount of heat. Periodic operational use of the pump resulted in thermal cycling on the outer surface of the shaft, which subsequently resulted in hardening of the shaft surface, grain growth, and the formation of subsurface cracks shown in Figure 2.4. The subsurface cracks and the reduced ductility served to facilitate intergranular crack growth until the crack front approached the more ductile center of the shaft where the crack growth became more transgranular in nature.

Figure 2.3: Photograph of Nuclear Power Plant Pump Shaft Fracture

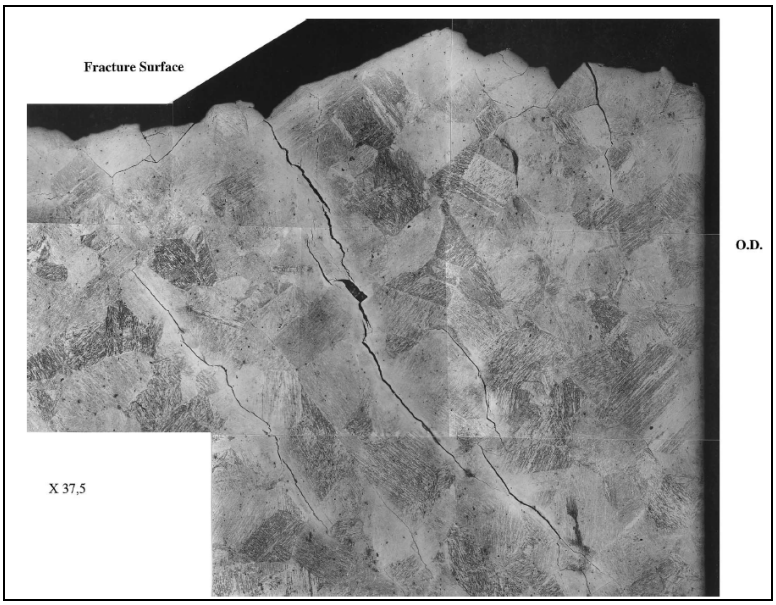

Figure 2.4: Photograph of Subsurface Cracks Due to Heat From Friction

It is well known that manufacturing defects such as poor surface finish, improperly machined rounds or chamfers, and internal voids stemming from porosity can serve as stress concentrations to both initiate and propagate a material crack. However, incorrect heat treatment can also serve as a mechanism to facilitate fatigue failure. Lancha, Serrano, and Gomez Briceno [4] conducted a failure study on a nuclear power plant water pump shaft failure operating under normal conditions that failed in a mode of rotating bending. According to their study, incorrect heat treatment of the AISI 410 stainless steel pump shaft lead to a condition known as temper embrittlement, which created subsurface intergranular cracks as shown in Figure 2.5. These internal cracks, which were primarily located near the outer diameter of the shaft, served as sites from which cracks could grow and propagate even though the pump shaft was operating under normal conditions.

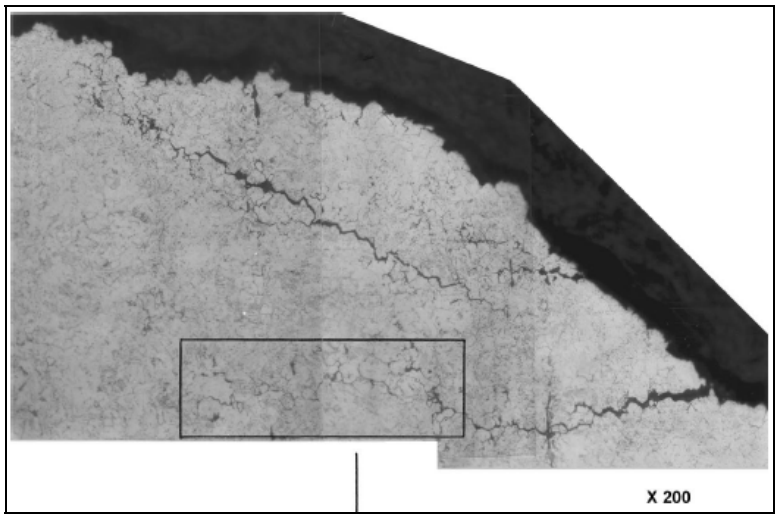

Figure 2.5: Photograph of Subsurface Intergranular Cracks

To aid in the evaluation of fracture surfaces associated with circular shafts or round bars the American Society of Metals publishes one of the most comprehensive schematics for interpreting fatigue fractures shown in Figure 2.6 [5]. The schematics offer a matrix of illustrations that depict the appearance of the fracture surface depending on the loading type (i.e. axial loading, unidirectional bending, reversed bending, rotating bending, and torsion), the relative magnitude of the applied stress, and relative magnitude of the stress concentration.

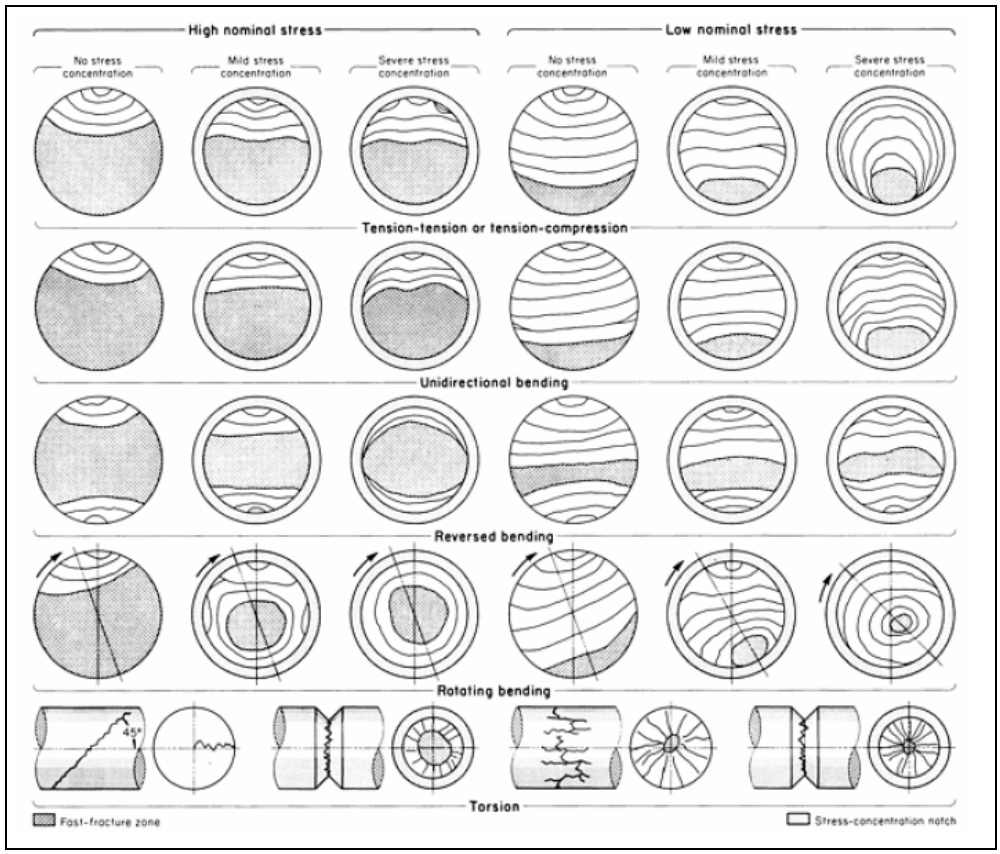

Figure 2.6: Illustrative Schematics of Typical Shaft Fracture Surfaces

2.2 Analytical Research

Some studies have been performed to compare the actual fatigue life of shafts with surface flaws to the predicted life based upon linear elastic fracture mechanics (LEFM) theory. Thompson and Sheppard [6] conducted a series of studies in which surface flaws at 90° and 45° on both smooth and notched shafts were subjected to both torsional and axial loading. Their studies mainly focused on life prediction models based upon the Mode I stress intensity factor (SIF). Their studies concluded that for relatively "large" cracks the actual life correlated well within a reasonable degree of accuracy with the life predictions based on Mode I SIF models where the Mode II and III SIFs were

much lower than Mode I. However, Thompson and Sheppard acknowledged a complication when the size of the crack became large in torsional loading cases. They asserted that when the crack size becomes large enough such that the Mode II SIF was no longer negligible that the life prediction models based on Mode I SIF would become invalidated.

Thompson and Sheppard also noted in their study that, while more testing is needed to develop a comprehensive quantitative understanding, a compressive stress acting parallel to the crack plane increases the crack propagation rate, while a tensile stress acting parallel to the crack plane decreases the crack propagation rate. Thompson and Sheppard supported their findings with work done by Smith and Pascoe [7] where they too found that tensile stresses parallel to the crack face reduced the fatigue crack propagation rate, while compressive stresses parallel to the crack face increased the fatigue crack propagation rate.

Both the work done by Thompson and Sheppard and by Smith and Pascoe are viewed as being intriguing given that the shaft crack pertaining to the typical intermittent pump shaft failure of Corken's larger pumps initiates in the vicinity of the seal drive pin hole, which is subject to compressive stresses due to the interference fit of the seal drive pin (see Figure 1.2).

Some additional research was conducted to better understand the effect of press fit geometry in the vicinity of a surface flaw or crack of a shaft subjected to rotary bending. Madia, Beretta, and Zerbst [9] researched the influence of local press fits in conjunction with rotary bending as it pertained to fatigue crack growth in railway axles. In their research they found that the load case of rotary bending as opposed to unidirectional or

reversed bending acted to increase the stress intensity factors of the crack front near the outer surfaces as compared crack front within the interior of the shaft. Figure 2.7 provides an illustration given by Madia, Beretta, and Zerbst where the SIF at point B located on the outer surface of the shaft would be larger in magnitude as compared with the SIF at point A. As a consequence of this they noted that this tended to flatten the crack as it propagates through the body of the shaft when the cracks initial shape is assumed to be elliptical. This phenomenon was also shown analytically by Carpinteri, Brighenti, and Spagnoli [10], however their research did not take into account any effects from nearby interference fits. The flattening of the crack shape as it propagates transversely through the interior of the shaft can also be seen in the fracture surface schematics shown in Figure 2.6, specifically for cases of low nominal stress where there is either no outer surface stress concentration or the existence of a "mild" stress concentration.

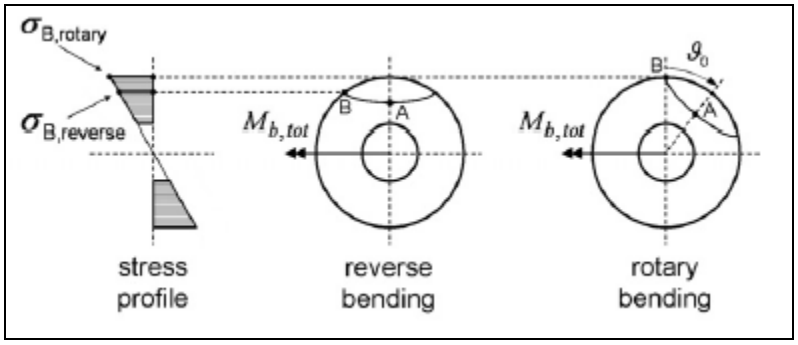

Figure 2.7: Illustration Denoting Point Locations Along Crack Front

In addition, Madia, Beretta, and Zerbst also found that the presence of a nearby interference fit served to negatively impact the life of the railway axles by increasing the fatigue crack propagation rate. In their study the nearby geometrical press fit served to

increase the longitudinal stresses in the railway axles, which acted perpendicular to the crack face. Madia et al. noted that the presence of the nearby interference fit did not increase the ΔK values, but instead increased the mean stresses thereby increasing the R ratio (Equation 2.1), which subsequently increased the fatigue crack growth rate.

$$R = \frac{K_{min}}{K_{max}} \tag{2.1}$$

From the standpoints of both mathematical modeling and post failure analysis there have been several studies conducted which served to better understand the mechanisms associated with shaft failures. The failure analysis studies have focused on root cause and outlining the sequence that lead to the ultimate failure of the pump or power transmission shaft. The analytical research conducted focused on an examination and mathematical modeling regarding the effects various loading and geometrical influence have on the stress state and fatigue life. However, no research concerning the stress state or failure analysis of a pump shaft of similar design and function to Corken's Z4500 pump model could be found. Perhaps failures of pump shafts involving mechanical seal assemblies and shrink fit rotors are not all that common throughout industry. However, for Corken pump shaft failures have been an ongoing engineering issue for decades and will continue if a complete understanding regarding the stress state during normal operation is not pursued.

2.3 Research Objectives

The purpose of this study is examine the stress state of the Corken Z4500 pump shaft under normal operating conditions through the use of both laboratory experimentation and numerical simulation using finite element analysis. Secondly, attempt to determine root cause of intermittent pump shaft failure based upon results stemming from the laboratory experimentations and numerical simulation studies. Experimental measurement of the strains of the pump shaft under normal operation will prove to be a complicated task, given that the strains must be measured while the pump is running thereby necessitating the use of telemetry equipment. In addition, the sealing integrity of the pump must be maintained to prevent large scale leakage.

While the design of the pump geometry (i.e. cam profile, relief valve design, etc.) as it relates to pump flow rate and discharge pressure is understood, the structural response of the power transmission components (i.e. pump shaft, rotor, blades, etc.) is not. Analytical research conducted thus far has examined the SIF and fatigue crack growth rates associated with steady state bending and torsional load cases. Experimental results of this study related to the structural response of the pump shaft are expected to be both highly dynamic and highly insightful into the true stress state of the pump shaft.

CHAPTER III

EXPERIMENTAL PROCEDURE

In order to fully examine the stress state of the Corken Z4500 pump shaft and to possibly determine root cause regarding the periodic fatigue failures several experimental tests were required to confirm the shaft material met current engineering specifications and to determine the real-time structural response of the pump shaft during operation.

3.1. Metallurgical Evaluation

The first test conducted was a metallurgical review to confirm the mechanical properties of the pump shaft and to determine the engineering stress-strain curve for the pump shaft material. The pump shaft material is AISI 8620 per ASTM A322 specified as having a fine grain condition, cold finishing, and a Brinell Hardness Number (BHN) of 207. The metallurgical tests were conducted by Douglas A. McClure, P.E. of McClure Engineering, Inc. [11], which is the primary supplier of metallurgical services for Corken. Table 1.1 lists the results of the tensile tests performed on the shaft specimens per ASTM E8-09. The test results obtained regarding the mechanical tensile properties were consistent with heat treated AISI 8620 to a BHN 207.

Initial Diameter (in)	0.497
Final Diameter (in)	0.368
Ultimate Tensile Strength (ksi)	95
Yield Strength (ksi)	83
Elongation (% in 2”)	19
Reduction of Area (%)	52

Table 1.1: Material Property Test Results of AISI 8620

A second tensile test was conducted to generate an engineering stress-strain curve for the sample shaft material. Figure 3.1 shows the resulting stress-strain curve that was generated. This engineering stress-strain data was subsequently converted into true stress-strain data and used to model plastic deformation using the finite element method associated with the interference fit of the seal assembly pin into the pump shaft. The results from these analytical studies will be covered in Chapter IV.

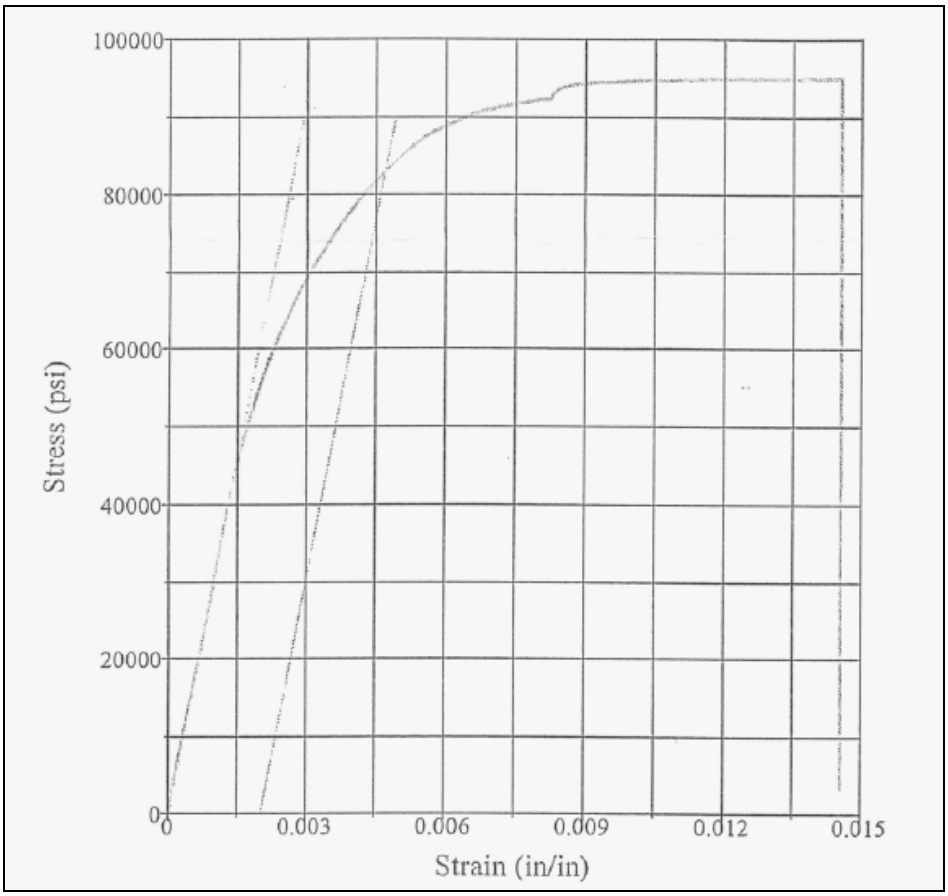

Figure 3.1: Engineering Stress-Strain Diagram of Sample Shaft Material

3.2 Seal Drive Pin Interference Fit Experimentation

To ensure that the pump mechanical seal rotates with the pump shaft a seal drive pin is press fit into pump shaft and held into position by means of interference fit. Figure 1.2 shows a cross section of the pump assembly where the seal drive pin is inserted into the pump shaft. To examine the effects of the interference fit had on the material that surrounds the seal drive pin hole in the pump shaft a test was devised to insert the seal pin in a manner similar to the current manufacturing methods and to extract the pin after insertion to examine the circumferential area of the seal drive pin hole that lies underneath the head of the assembled pin.

Figure 3.2 provides an illustration of the Z4500 pump shaft where modifications were made such that the seal drive pin, once assembled to the pump shaft, could be removed by tapping on the bottom side of the pin via a drilled hole located coaxially on the opposite side of the shaft. The drilled hole serving as a means of pin extraction was kept sufficiently small to not affect the results of the test, yet large enough to enable the insertion of a cylindrical tool to facilitate the extraction of the pin.

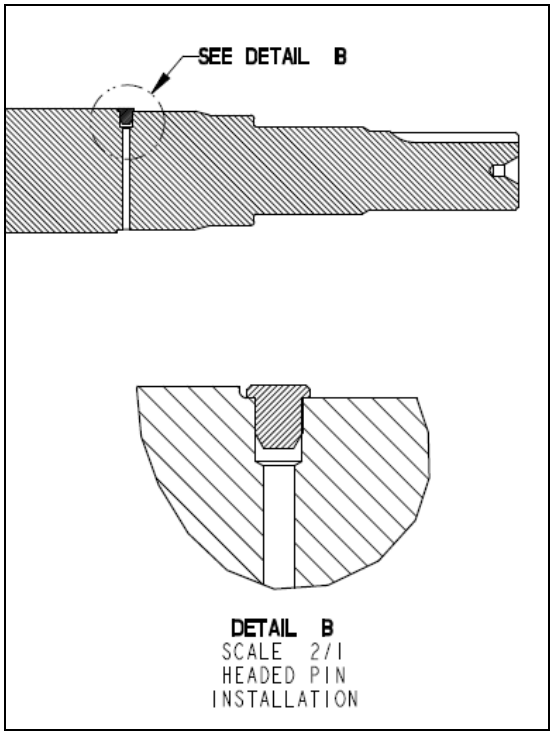

Figure 3.2: Modified Pump Shaft for Seal Drive Pin Extraction

Prior to pinning the shaft the surface of the shaft was cleaned of any foreign debris, machining chips, and rust inhibitor. Four separate locations were marked and labeled as shown in Figure 3.3 around the circumference of the seal drive pin hole to provide locations where photographs would be taken at an optical zoom of 200X.

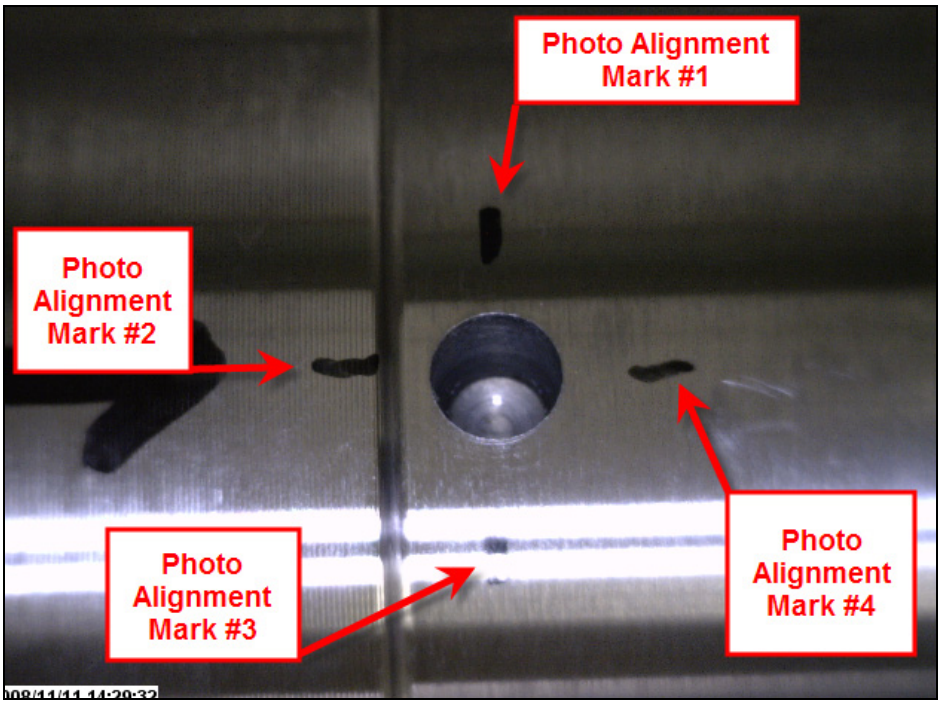

Figure 3.3: Photograph of Alignment Marks of Seal Drive Pin Hole

Figures 3.4 through 3.7 show a side-by-side comparison of the un-pinned hole versus the pinned hole for each of the alignment marks identified previously in Figure 3.3. Figures 3.8 and 3.9 show overall photographs of the seal drive pin hole before and after pinning, respectively.

It can be seen from the photographs that there is an appreciable amount of plastic deformation in the area surrounding the seal drive pin hole after pinning. However, it can be seen that the plastic deformation is more highly concentrated at alignment marks #1 and #3, which are located transverse of the shaft axis. No visible cracks near or around the seal drive pin hole were observed.

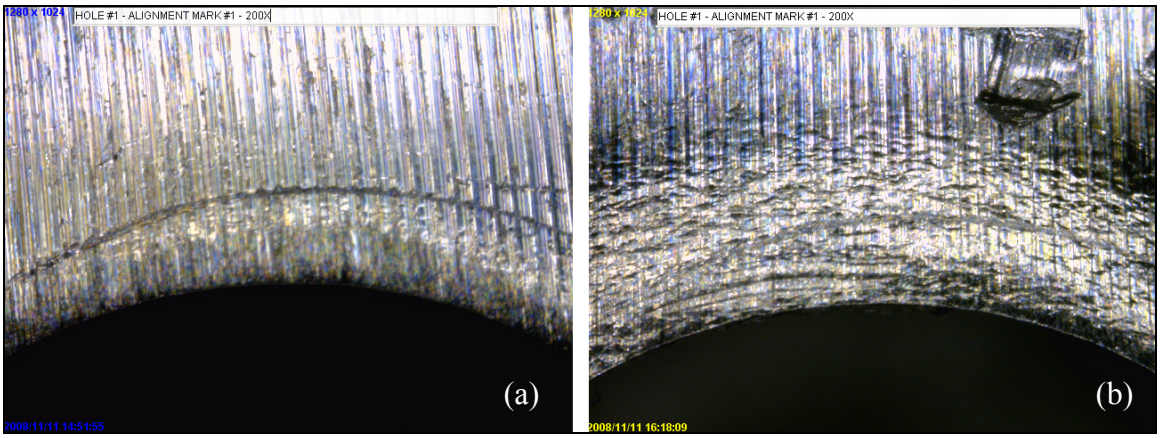

Figure 3.4: Photographs of Seal Drive Pin Hole at Alignment Mark #1 (a) Before Pinning, (b) After Pinning

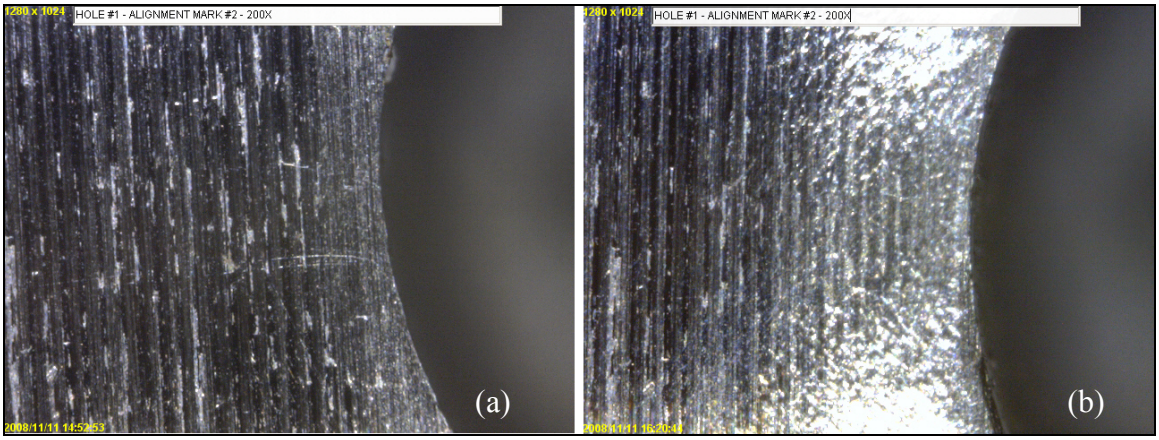

Figure 3.5: Photographs of Seal Drive Pin Hole at Alignment Mark #2 (a) Before Pinning, (b) After Pinning

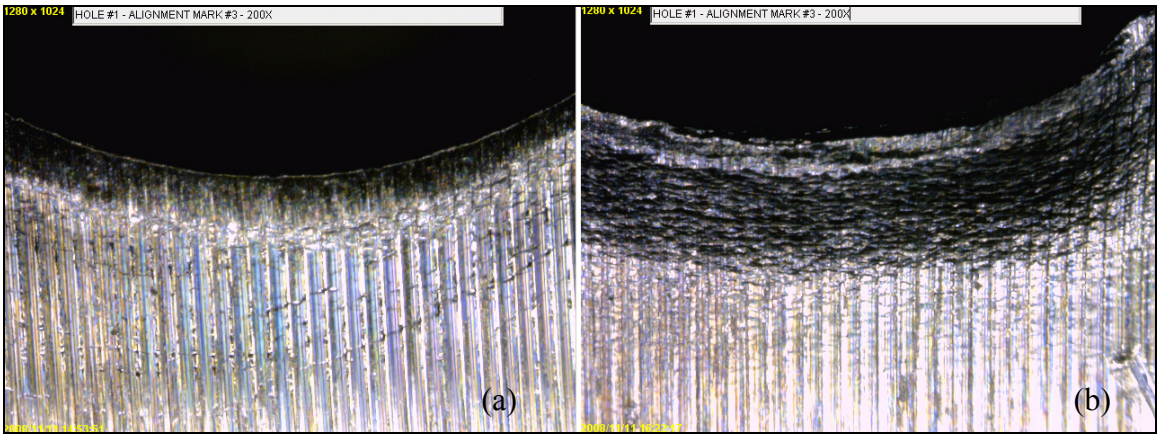

Figure 3.6: Photographs of Seal Drive Pin Hole at Alignment Mark #3 (a) Before Pinning, (b) After Pinning

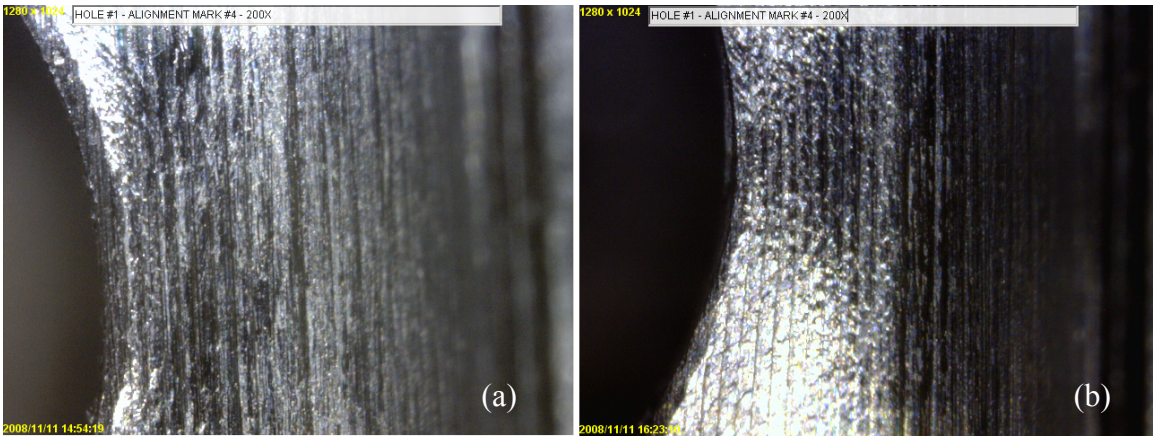

Figure 3.7: Photographs of Seal Drive Pin Hole at Alignment Mark #4 (a) Before Pinning, (b) After Pinning

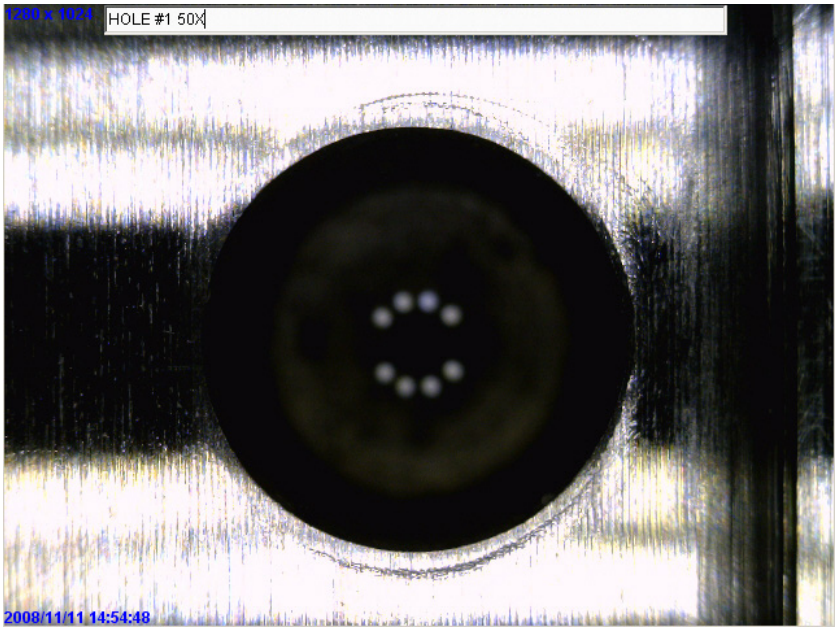

Figure 3.8: Overall Photograph of Hole Prior to Pinning

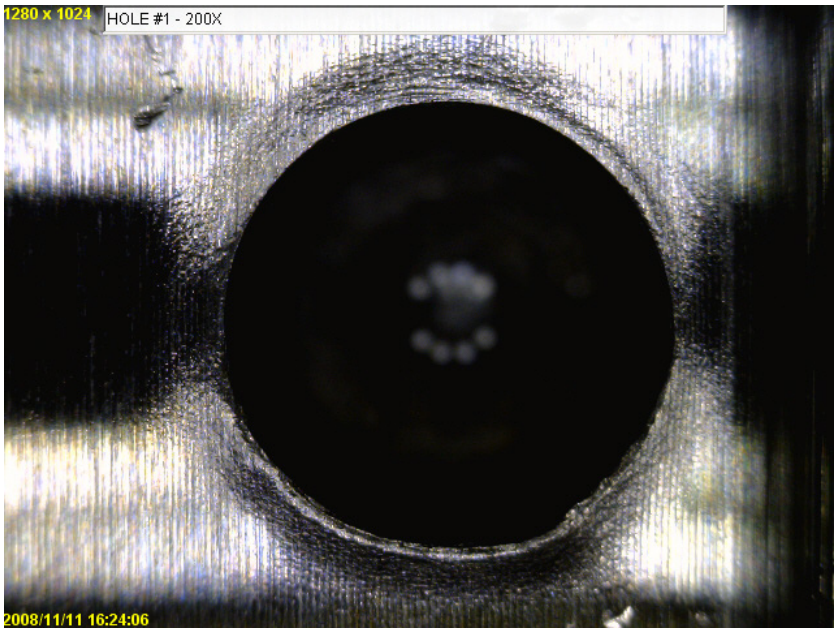

Figure 3.9: Overall Photograph of Hole After Pinning

In order to have a better view of the damage sustained to the pump shaft around the seal drive pin hole after the press fit operation a second shaft sample was modified according to Figure 3.2. The shaft was subsequently pinned and then the pin was extracted. This second shaft sample was then sent to Douglas McClure of McClure Engineering, Inc. so that scanning electron microscopic (SEM) photographs could be taken of the area surrounding the seal drive pin hole in the shaft.

Figures 3.10 and 3.11 show two different views of the seal drive pin hole in the shaft prior to the press fit operation. Machining marks on the outer surface of the shaft can be visibly seen as well as the circular machine marks inside the seal drive pin hole. A small amount of plastically deformed metal can be seen around the perimeter of the seal drive pin hole. This small ring of material is attributed to the drilling operation.

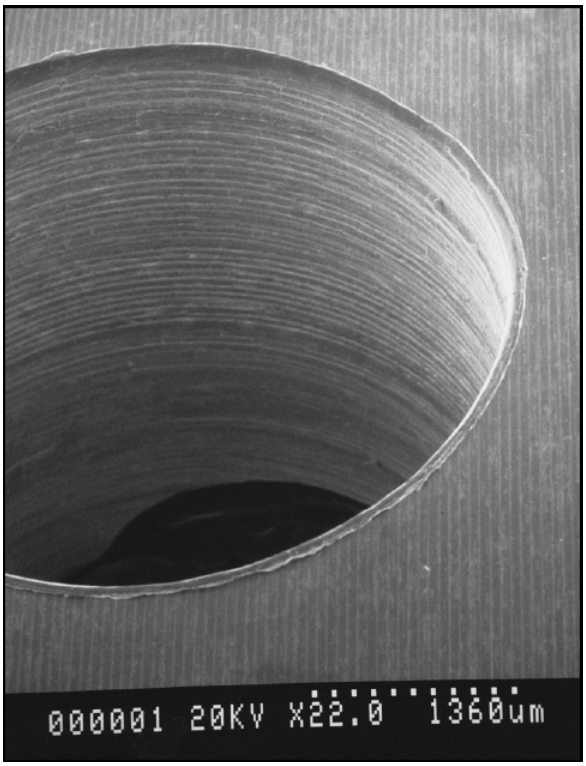

Figure 3.10: SEM Photograph of Seal Drive Pin Hole Prior to Pinning

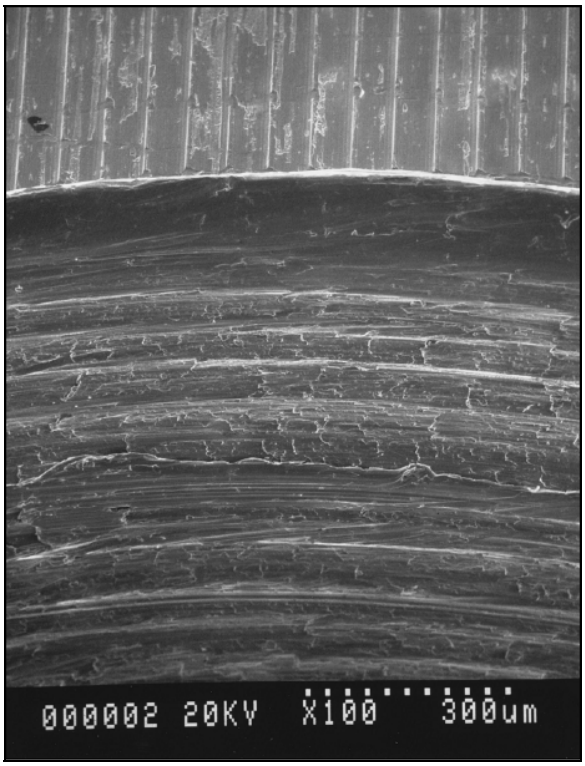

Figure 3.11: SEM Photograph - Closer Examination of Seal Drive Pin Hole

Figures 3.12 and 3.13 are SEM photographs of the seal drive pin after the press fit operation. Figure 3.12 indicates a small amount of circumferential damage in the upper right corner of the photograph. It is also noted on Figure 3.12 a small tear in the rim of the hole as well. Figure 3.13 provides a closer look at the seal drive pin hole after the press fit operation. No visible cracks can be seen. Figure 3.14 is a SEM photograph of the seal drive pin hole after pinning where a shaving from the seal drive pin was left behind. Also, it is noted in this photograph the lack of any plastic deformation around the diameter of the hole. A possible reason for this might be due to the reduced diameter of the seal drive pin, because some of the outer diameter of the pin was sheared away.

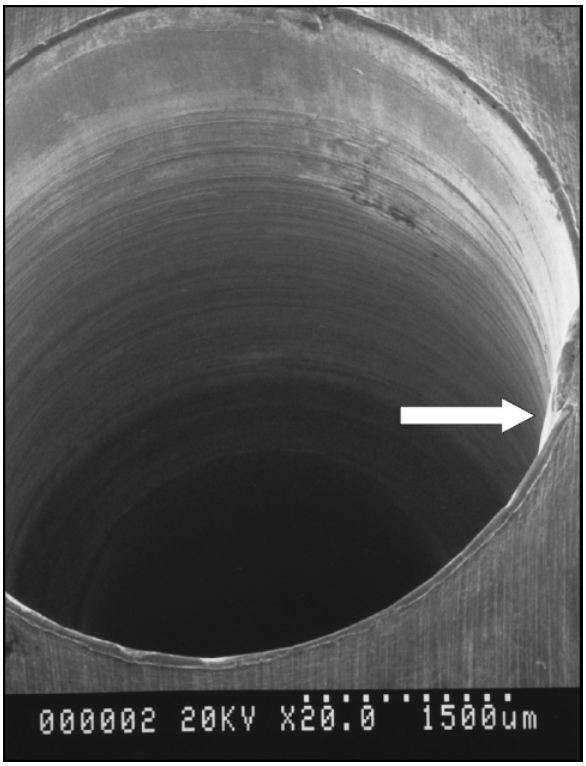

Figure 3.12: SEM Photograph of Seal Drive Pin Hole After Pinning

Figure 3.13: Closer Examination of Seal Drive Pin Hole After Pinning

Figure 3.14: SEM Photograph of Seal Drive Pin Hole After the Pinning Operation Showing a Shaving From the Pin

3.3 Pump Discharge Pressure Experimentation

Because the structural response of the pump shaft is directly related to the differential pressure of the pump, an experiment was conducted to closely examine the pump discharge pressure during normal operation. The goal here was to determine if there are any abnormal pressure spikes present in the discharge of the pump, which could contribute additional stresses on pump shaft, and to characterize the pressure loading that the pump shaft would experience.

Since the tank from which the pump would be circulating was open to atmosphere and the liquid level above the pump was limited, the inlet pressure to the pump was assumed to be approximately atmospheric or 0 psi gauge pressure. The pump discharge pressure was measured in two separate locations: the pump discharge pressure port designed into the pump case and a pressure tap drilled into the case to capture the pump chamber pressure as closely as possible. Figure 3.15 shows a photograph where the pressure and positional measurements were taken. In order to gain access to the pumping chamber an additional pressure port was drilled and tapped into the side of the pump opposite the inlet. In addition, an inductive proximity sensor was used to capture the location of the pump shaft as it rotates. The data from the inductive proximity sensor would be used to provide a means to relate any possible pressure spikes to the position of the rotor and blades. Figure 3.16 shows a photograph labeling the various internal components of the pump and identifying the pumping chamber.

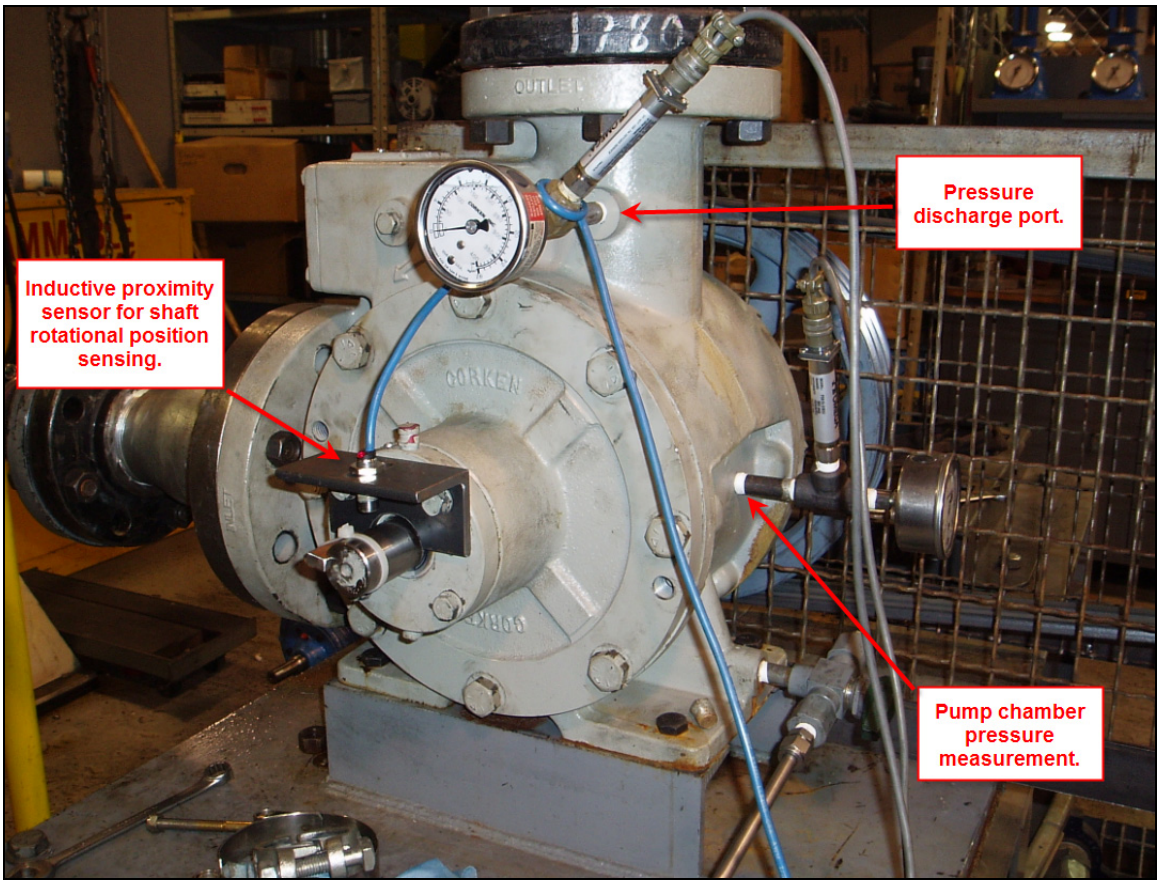

Figure 3.15: Pump Pressure and Shaft Positional Measurements

Pressure measurements were acquired using two 4-20ma, 0-300 psig pressure transducers from Omega. The inductive proximity sensor was a 12mm barrel type sensor that positioned on the bearing cap of the pump via a bracket where the shaft position was picked up using a modified shaft key. Signal data from the pressure transducers and inductive proximity sensor was acquired using National Instruments data acquisition hardware with a SCXI signal conditioning chassis at a sample rate of 1000 Hz. A sample set of 30,000 samples was collected and streamed to an ASCII text file. Examples of the data acquisition program written in LabView for this experiment are shown in Appendix A.

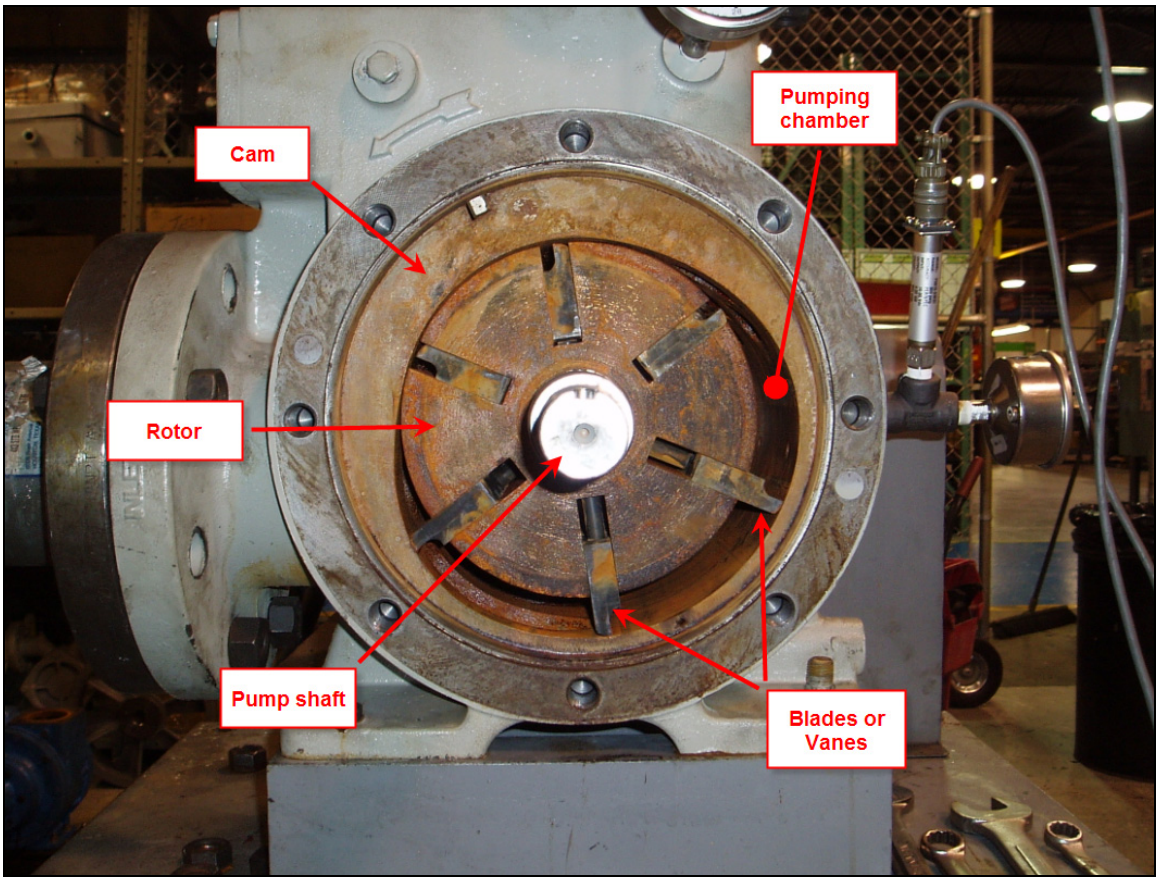

Figure 3.16: Internal Pump Components and Pumping Chamber

An excerpt of the data collected is shown in Figure 3.17. There was an obvious difference in mean value between the pump discharge pressure and the pump chamber pressure. In addition, the acquired data revealed pressure oscillations within the pumping chamber. The pump chamber pressure oscillations were noted as having six (6) peaks per revolution, which is identical to the number of vanes within the pump. A complete revolution of the pump is shown in the data presented in Figure 3.17 as the time between peaks of the inductive sensor voltage. The inductive sensor voltage signal was such that when the modified shaft key was present directly underneath the inductive sensor the inductive sensor output voltage would immediately drop.

The mean difference between the pump discharge pressure and the pump chamber pressure in conjunction with the pressure fluctuations observed within the pumping chamber appear to be related to the number of vanes in the pump and may indicate the possibility of liquid compression within the pump. Liquid compression within positive displacement pumps is viewed as being detrimental due to the magnitude of the resulting pressures, the loss in efficiency, and the subsequent torque variations which result in vibration. However, the mean difference between the pump discharge and the pump chamber pressure may simply be a function of the pressure losses as the fluid travels from the pumping chamber, through the cam outlet porting, and into the main volume of the discharge cavity.

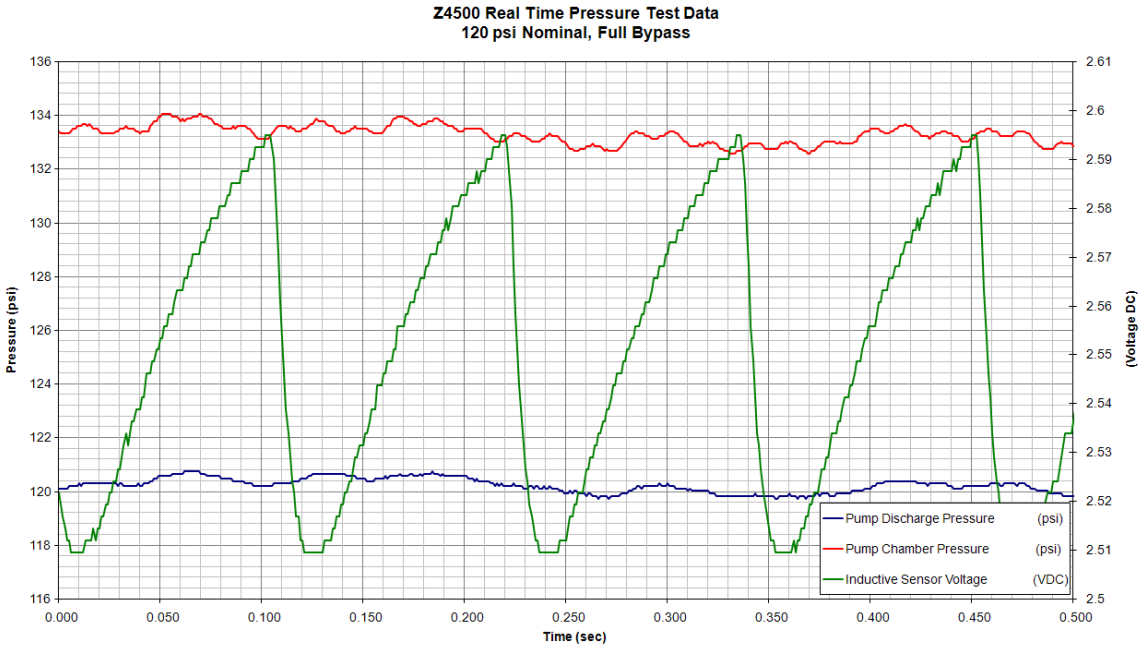

Figure 3.17: Pump Pressure Test Results

3.4 Pump Shaft Structural Response Instrumentation Validation

3.4.1 Gauge Selection, Location, Data Acquisition, and Protection

The next step in examining the stress state of the pump shaft is to directly measure the structural response of the pump shaft during normal operation. To accomplish this mechanical strains were measured directly using a strain gauge rosette located on the pump shaft in an area where mechanical failures were typical. The strain gauge used was a 0°-45°-90° stacked rosette with a self temperature compensation matched to steel, a gauge resistance of 350 Ohms, gauge length of 3 mm, and prewired in a three wire arrangement to negate the thermal effects of the lead wire resistance. Figure 3.18 provides an illustrative example of the strain gauge rosette that was used for the experimentation. Figure 3.19 is a photograph of the stacked rosette labeling the individual gauge numbers.

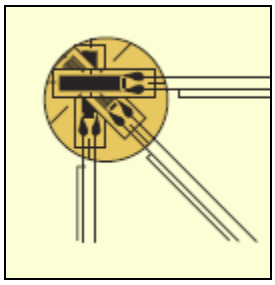

Figure 3.18: Illustration of Stacked Strain Gauge Rosette

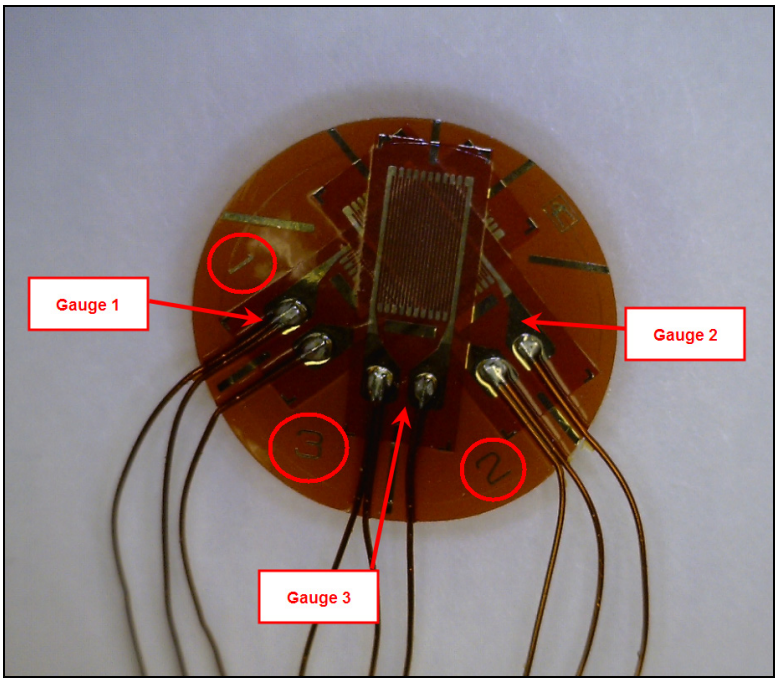

Figure 3.19: Photograph of Stacked Rosette Layout

One of the primary motivations in selecting a strain gauge rosette as the gauge type is due to the insensitivity to angular misalignment with respect to the derived principal strain based upon the three independent gauge measurements. The relationship between the derived principal strain and the individual gauges are shown analytically via Equation 3.1 [12] in combination with the gauge layout shown in Figure 3.20. Table 3.1 provides the relationship between the gauge numbers on the stacked rosette and the gauge letters used in Equation 3.1.

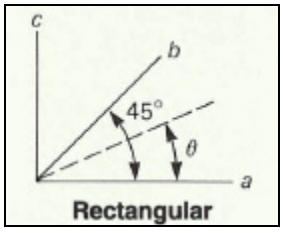

Figure 3.20: Rosette Gauge Labels for Equation 3.1

$$\varepsilon_{1,2} = \frac{1}{2}\left[\varepsilon_a + \varepsilon_c \pm \sqrt{2(\varepsilon_a - \varepsilon_b)^2 + 2(\varepsilon_b - \varepsilon_c)^2} \right] \tag{3.1}$$

Stacked Rosette Gauge Number	Equation 3.1 Strain Letter
1	a
2	c
3	b

Table 3.1: Gauge Numbering to Lettering Conversion

Determining the strain gauge location was critical. The gauge had to be placed near the seal drive pin hole where the typical Z4500 pump shaft failures were occurring, however this region was typically reserved for the mechanical seal assembly as shown in Figure 1.2. Due to lead wire routing and the protective coating that was applied to the shaft, it was decided to operate the pump without a mechanical seal on the drive side of the pump. Removal of the mechanical seal on the drive side was viewed as having no adverse affect on the mechanical response of the pump shaft. Leakage of the pump product through the bearing assembly was minimized by reversing the grease lip seal shown in Figure 3.21 such that a positive seal was made when pressurized from within the pump. Figure 3.22 is a photograph of the gauge installed on to the pump shaft near the seal drive pin. Bonding of the gauge to the shaft was performed using Loctite 496, which is a cyanoacrylate adhesive recommended for strain gauging.

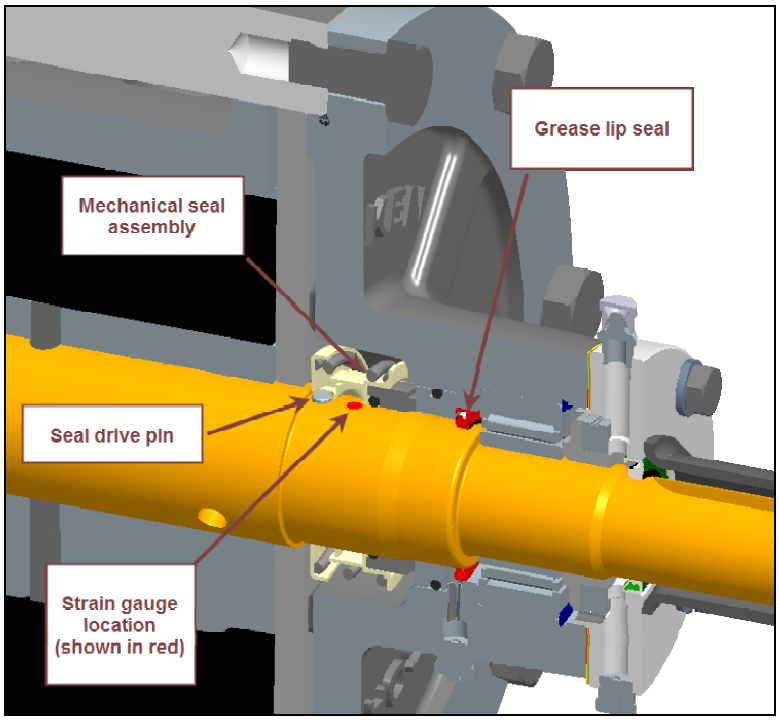

Figure 3.21: Strain Gauge Location

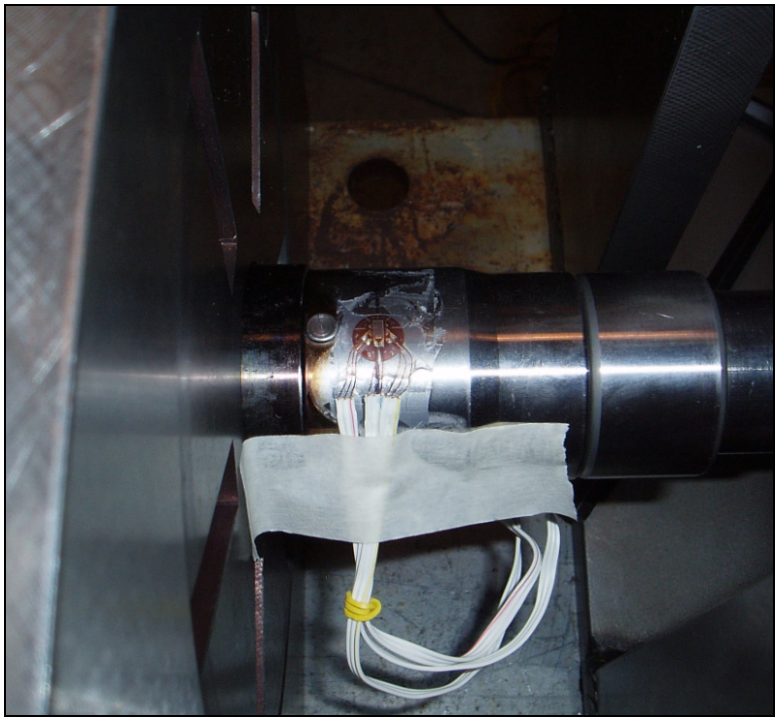

Figure 3.22: Photograph of Strain Gauge Rosette

Because strain gauge measurements were required while the pump shaft was rotating this necessitated the use of telemetry / data logging data acquisition hardware. The telemetry hardware selected was a V-Link 2400-M wireless voltage node manufactured by MicroStrain, Inc. This module contained four differential input channels with a bridge excitation voltage of 3 VDC for strain gauge measurement and three singled ended input channels for basic transducer voltage measurement. It was capable of sample rates of up to 2048 Hz and onboard memory capacity of 2 MB. However hardware issues that will be covered later in this chapter forced the use of lower sample rates than the published maximum. For this experiment three of the four differential input channels would be utilized to measure each of the individual gauges on the strain gauge rosette. The three differential channels utilized would be configured as a quarter bridge circuit with 350 Ohm bridge completion resistors and 499 kΩ shunt calibration resistor.

The telemetry hardware had to be located such that it would rotate with the shaft during the operation of the pump. The telemetry module was too large to be positioned inside the pump, therefore it was located on the end of the pump shaft between the driving motor and the pump within a custom designed shaft coupling shown in Figure 3.23. The routing for the strain gauge lead wires could not be located on the outside surfaces of the pump shaft due to the radial roller bearings and elastomeric shaft seals. Therefore, a hole was drilled through the center of the pump shaft to a depth where the end of the drilled hole was positioned at approximately the location of the strain gauge. Subsequently, a hole was drilled radially from the outside diameter of the pump shaft opposite the seal drive pin hole towards the center of the pump shaft. Figure 3.24 shows

the drilled holes shaded in light blue that were used to route the strain gauge lead wires from the gauge to the telemetry hardware.

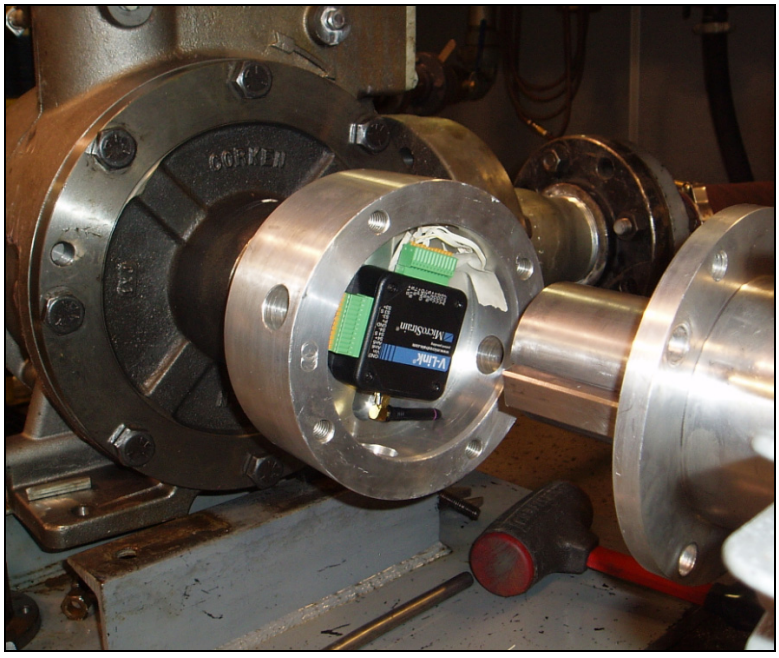

Figure 3.23: Photograph of Installed Telemetry System

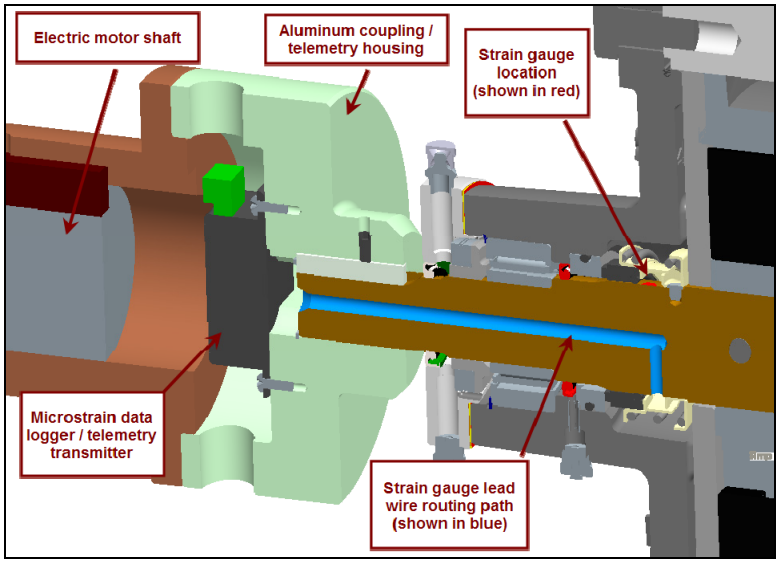

Figure 3.24: Strain Gauge Lead Wire Routing

One final issue regarding the strain gauging was protection of the gauge and fine lead wires while submerged in pressurized fluid. The test fluid used by Corken, Inc. is clear Electrical Discharge Machining (EDM) oil. The first attempt at protecting both the gauge and the lead wires that were routed around the outer circumference of the pump shaft was to use commercially available clear silicone. However, during one of the experiments it was discovered that EDM fluid dissolves silicone. Therefore, a second attempt to protect both gauge and its lead wires was performed using several coats of commercially available cyanoacrylate adhesive. This protection method proved to be successful at both protecting the gauge from the EDM fluid and protecting the lead wires from incidental displacement. Figure 3.25 is a photograph of the rotor/shaft assembly with the protective coating over both the gauge and the lead wires routed circumferentially to the radially drilled hole.

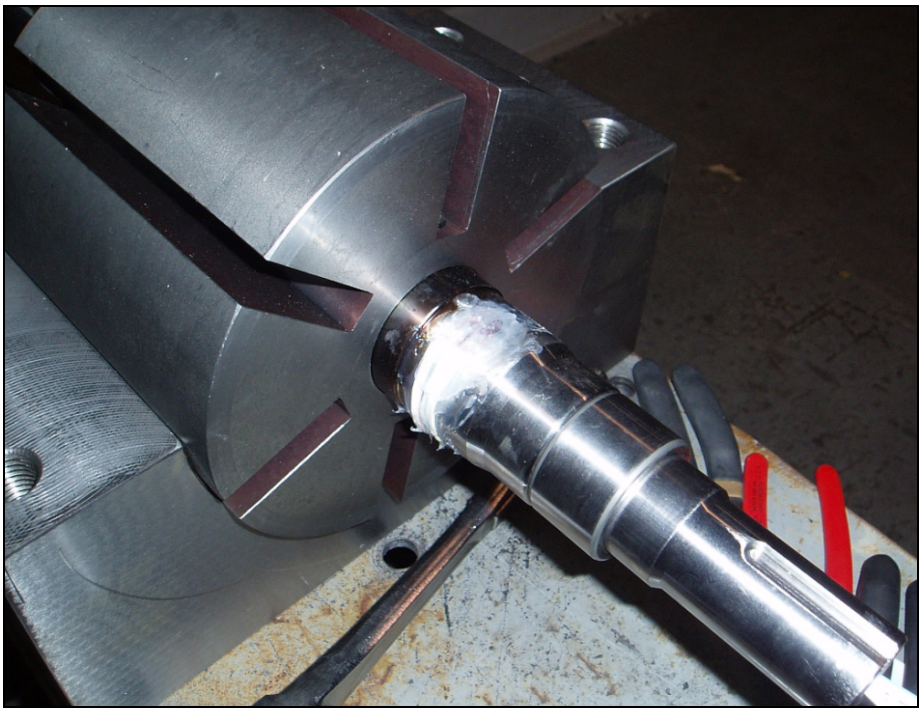

Figure 3.25: Photograph of Strain Gauge with Protective Coating

3.4.2 Validation of Gauge Bonding and Telemetry Hardware

3.4.2.1 Validation Static Test Fixture Design

In order to validate both the effectiveness of the bond between the gauge and the shaft surface and to validate the measurements obtained by the telemetry equipment prior to installation and experimentation, a static test fixture was designed and built to apply a fixed 1000 lbf vertical load to the end of the pump shaft in order to produce a known strain. This known applied strain would then be compared to the principal strain results stemming from a finite element analysis of the rotor/shaft assembly to ensure that measured applied strain was not only accurate, but that it also was being measured accurately by the telemetry hardware. Later in this chapter it will be discussed how this validation step identified a previously unknown issue with the telemetry hardware, which resulted in the manufacturer making a design revision not only on the hardware used in this experimentation, but also at a production level.

Figures 3.26 through 3.29 are photographs of the static test fixture with the rotor/shaft assembly installed. The static test fixture was comprised of two main parts: the clamp assembly and the loading frame; both of which were mounted to a large structural steel frame. The clamp assembly is comprised of two large machined blocks with an inner radius cut to match the radius of the pump shaft rotor. A slight gap was intentionally designed into the clamp assembly to provide means to apply clamping force to the entire cylindrical rotor surface to simulate a fixed boundary constraint within the finite element model. The fasteners used to apply the clamping load to the top and bottom halves of the clamping assembly were tightened to a torque value of 150 lbf-in.

A fastener pre-load force based upon the applied fastener torque values was included in the finite element model.

The loading frame, best shown in Figures 3.27 and 3.29, contained a one inch diameter fine thread lead screw for applying axial force by means of applied torque. The lead screw was connected in series with a 1000 lbf load cell and a custom designed clamp located at the end if the shaft. The load cell transmitted the applied axial force by means of a load cell button. The shaft clamp was a block of steel machined exactly 1.000 inches in width, which clamped onto the end of the shaft in order to simulate a distributed load over a one inch long region of the pump shaft. This shaft clamp was specifically design to facilitate the modeling of a bending load by avoiding the need to model a point load within the finite element model. The creation of a point load would have created a numerical singularity.

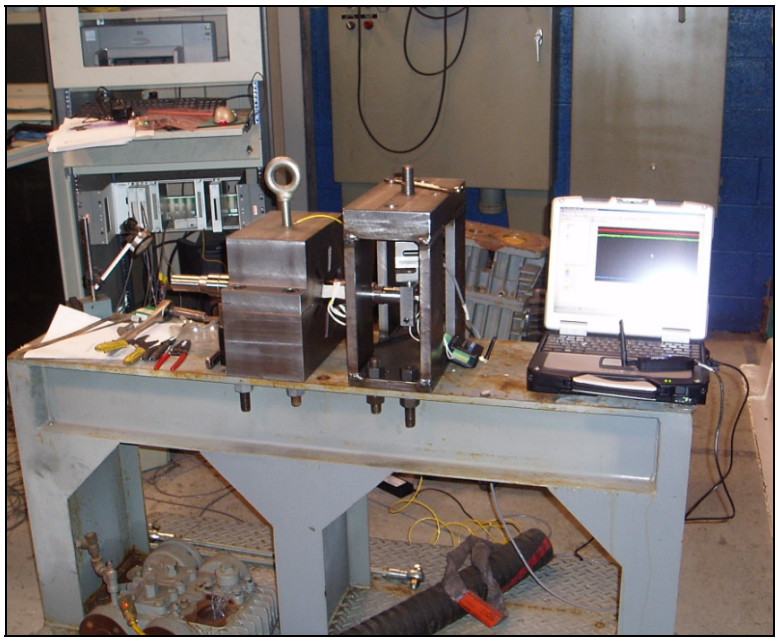

Figure 3.26: Overall Photograph of Static Test Fixture

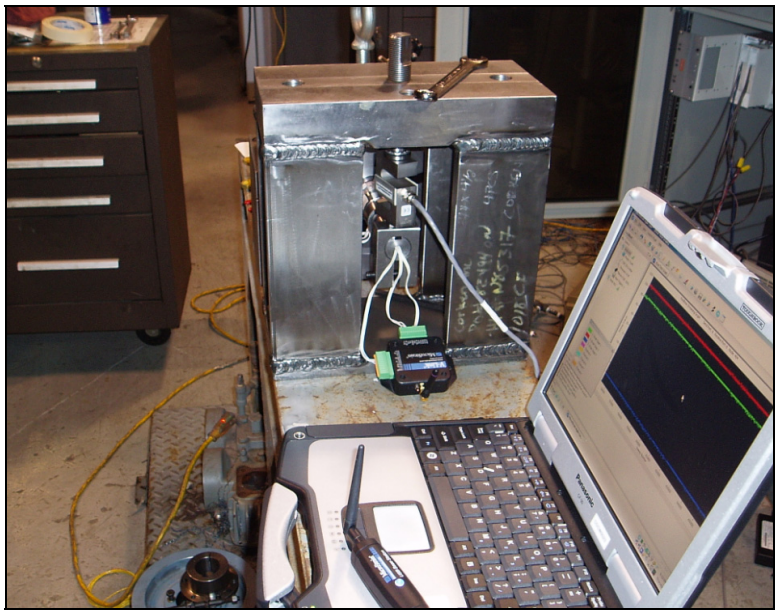

Figure 3.27: Photograph of Telemetry End of Static Test Fixture

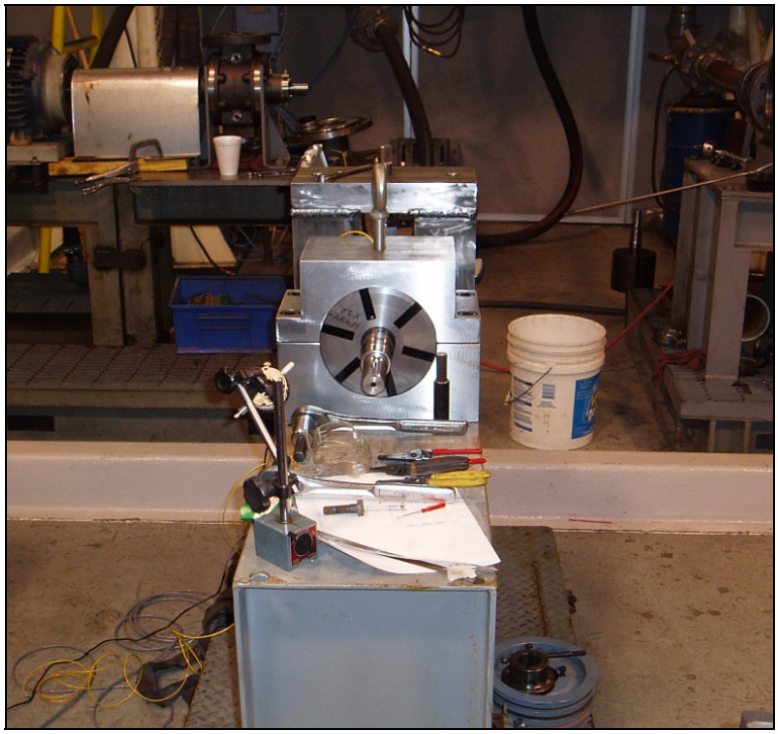

Figure 3.28: Photograph of Clamp End of Static Test Fixture

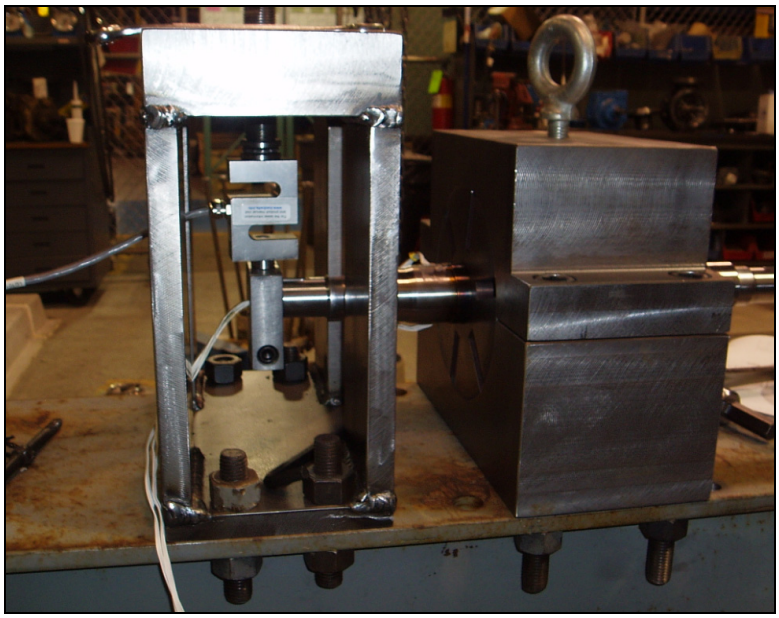

Figure 3.29: Photograph of Load Cell and Shaft Clamp

3.4.2.2 Static Test Fixture: Instrumentation and Data Acquisition

As mentioned previously a load cell was used during the experimentation utilizing the static test fixture. The load cell supplied by Omega had a capacity of 1000 lbf in either tension or compression, required 10 VDC excitation, and supplied a signal of ±30 mV at the maximum rated capacity. A calibration data sheet was provided with the load cell and was used in formulating the load versus signal curve within the data acquisition software.

National Instruments data acquisition hardware was used to acquire the load cell signal for all of the static test fixture validation experiments and was used to validate the bond between the strain gauge and the pump shaft prior to utilizing the telemetry hardware from MicroStrain. All signal wires from both the load cell and strain gauge rosette were connected to signal conditioning modules within the National Instrument SCXI chassis signal multiplexer. The voltage signal coming from the load cell was

connected to a SCXI-1102 input module via a SCXI-1303 connection block. The strain gauge rosette lead wires were connected to the SCXI-1520 universal strain gauge input module via the SCXI-1314 terminal block, which acquired the signal from the strain gauges and provided the bridge excitation for each of the rosette gauges as well. The bridge excitation was selected programmatically as 3 VDC in order to match the bridge excitation values of the MicroStrain telemetry hardware. Shunt calibration was accomplished via 499 kΩ internal shunt resistors within the SCXI-1520, while null offsetting was accomplished programmatically via software. Figure 3.30 is a photograph of the static test fixture data acquisition system.

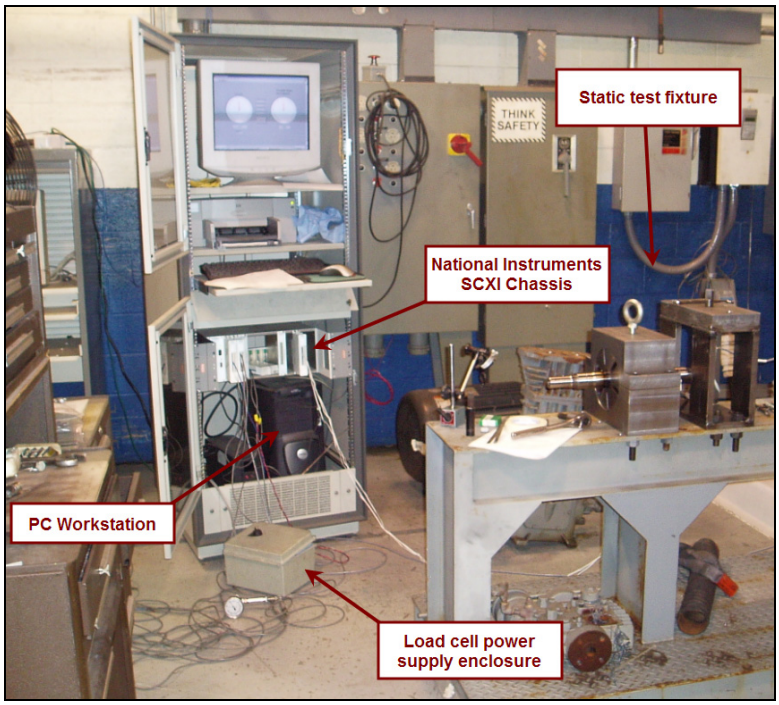

Figure 3.30: Photograph of Static Test Fixture DAQ System

The software program written for the acquisition of the load cell and strain gauge measurements was created in National Instruments LabView. A copy of the program can be found in Appendix B.

As previously mentioned in Section 3.4.1 the telemetry equipment selected for the experimentation was the V-Link 2400-M strain gauge module. During some preliminary experimentation used to test the functionality of the telemetry hardware, a severe amount of negative signal drift was observed, specifically at sample rates above 2 Hz. Figure 3.31 shows a graph of some sample data that was collected when the negative drift occurred. The actual settling time was unknown, but was found to last greater than 60 seconds.

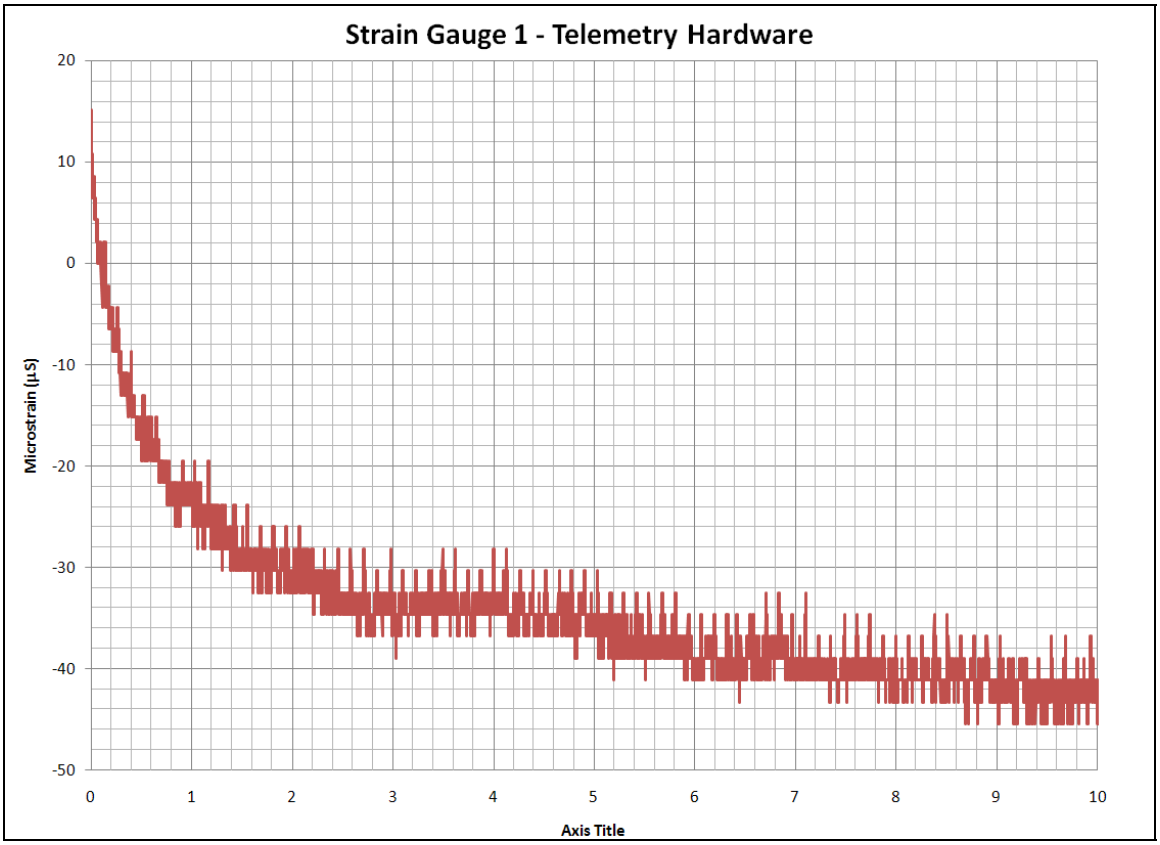

Figure 3.31: Acquired Telemetry Data Showing Negative Signal Drift

The manufacturer was contacted and subsequent investigation revealed an issue with the internal bridge completion resistors, specifically related to their temperature sensitivity. A permanent solution was determined by the manufacturer, however would have been implemented well beyond the calendar timeline allotted for this

experimentation. Therefore, a temporary fix was implemented involving a set of bridge completion resistors with improved temperature sensitivity characteristics. The modified telemetry system hardware still experienced some negative signal drift; however the negative drift was limited to a value of -5 to -12 μS with a settling time of 20 seconds. Experimental procedures were updated accordingly to average the negative offset between the elapsed time of 20 through 25 seconds and to subsequently manually adjust the acquired data upon completion of the individual experiments.

3.4.2.3 Validation Finite Element Model

In order to ensure that no errors had been introduced during the bonding procedure and that the MicroStrain telemetry hardware is accurately reading the strain gauge a finite element model with constraints, loads, and materials modeled to represent the static test fixture was created. In addition, the results from the numerical simulation model were also used to validate the measurements obtained via the MicroStrain telemetry system.

The geometry for the pump rotor/shaft assembly was provided by Corken, Inc. The remainder of the three dimensional geometry used in the finite element analysis was modeled in the Pro/Engineer solid modeling package. Since only the strains from the applied bending load were to be modeled, only the rotor and the shaft geometry were included; the pin geometry was excluded from this analysis. Figure 3.32 shows an illustration of the geometry used during the numerical simulation. A small 3 mm diametrical surface region was created on the pump shaft geometry in the identical location of the strain gauge rosette during experimentation, which would facilitate

directional and principal strain results extraction during the post processing phase of the numerical simulation. Figure 3.33 shows the strain gauge surface region that was created.

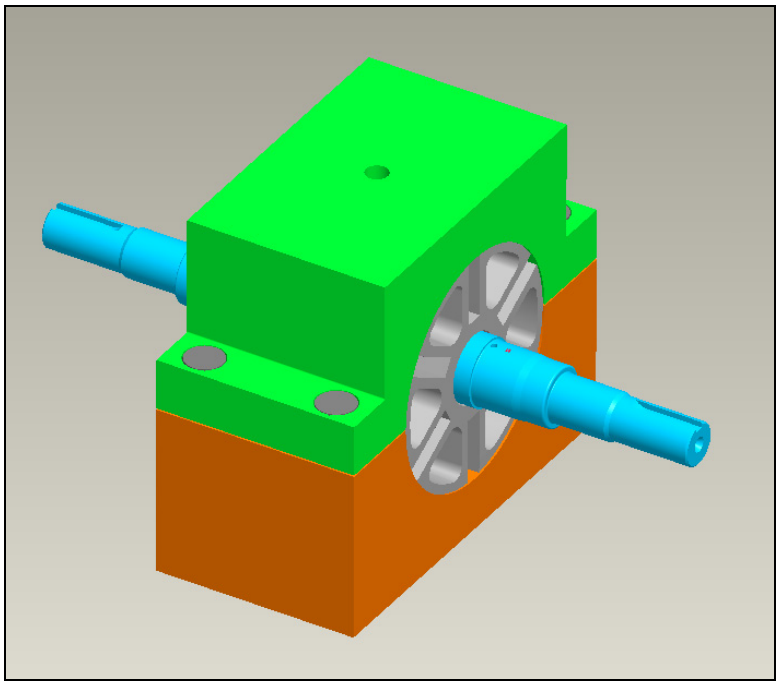

Figure 3.32: Finite Element Model Geometry

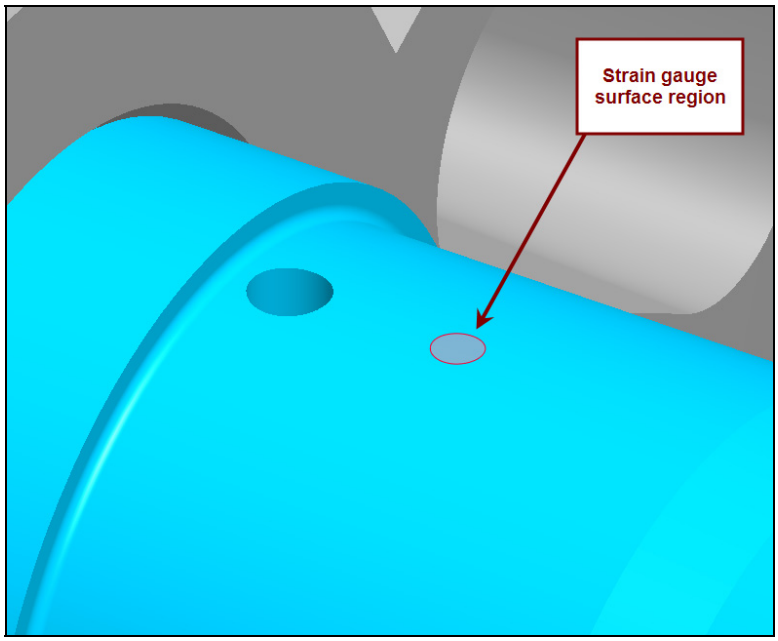

Figure 3.33: 3 mm Surface Region Representing the Actual Strain Gauge

Once some minor geometry simplification had been completed, the three dimensional geometry was imported into the commercial general finite element code Ansys and subsequently meshed. The finite element mesh shown in Figure 3.34 was comprised of 10-node tetrahedral elements and various sets of contact elements between the fasteners and the clamp, the clamps and the rotor, and the rotor and the pump shaft. The contact between the rotor and pump shaft was modeled as bonded contact so as to not include any additional strains from the shrink fit operation of the rotor onto the pump shaft. Table 3.2 lists the elastic material properties used for each of the components within the finite element model.

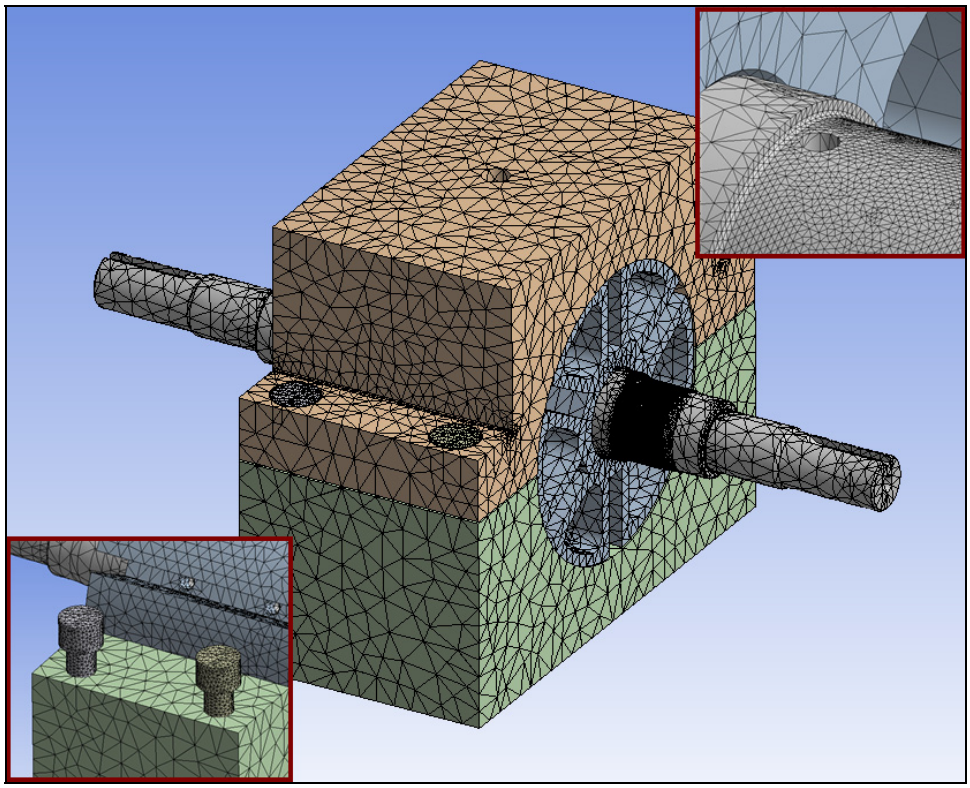

Figure 3.34: Finite Element Mesh of Static Fixture Model

Component Name	Material Description	Modulus of Elasticity (lbf/in^2)	Poisson's Ratio
Shaft	8620 Steel	2.97e7	0.29
Clamp (top)	Steel	2.90e7	0.30
Clamp (bottom)	Steel	2.90e7	0.30
Fasteners	Steel	2.90e7	0.30
Rotor	Ductile Iron 65-45-12	2.44e7	0.29

Table 3.2: Material Properties for Static Test Fixture Model Components

Next, the boundary conditions for the finite element model were applied. A downward vertical load of 1000 lbf in the negative global Y direction was applied over a one inch long region of the shaft starting from the end as shown in Figure 3.35. Fastener axial preload forces of 12,330 lbf were applied to each of the fasteners based upon equation 3.2 [13] with the equation parameter values shown in Table 3.3. All applied loads are shown as red surfaces in Figure 3.35. A fixed displacement constraint where elemental nodes are constrained in all three coordinate directions was applied along the bottom surface of the lower clamp. The lower left corner of Figure 3.35 shows the shaded blue surface where the fix displacement constraint was applied.

$$F_{PL} = \frac{T}{\left[(0.159)P + (1.156)\mu d\right]} \tag{3.2}$$

Applied Torque (T)	150 lbf-ft
Fastener Pitch (P)	1/10
Frictional Coefficient (μ)	0.15
Fastener Nominal Diameter (d)	0.75 in

Table 3.3: Fastener Parameter Values for Equation 3.2

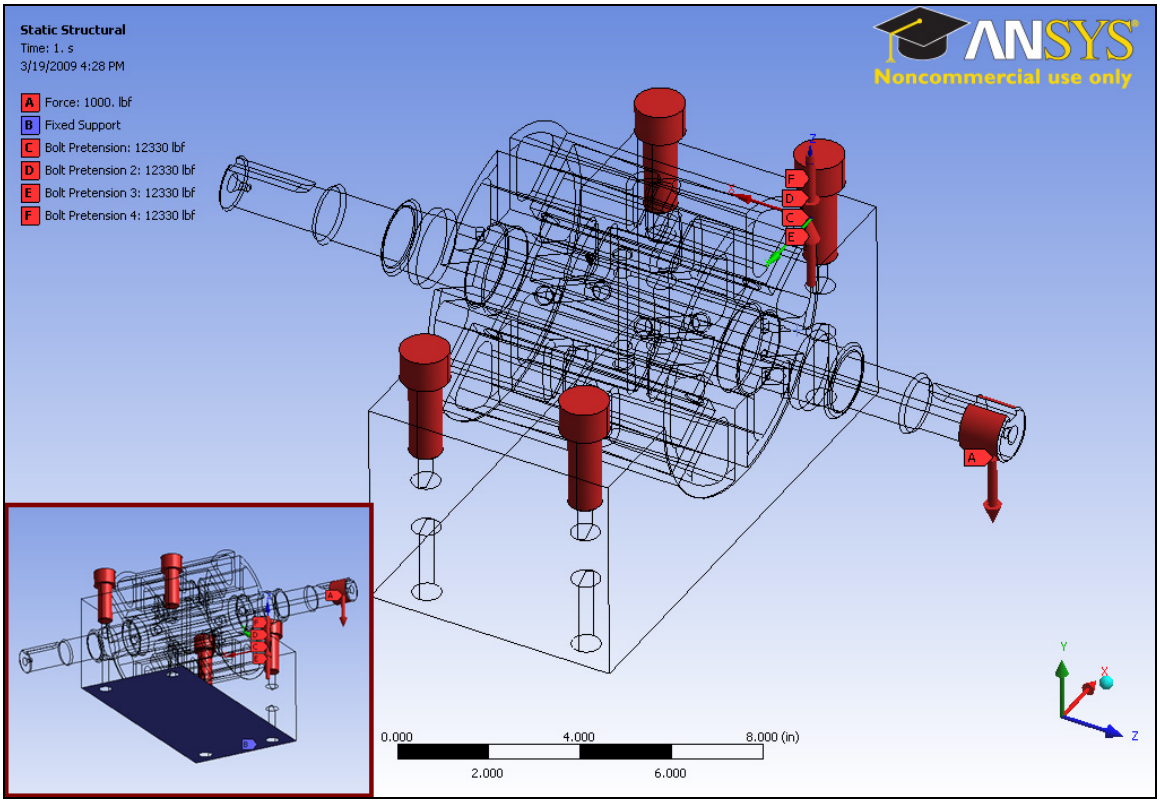

Figure 3.35: Finite Element Model Loads and Constraints

3.4.2.4 Validation Results

Based upon the static 1000 lbf load applied to the end of the shaft, Table 3.4 shows the averaged strain reading obtained using the National Instruments hardware for each of the individual grids within the rosette and the derived 1st principal strain value using Equation 3.1. Table 3.5 shows the averaged strain reading obtained using the MicroStrain telemetry hardware for each of the individual grids within the rosette and the derived 1st principal strain value using Equation 3.1 based on a static 1000 lbf load. Table 3.6 shows a comparison between the 1st principal strain values in Table 3.4, Table 3.5, and the numerical simulation results.

Measure Name	Averaged Strain (μS)
Rosette Gauge 1	87
Rosette Gauge 2	-68
Rosette Gauge 3	107
Max Principal Strain	262

Table 3.4: Averaged Measured Strain Values Using NI Hardware

Measure Name	Averaged Strain (μS)
Rosette Gauge 1	88
Rosette Gauge 2	-74
Rosette Gauge 3	105
Max Principal Strain	269

Table 3.5: Averaged Measured Strain Values Using Telemetry Hardware

	Derived Max Principal Strain – NI DAQ Hardware	Derived Max Principal Strain – MicroStrain Telemetry Hardware	Finite Element Model Averaged Max Principal Strain
Measured Value	262	269	278
Percent Difference Relative to Finite Element Model Results (%)	-5.8%	-3.2%	0.0%

Table 3.6: Principal Strain – NI Hardware vs. Telemetry vs. FEA

The correlation between the strain measured using the National Instruments hardware, the MicroStrain telemetry hardware, and the averaged 1st principal strain numerical simulation results appears to be very good. Therefore, it is accepted that the strain gauge rosette has been properly bonded to the shaft surface and that the telemetry equipment is properly measuring the gauge strains.

3.5 Pump Shaft Structural Response Experimentation

Once the strain gauge rosette bond to the pump shaft and the telemetry hardware had been validated, experimentation to determine the structural response of the pump shaft to normal operating loads could commence. The experimentation was initially conducted using a direct coupling between the motor and the pump where the coupling served as housing for the telemetry hardware as shown in Figure 3.36. However, the results contained repeatable and periodic spikes in principal strain. These spikes were initially interpreted as being the product of rotational binding due small amounts of

misalignment between pump and the motor where there was no compliant member present. Therefore, a double universal joint shaft assembly was inserted between the pump and the motor to eliminate any misalignment issues as shown in Figure 3.37. A series of experiments were conducted at three separate rotational speeds and three separate pump discharge pressures. The results from both experiment setups are presented later in this chapter and are used in the next chapter as a basis for comparison against numerical simulations.

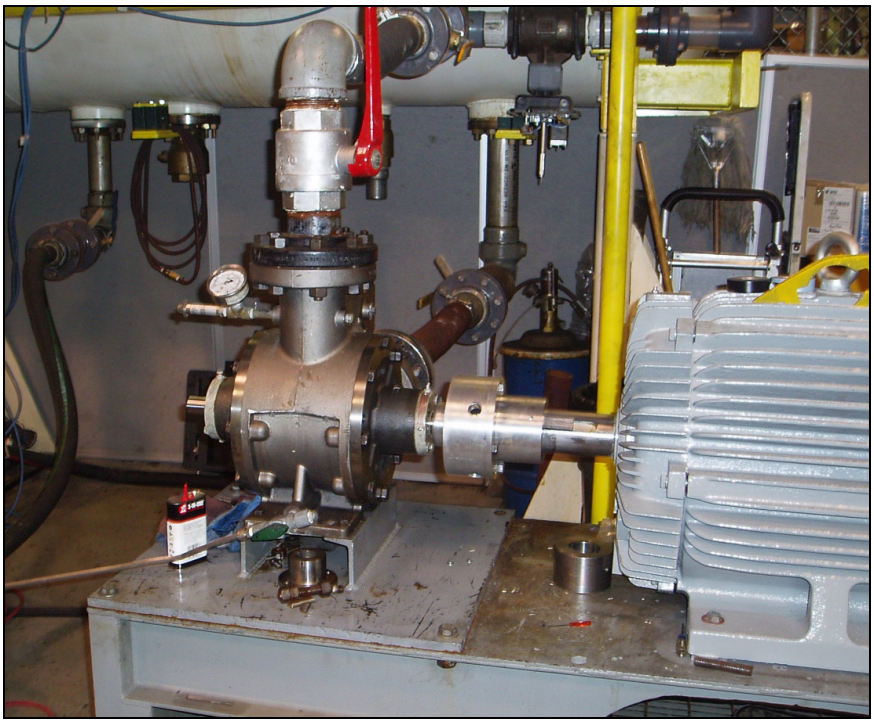

Figure 3.36: Photograph of Direct Drive Setup

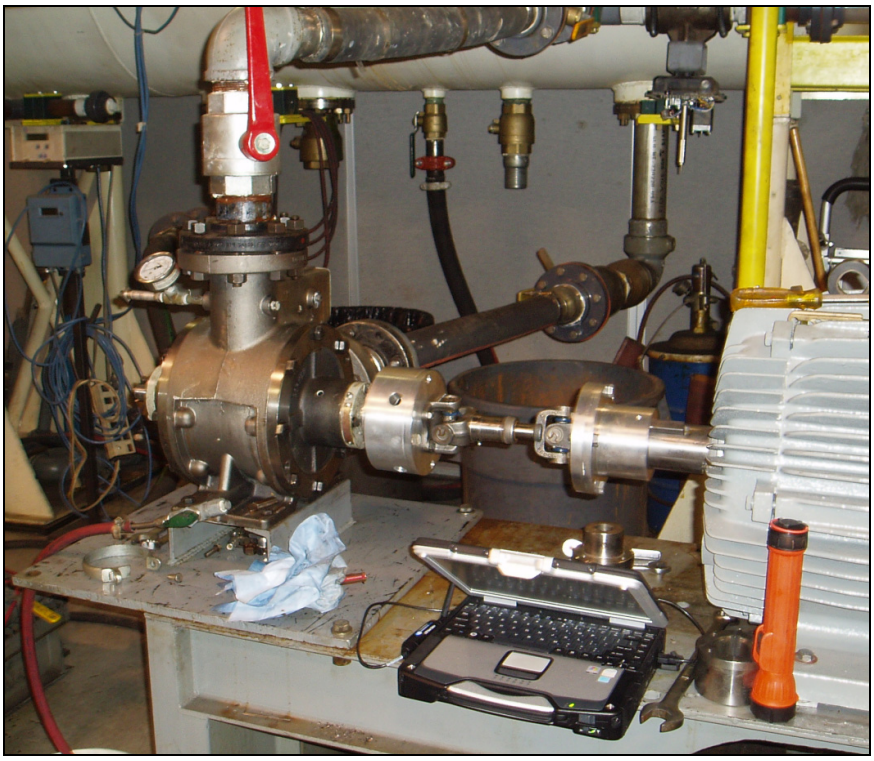

Figure 3.37: Photograph of U-Joint Setup

Due to radio signal transmission issues from the MicroStrain telemetry hardware, the telemetry hardware was configured to operate in a data logging mode. The sample rate frequency was set to a value of 512 Hz. Although the telemetry hardware was physically capable of sample rates in excess of 2000 Hz, due to the technical issue regarding the negative signal drift it was recommended by the manufacture to limit the sample rate frequency to a level of 512 Hz or below. Because of this reduced sample rate frequency, the pump rotational speed during the experimentation would be limited to a maximum of 200 RPM. The rotational speed limitation was imposed to prevent data aliasing of the strain measurements by ensuring a maximum of 2.34° of angular rotation per sample.

Measurements of the applied torque to the pump shaft were to be taken indirectly via a feedback signal coming from the variable frequency drive (VFD) used to power the electric motor. The feedback signal was provided as a percentage of the maximum nominal torque based upon the nameplate rating of the electric motor. Table 3.7 provides the nameplate specifications of the electric motor as it pertains to torque. Based on the parameters provided in Table 3.7 and through the use of Equation 3.3 the maximum nominal torque could be determined. Finally, the actual torque applied to the pump shaft during the experiment could be determined by multiplying the measured percentage of toque against the maximum nominal torque.

Horsepower	50
Frequency	60 Hz
Nominal Speed	885 RPM

Table 3.7: Nameplate Specifications of the Electric Motor

$$HP = \frac{T \times N}{63024} \tag{3.3}$$

$T \equiv \text{Torque in lbf - in}$

$N \equiv \text{Rotational speed in RPM}$

It is acknowledged that due to the indirect nature of the torque measurement some error max exists. In addition, due to the sample rate used by the VFD instantaneous values for torque were not possible. The torque values recorded were the average values observed during peak loading of the pump shaft during the structural response experiments.

Prior to commencement of the experiment both shunt calibration and zero offsetting were performed on the telemetry system. One possible source for error identified pertained to any initial bending strain due to the weight of the rotor, which may or may not be included in the zero offsetting procedure depending on the initial orientation of the shaft at the time the zero offsetting was performed. However, it was assumed that the strain contributions due to bending would be negligible.

The experiment was conducted in four separate phases:

1) Initiation of telemetry equipment for a period time to allow for signal settling.
2) Begin rotation of the pump at 150 RPM with 0 psi differential pressure and hold.
3) Throttle discharge valve to a pump discharge pressure of 125 psi and hold. Record average of torque feedback signal.
4) Fully open the discharge valve bringing the discharge pressure to 0 psi and turn of the electric motor.
5) Download the data from the telemetry hardware.

Phase 1 of this experiment was required to allow ample settling time per the telemetry hardware sampling issues described previously in Section 3.4.2.2. Phase 2 was to allow the pump rotational speed to settle after ramping up from 0 RPM. Phase 3 allowed for a brief period to ramp the pressure from 0 psi to 125 psi and then hold at 125 to acquire strain data for during pump rotations.

Figure 3.38 shows an excerpt of the data collected during five rotations of the pump shaft using the direct coupling setup. The actual acquired data for each of the three individual strain gauges of the rosette are labeled as Strain 1, Strain 2, and Strain 3 corresponding to the strain gauge rosette layout shown in Figure 3.19. The derived 1st principal strain is labeled as Principal Strain 1 in Figure 3.38. The 1st principal strain data contains sharp increase from roughly 230 μS to over 270 μS. This sharp increase in principal strain was interpreted as being a product of binding due to misalignment between the pump and the motor via the coupling / telemetry housing. The applied torque measured at peak pressure during this experiment was 76%, which corresponds to an actual torque value of 2706 lbf-in.

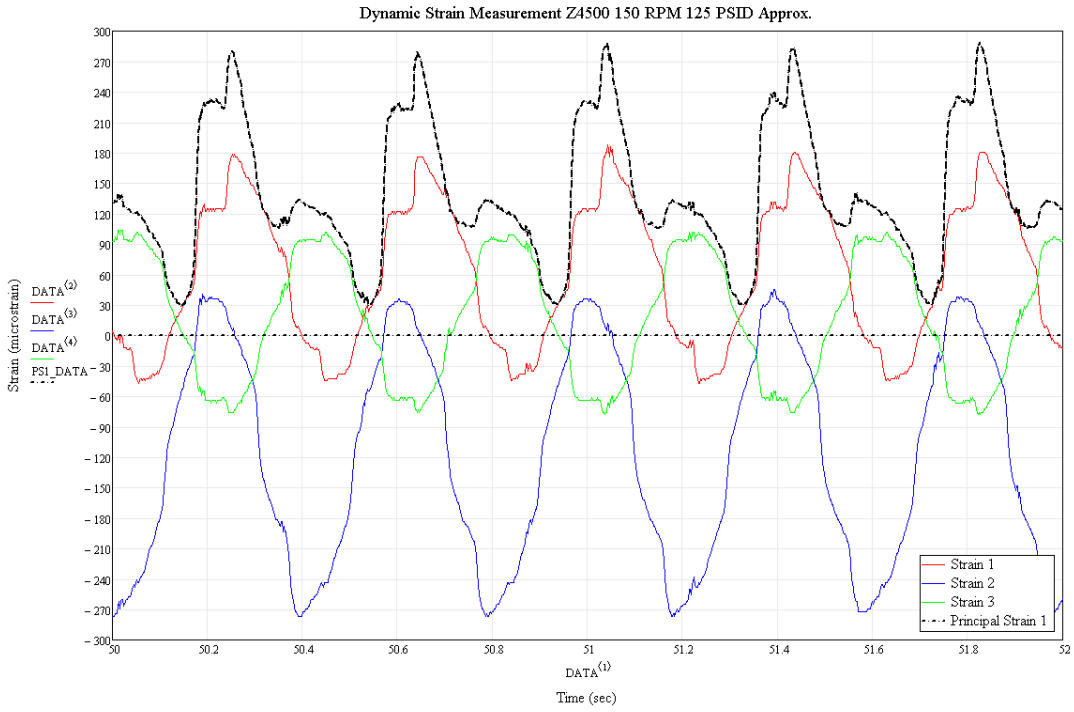

Figure 3.38: Excerpt of Strain Data Showing Five Shaft Rotations

To address the possibility of any rotational binding due to misalignment between the pump and the motor, the experimental setup was modified to include a double universal joint assembly between the pump and the motor as shown in Figure 3.37. In addition, a more rigorous approach was taken to examine the structural response over a range of pump discharge pressures and rotational speeds. The structural response of the pump shaft was to be measured at 100, 150, and 200 RPM, while additionally varying the discharge pressure by 25, 75, and 125 psi. Once again, prior to commencement of the series of experiments shunt calibration and zero offsetting were performed on the installed telemetry hardware. At each one of the rotational speeds and discharge pressures previously listed the following experimental procedure was executed:

1) Initialize the telemetry hardware and acquire data for 30 seconds prior to starting the electric motor. This was to account for the settling time issue.
2) With the telemetry equipment still acquiring data start the electric motor with the discharge valve fully open and the pump discharge pressure at approximately 0 psi for 30 seconds.
3) Throttle the discharge valve towards the closed position until the discharge pressure has reached required value. Maintain the discharge pressure for 30 seconds while the telemetry hardware continues to acquire data. Record average of torque feedback signal.

4) Fully open the discharge valve bringing the discharge pressure to 0 psi and turn of the electric motor.
5) Download the data from the telemetry hardware.

Figures 3.39 through 3.47 are the experimental strain results at each discharge pressure and pump rotational speed previously indicated. The sudden increases in principal strain can be seen in all nine data sets. In addition, both sharp increases and decreases in measured strain of the individual rosette grids is observed in all nine data sets as well. The magnitude of the sudden changes in the measured and derived strain values appear to be related to the pump discharge pressure. As the pump discharge pressure is increased the magnitude of the sharp changes in strain measurements increases as well. However, the sharp changes in strain measurements appear to be insensitive to pump rotational speed.

The data presented in Figures 3.39 through 3.47 pertaining to pump discharge pressures exhibite signs of signal noise in the strain measurements. This is too be expected somewhat given the experiments were conducted in an industrial setting in the presence of a variable frequency drive, which are known to be a major source of signaling noise.

Table 3.8 provides the average torque measured for each of the nine experiments conducted. While the data collected pertaining to torque was in the form of percentage of motor nameplate torque, the data presented in Table 3.8 has been converted to the actual torque values for convenience. The data reveals the applied shaft torque has a strong dependence on pump discharge pressure, while being fairly insensitive pump speed.

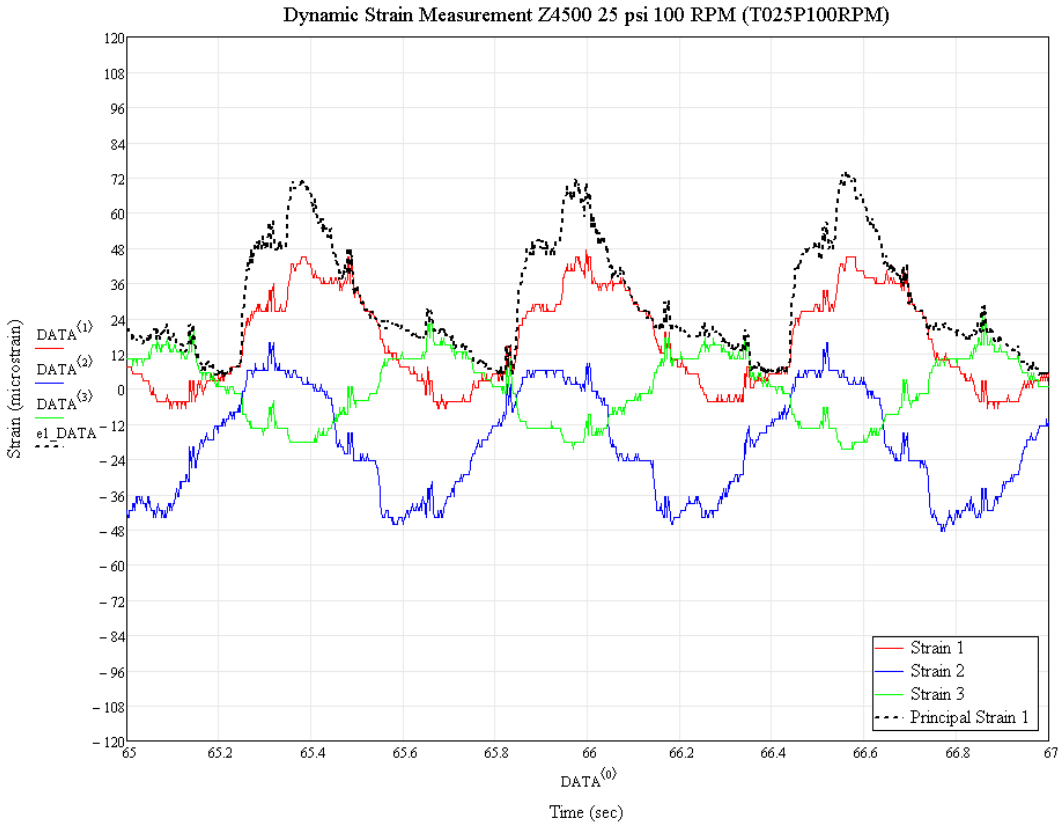

Figure 3.39: Strain Data at 100 RPM and 25 psi Discharge Pressure

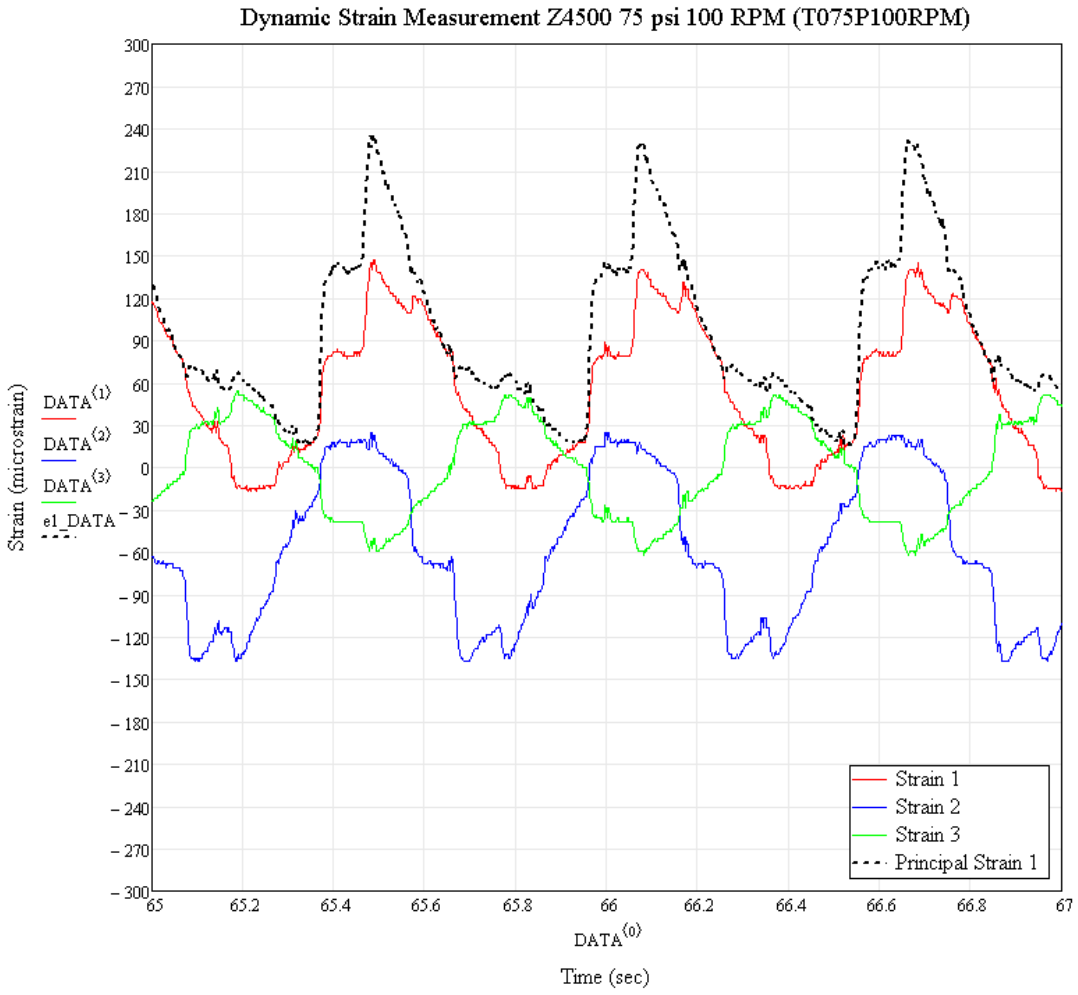

Figure 3.40: Strain Data at 100 RPM and 75 psi Discharge Pressure

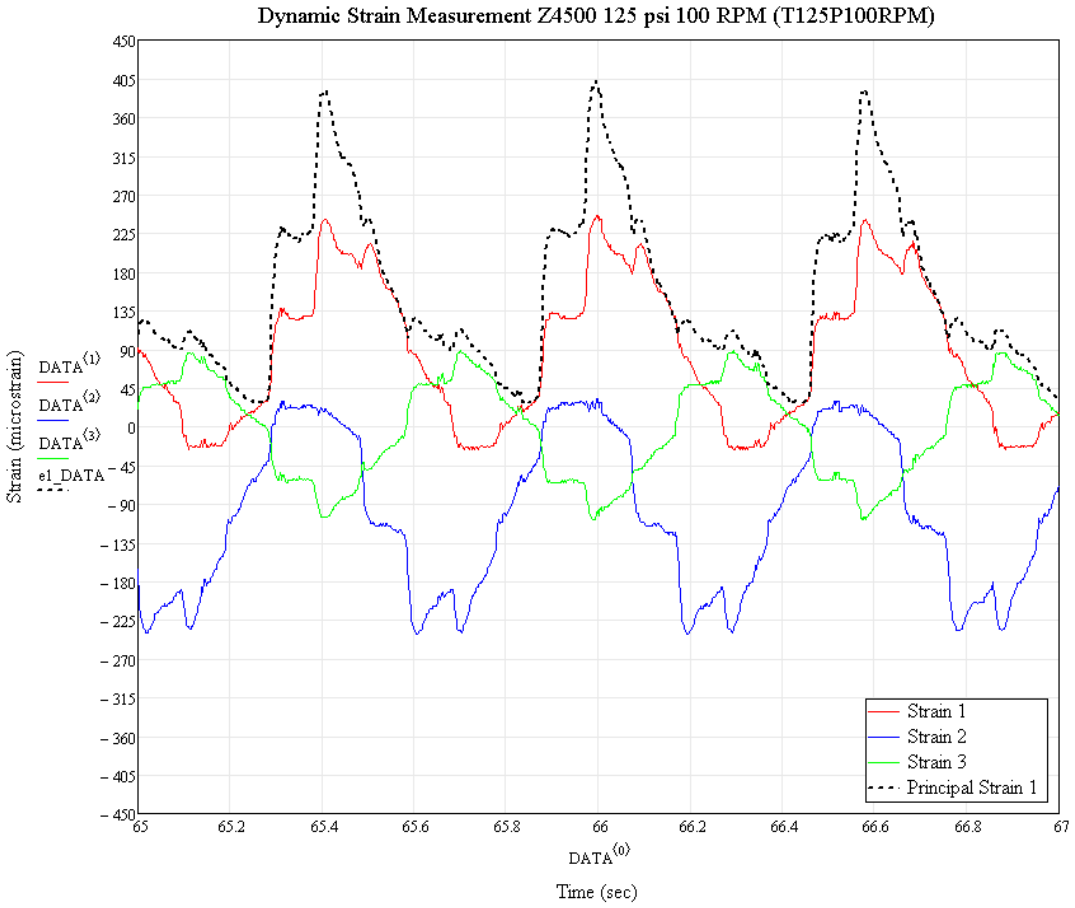

Figure 3.41: Strain Data at 100 RPM and 125 psi Discharge Pressure

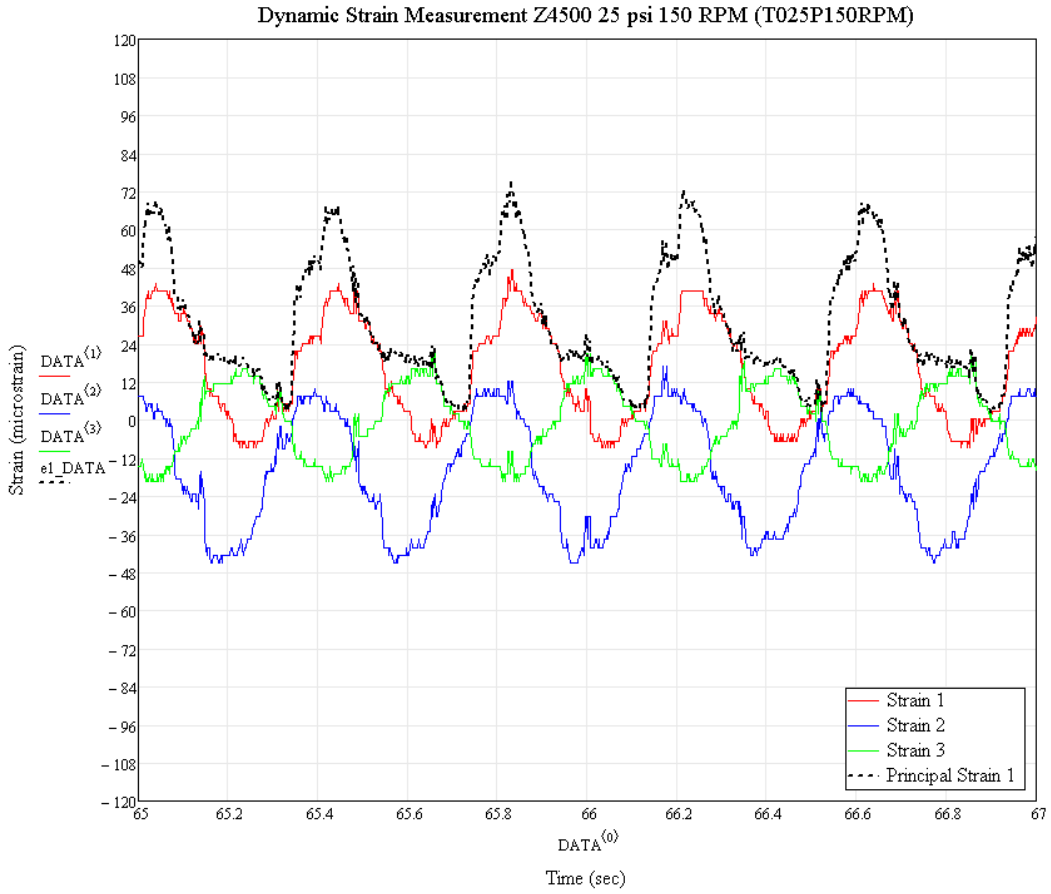

Figure 3.42: Strain Data at 150 RPM and 25 psi Discharge Pressure

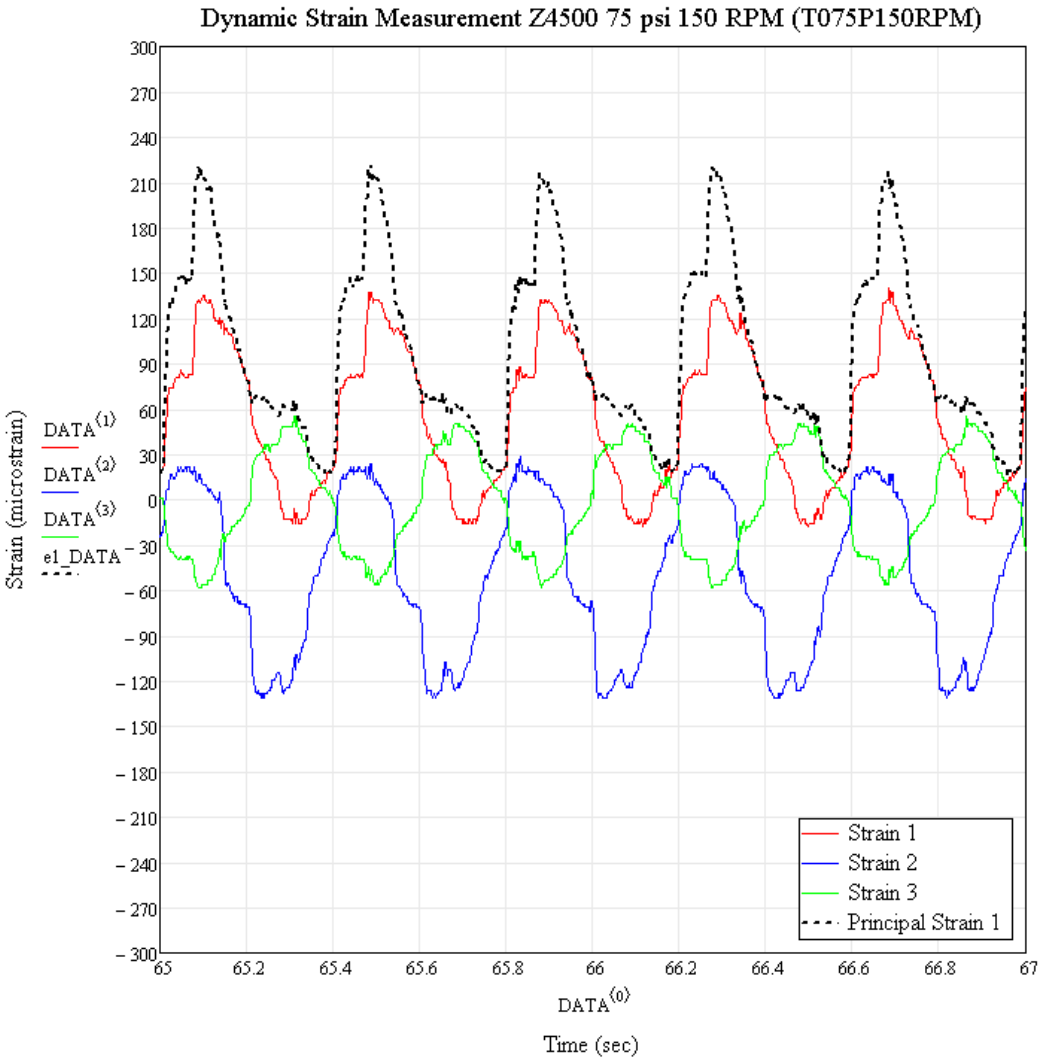

Figure 3.43: Strain Data at 150 RPM and 75 psi Discharge Pressure

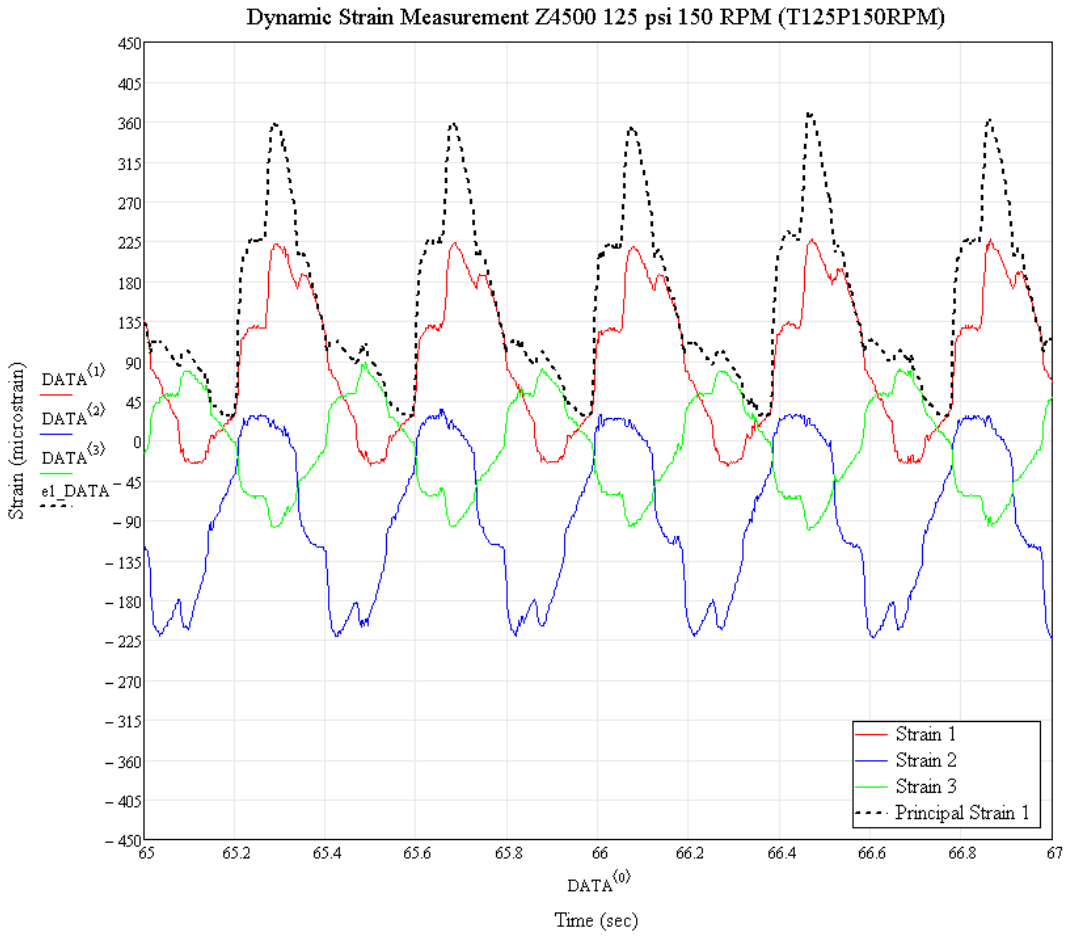

Figure 3.44: Strain Data at 150 RPM and 125 psi Discharge Pressure

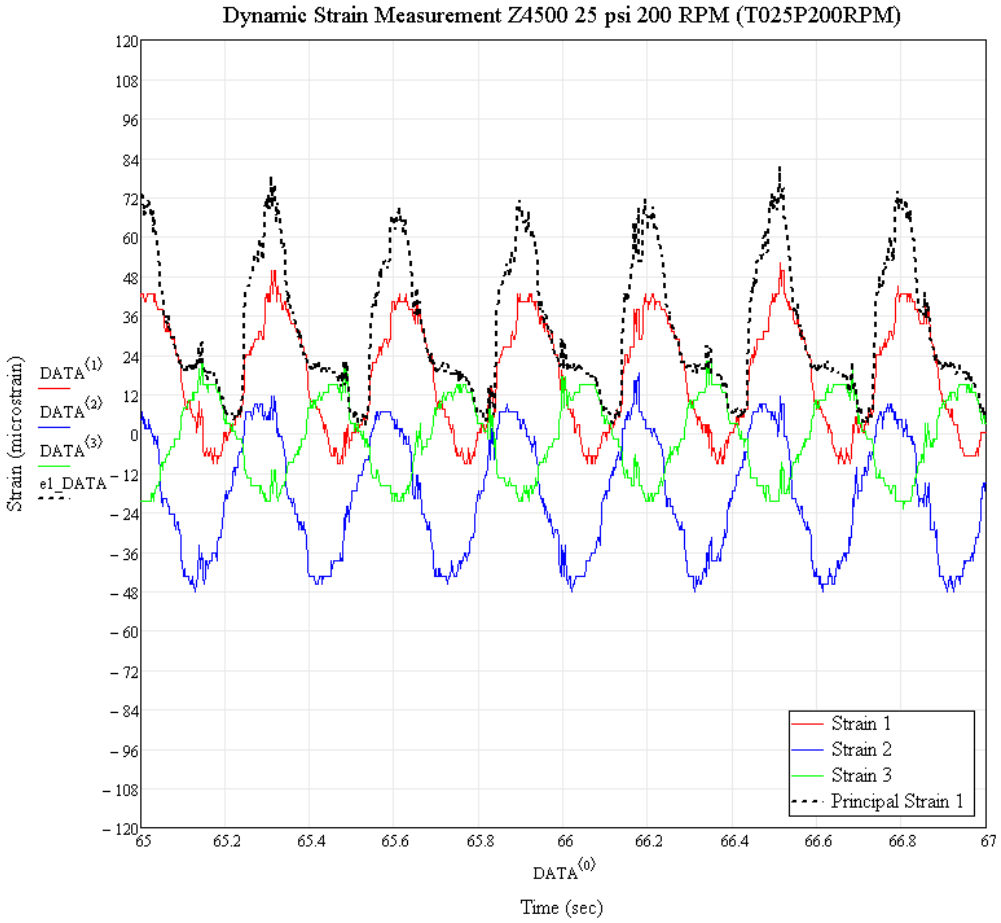

Figure 3.45: Strain Data at 200 RPM and 25 psi Discharge Pressure

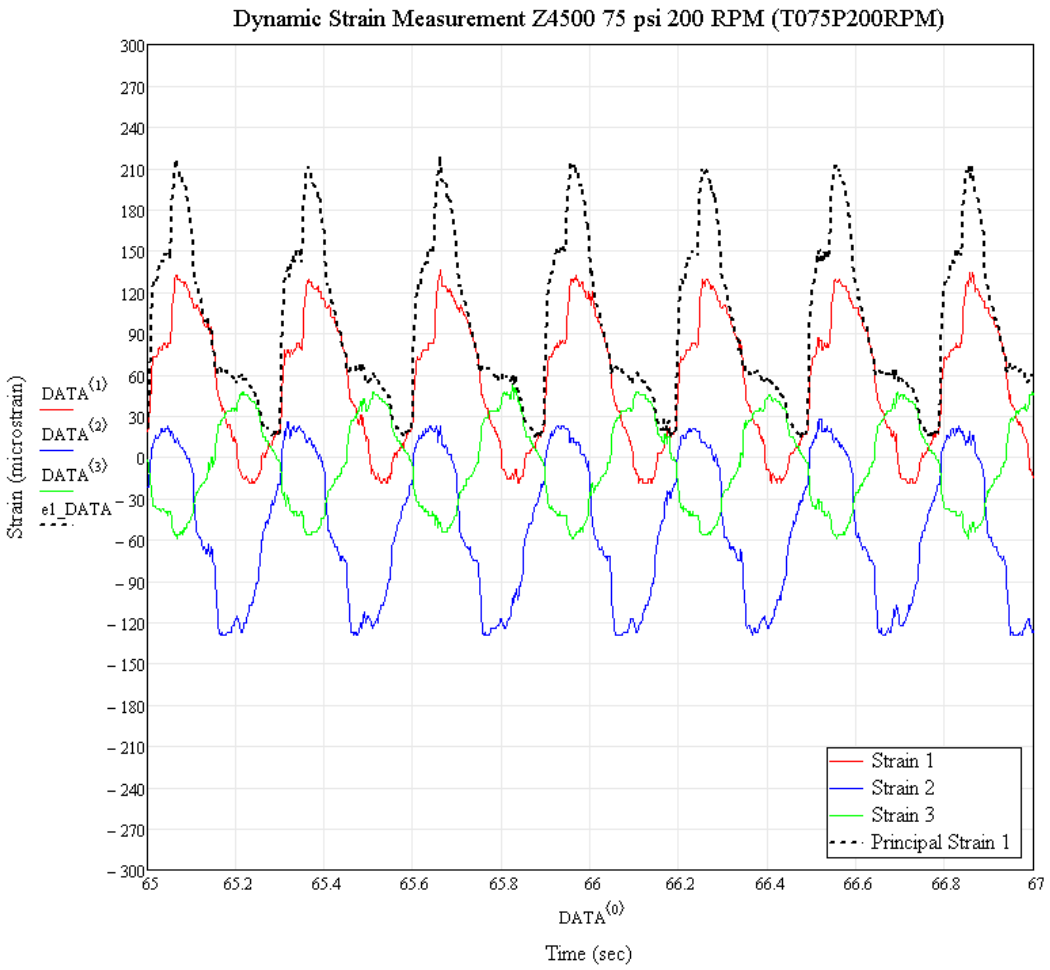

Figure 3.46: Strain Data at 200 RPM and 75 psi Discharge Pressure

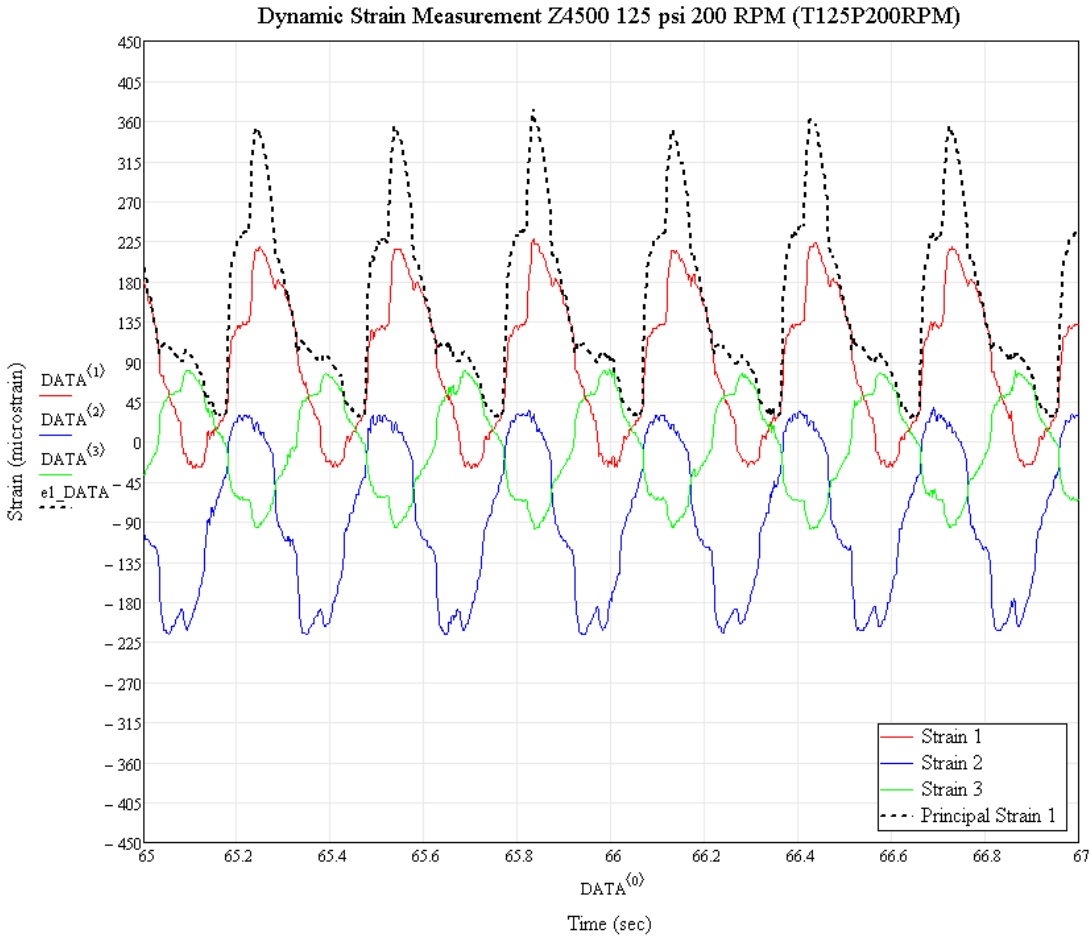

Figure 3.47: Strain Data at 200 RPM and 125 psi Discharge Pressure

	Pump Discharge Pressure		
Pump Rotational Speed (RPM)	**25 psi**	**75 psi**	**125 psi**
100	641	1709	2671
150	605	1674	2742
200	605	1674	2635

Table 3.8: Torque Measurements (lbf-in) Results Matrix

CHAPTER IV

NUMERICAL SIMULATION MODELS

4.1 Introduction

In order to gain better insight into the state of the stress and strain of the pump shaft several numerical simulation models were created utilizing the finite element method. Three dimensional simulations were performed first by importing geometry into the commercially available general purpose finite element solver Ansys. After performing various minor geometrical simplifications on each of the simulation models, the solid bodies were meshed, material properties applied, and boundary conditions were set on all applicable surfaces. Most of the models required contact elements to simulate either interference press fits or shrink fits, therefore contact elements with frictional coefficient parameters were added where applicable. The results from the numerical simulations would not only provide insight into the stress and strain distributions throughout the pump shaft, but also serve as a basis for comparison against experimental data.

4.2 Numerical Simulation Elastic and Plastic Material Properties

All of the numerical simulations described in this chapter were performed on the pump shaft, seal drive pin, rotor, or a combination thereof. Table 4.1 lists the components used in the following numerical simulations along with the respective components material name.

Component Name	**Material Name**
Pump Shaft	8620 Steel
Rotor	65-45-12 Ductile Iron
Seal Drive Pin	1020 Steel

Table 4.1: Component Material Specifications

The numerical simulations performed to determine the stress, strain, and displacements of previously listed components were conducted with a combination of elasticity and plasticity material models. Regarding the elasticity material models, Table 4.2 provides the linear elastic material properties used in the subsequent numerical simulations.

Material Description	Modulus of Elasticity (lbf/in^2)	Poisson's Ratio
8620 Steel	2.97e7	0.29
1020 Steel	2.95e7	0.29
65-45-12 Ductile Iron	2.44e7	0.29

Table 4.2: Linear Elastic Material Properties

It can be seen in Figures 3.4 through 3.9 that during the pinning of the seal drive pin into the pump shaft plastic deformation occurs around the outer diameter of the seal drive pin hole. Also, by observation it is noted that the seal drive pin itself also undergoes plastic deformation as well. In order to obtain a representation of the stresses and strains associated with the pinning operation numerical simulations requiring plasticity must be performed. The general finite element solver Ansys has the capability of simulating plastic deformation through the use of its Multilinear Isotropic Hardening plasticity model, which is based on the von Mises yield criterion. In order to utilize this plasticity model within Ansys a set of data points representing the true stress versus the true plastic strain must be provided for the individual material along with the respective linear elastic property parameters. Since it is well assumed that the only two components that undergo any plastic deformation are the shaft and the seal drive pin, true stress versus true plastic strain data will only be created for their respective materials.

To obtain the true stress versus true plastic strain data set for the 8620 steel material the tensile test data obtained during the metallurgical review of the material, shown in Figure 3.1, was first converted to a true stress-strain curve using Equation 4.1 and 4.2 [14]. Then the true stress-strain data beyond the yield point had the elastic component of the strain removed resulting in a data set of true stress versus true plastic strain as shown graphically in Figure 4.1.

$$\sigma_{true} = \sigma_{eng}\left(1 + \varepsilon_{eng}\right) \tag{4.1}$$

$$\varepsilon_{true} = \ln\left(\varepsilon_{eng} + 1\right) \tag{4.2}$$

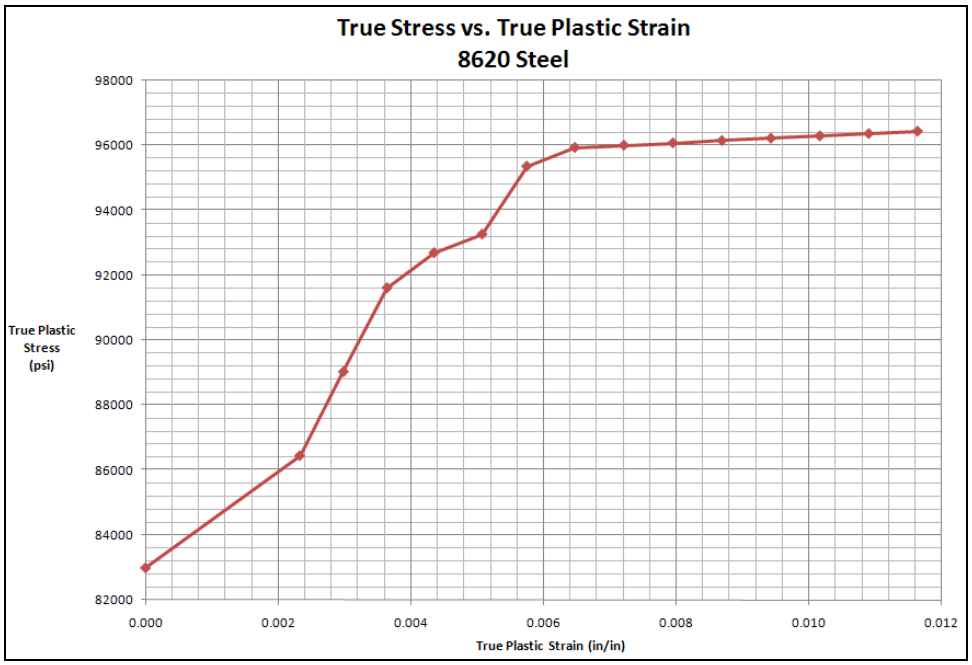

Figure 4.1: True Stress versus True Plastic Strain for 8620 Steel

To obtain the true stress versus the true plastic strain data set for 1020 steel, given that actual test data did not exists, both Hertzberg [14] and Stephens et al. [15] present the "Ramberg-Osgood relationship" in Equation 4.3 where true stress is defined as a power function of the strength coefficient K, plastic strain ε_p, and the strain hardening exponent n. The total true strain is then given by equation 4.4 where E is the modulus of elasticity. The parameters for Equations 4.3 and 4.4 pertaining to 1020 steel are given in Table 4.3. The resulting set of true stress versus true plastic strain for 1020 steel is shown graphically in Figure 4.2.

$$\sigma = K(\varepsilon_p)^n \tag{4.3}$$

$$\varepsilon = \varepsilon_e + \varepsilon_p = \frac{\sigma}{E} + \left(\frac{\sigma}{K}\right)^{\frac{1}{n}} \tag{4.4}$$

Parameter	Value
Yield Strength	38,000 psi
Modulus of Elasticity (E)	2.95e7 psi
Strength Coefficient (K)	107000
Strain Hardening Exponent (n)	0.19

Table 4.3: Parameters for Equations 4.3 and 4.4 for 1020 Steel

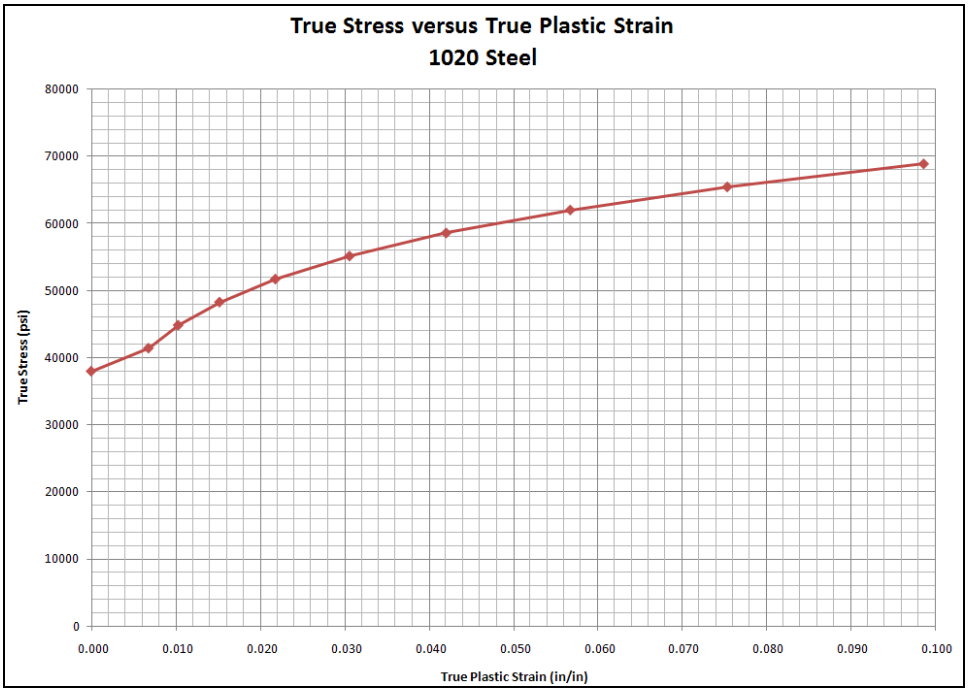

Figure 4.2: True Stress versus True Plastic Strain for 1020 Steel

4.3 Material Fatigue Properties

To examine the pump shafts ability to withstand fatigue failure the mechanical fatigue properties must be established. The stress-life approach will be utilized in comparing the applied stresses to the established fatigue limits in order to determine if fatigue failure is likely. However, fatigue property data is difficult to obtain for AISI 8620. Concessions had to be made in order to establish a value for the endurance limit that would be utilized in evaluating the likelihood of fatigue failure..

Figure 4.3 provides the S-N curves for nitrided and quenched and tempered AISI 8620 steel [17]. According to Figure 4.3 the endurance limit for quench and tempered 8620 appears to be approximately 30,000 psi. However, the process for manufacturing 8620 with a Brinell Hardness Number (BHN) of 207 requires a quench and temper at a temperature of 300°F as opposed to 1050°F as indicated on the S-N curve, thereby indicating a significant difference in hardness which would imply a significant difference in mechanical properties as well.

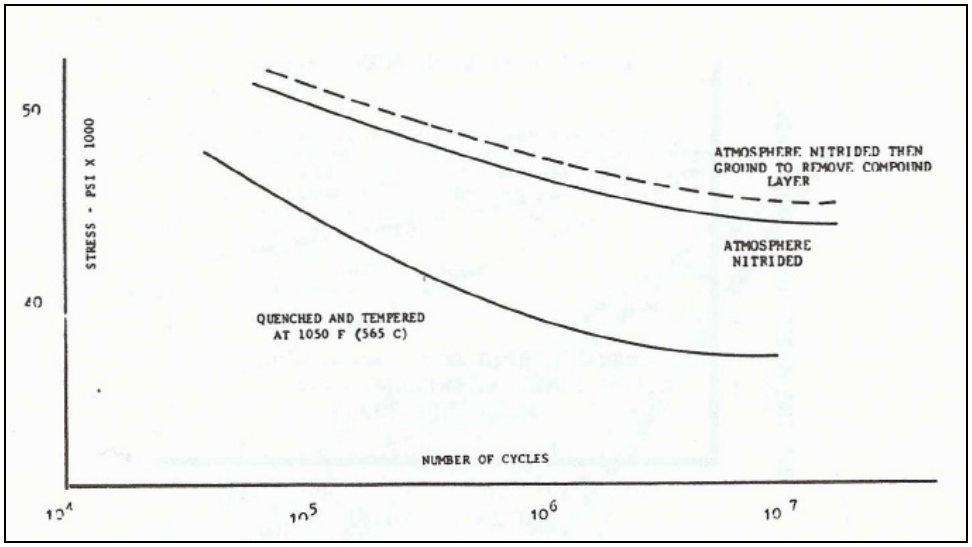

Figure 4.3: S-N Curves for Nitrided and Quenched and Tempered 8620

Table 4.4 provides the tensile and fatigue properties for various steel alloys based on three different types of heat treatments. While 8620 is not listed in Table 4.4, 8630 is listed with either a normalized and tempered heat treatment or a quench and tempered heat treatment. The yield strength of the normalized and tempered 8630 is slightly higher than the yield strength of the 8620 material reported in Table 1.1. Therefore treating 8620 at a BHN of 207 as having similar mechanical properties as 8630 normalized and tempered, the 8620 material can then be treated as having an endurance limit of 54,000 psi to 33,100 psi for unnotched and notched specimens, respectively.

Steel	Tensile strength		Endurance limit				Fatigue endurance ratio		Fatigue notch sensitivity factor, *q*
			Unnotched		Notched				
	MPa	ksi	MPa	ksi	MPa	ksi	Unnotched	Notched	
Normalized and tempered									
1040	648	94	260	37.7	193	28	0.40	0.30	0.29
1330	685	99.3	334	48.4	219	31.7	0.49	0.32	0.44
1330	669	97	288	41.7	215	31.2	0.43	0.32	0.28
4135	777	112.7	353	51.2	230	33.3	0.45	0.30	0.45
4335	872	126.5	434	63	241	34.9	0.50	0.28	0.68
8630	762	110.5	372	54	228	33.1	0.49	0.30	0.53
Quenched and tempered									
1330	843	122.2	403	58.5	257	37.3	0.48	0.31	0.48
4135	1009	146.4	423	61.3	280	40.6	0.42	0.28	0.43
4335	1160	168.2	535	77.6	332	48.2	0.46	0.29	0.51
8630	948	137.5	447	64.9	266	38.6	0.47	0.27	0.57
Annealed									
1040	576	83.5	229	33.2	179	26	0.40	0.31	0.23

Table 4.4: Mechanical and Fatigue Properties for Several Cast Alloy Steels

Since no exact value regarding the endurance limit for AISI 8620 steel at a hardness of 207 BHN exists, based upon the data in Figure 4.3 and Table 4.4 the endurance limit will be taken as a minimum of 30,000 psi to a maximum of 54,000 psi where the minimum will be used where stress concentrations exist.

4.4 Press Fit Numerical Simulation Model

The goal of this press fit operation numerical simulation is to both simulate the plastic deformation and stresses involved with the press fit operation and to also determine the resulting elastic stress field around the hole, which would serve to increase the fatigue crack propagation rate if a flaw were to exist.

The geometry used for this simulation was a three dimensional CAD model of the pin inserted into the drilled hole within the shaft. Nominally, the interference between the pin and the hole is radially 0.001 inches. Only half of the pump shaft model was utilized in order to simplify the simulation model. In addition, a majority of the motor side of the model, which would have represented the unconstrained portion of the shaft, was eliminated to further simplify the simulation model. Figure 4.4 is an illustration of the CAD geometry used for the simulation with a sectioned view of the assembly shown in the bottom left corner. The elastic and plastic material properties for each component are given in Section 4.2.

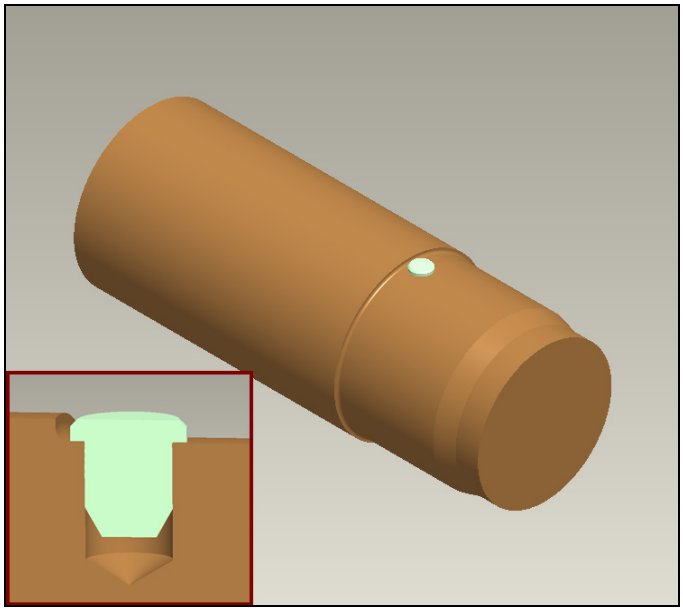

Figure 4.4: 3D Geometry for Press Fit Simulation

Both the pin and the pump shaft were meshed using 10-node tetrahedral elements with additional levels of refinement near the contact surfaces between the pin and the shaft. The maximum element size was set to a value of 0.005 inches in the refined areas of the mesh to adequately capture the stress distributions within those regions. Contacts between surfaces were modeled using the penalty formulation with a sliding frictional coefficient of 0.15. Figure 4.5 provides a picture of the finite element mesh used for this simulation.

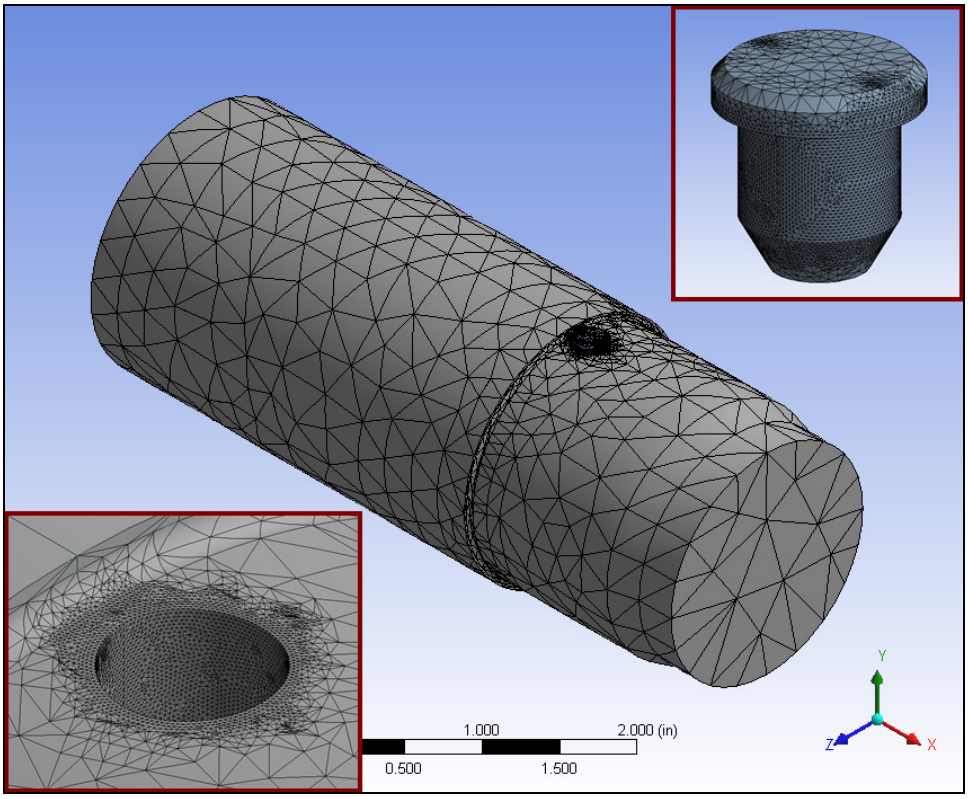

Figure 4.5: Press Fit Simulation Finite Element Mesh

For this numerical simulation no external loads would be included in the model, therefore only displacement constraints were applied to prevent rigid body motion for the static solver. Figure 4.6 shows the sole displacement constraint placed on the symmetry

surface of the pump shaft. Displacements on this surface highlighted in blue were constrained in all three global coordinate directions.

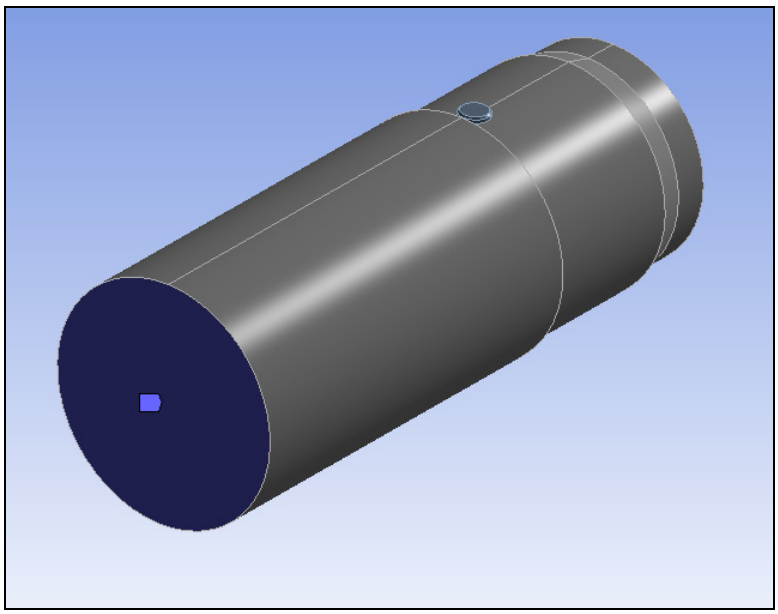

Figure 4.6: Press Fit Simulation Boundary Conditions

Figure 4.7 provides an illustration of the equivalent plastic strain pertaining to the press fit simulation model. The equivalent plastic strain is a measure of the plastic deformation that has occurred where the equivalent plastic strain is non-zero. Regions of the model where the equivalent plastic strains are zero are considered to still be in a state of elastic strain only. As can be seen in Figure 4.7 the plastic deformation is confined to a volumetric region that surrounds the seal drive pin hole in the pump shaft near the outer surface of the shaft. The plastic deformation results shown in Figure 4.7 agree well with the photographs of the pump shaft after the pinning operation as shown in Figures 3.4 through 3.9. Localized regions located around the rim of the seal drive pin hole shown in Figure 4.7 have relatively high equivalent plastic strain values shown in red. These localized regions are considered artifacts of mesh resolution and the distribution of the

equivalent plastic strains around the rim of the seal drive pin hole would be expected to be more evenly distributed had the mesh been more refined.

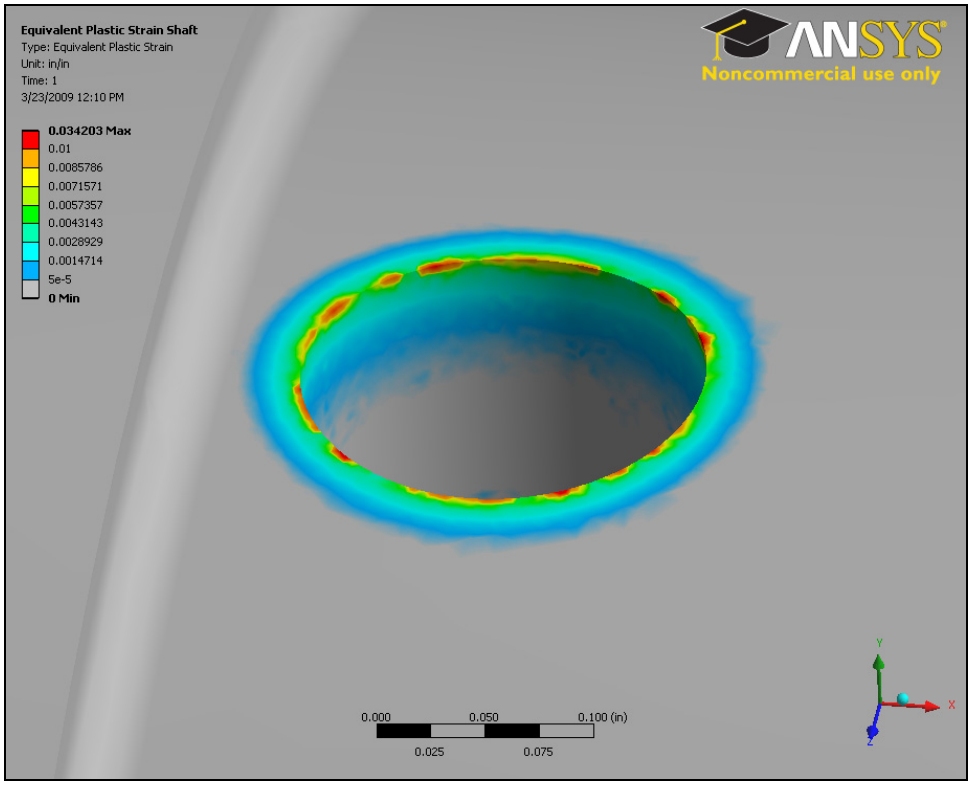

Figure 4.7: Contour Plot of Equivalent Plastic Strain

In order to examine the affect the press fit operation has on the state of stress surrounding the seal drive pin hole Figure 4.8 provides an illustration showing 1st principal stresses and 3rd principal stresses. Large 1st principal stress values indicate a stress state of tension, while negative values of 3rd principal stress indicate a stress state of compression. Figure 4.8 indicates that the region immediately adjacent to the seal drive pin hole located on the outer surface of the pump shaft is in a large state of compressive stress. However, moving out radially from the center of the seal drive pin hole the state of stress changes from compressive to tensile as indicated in Figure 4.8 by the increasing values for both 1st and 3rd principal stresses.

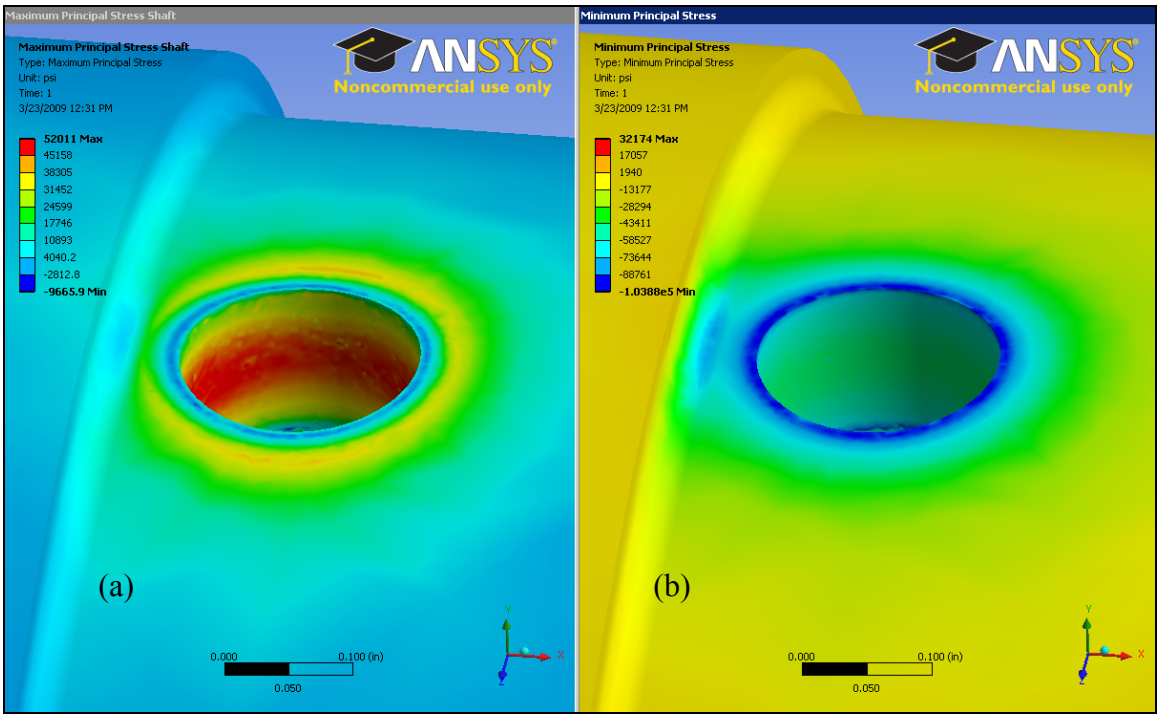

Figure 4.8: Contour Plot of (a) 1st Principal Stress, (b) 3rd Principal Stresses

Given that most pump shaft fractures for the Z4500 pump model have fracture surfaces that pass through the seal drive pin hole normal to the axis of the shaft, a contour plot of the stresses acting in the axial direction is shown in Figure 4.9. The stresses acting normal to the typical crack face reach an approximate peak positive value of 50,600 psi near the seal drive pin hole. However, the tensile stress acting in the axial direction dissipates rapidly as the distance from the hole increases.

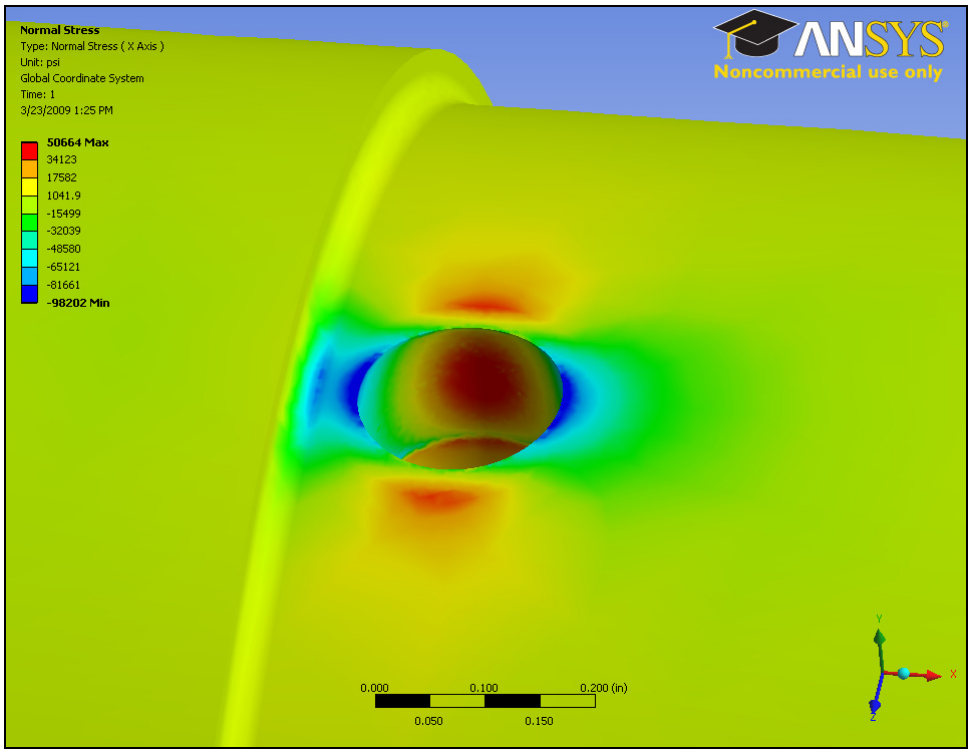

Figure 4.9: Contour Plot of the Stresses Acting in the Axial Direction of the Shaft

4.5 Bending and Torsion Numerical Simulation Model

The goal for this numerical simulation study is to replicate the bending and torsional loads the pump shaft would be subject to during the normal operation of the pump and examine numerically the structural response of the pump shaft. Since the idea is to simulate the strains that would be measurable by strain gauging as performed during the structural response experimentation, only the bending and torsional loads will be included in the numerical simulation model. Meaning, that stresses and strains due to either the press fit of the seal drive pin into the shaft or the shrink fit of the rotor onto the pump shaft would not be modeled. While both the press fit and the shrink fit operations contribute to the total structural response of the pump shaft, these strains were not measured during experimentation due to the fact that the shaft was gauged after both the

press fit and shrink fit operations had been performed. The results from this numerical study will be used as a basis for comparison with some of the experimentation results.

To simulate the structural response of the shaft through one revolution the force vector associated with the bending load due to pressure would be varied angularly, while maintaining the same magnitude throughout. In addition, the applied torque loading would be modeled as constantly applied moment. The numerical simulation model would be analyzed at 2° increments over a complete 360° rotation of the shaft. At each 2° increment the 1st principal strain along with the directional strain associated with the individual grids of the strain gauge rosette would be determined. The results output would be in the form of simulated strains versus rotational angle.

The three dimensional geometry used for this numerical study was the pump shaft and rotor only. Due to symmetry, only half of the pump shaft and rotor assembly was modeled as shown in Figure 4.10. In addition, a small 3 mm surface region was created in the identical location of where the strain gauge rosette was placed during the rotor shaft experimentation, which would be subsequently used for results extraction and comparison against the data obtained during the shaft experimentation. The lower left corner of Figure 4.10 shows the 3 mm circular surface region highlighted in green.

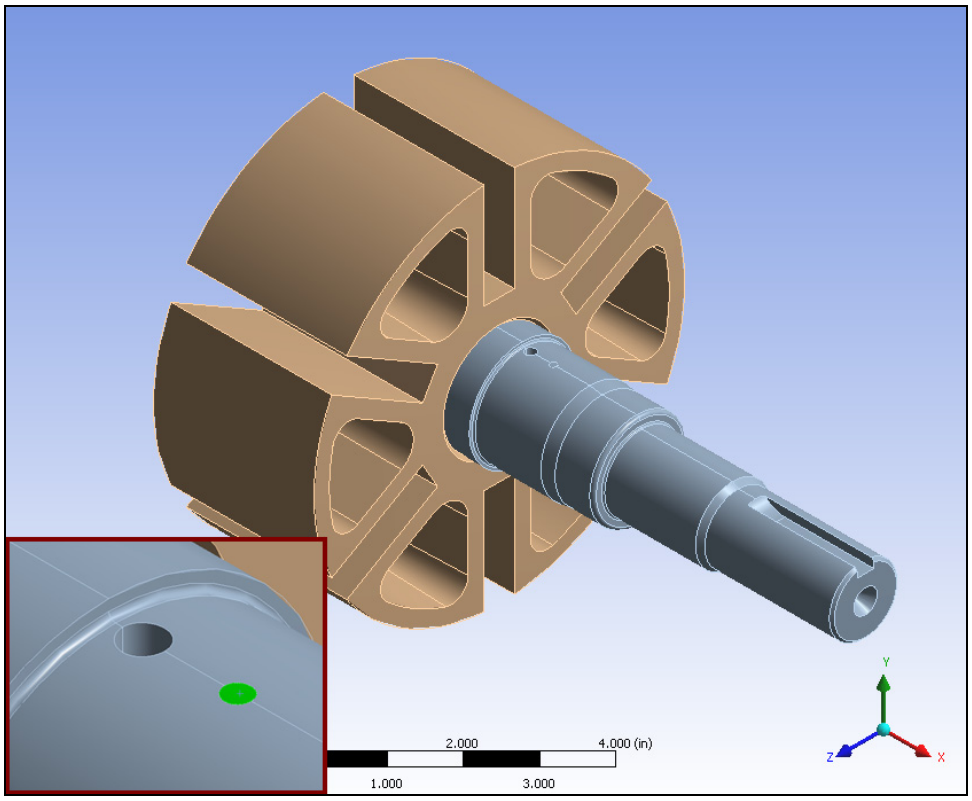

Figure 4.10: 3D Geometry for Bending and Torsion Simulation

Both the shaft and the rotor were meshed with 10-node tetrahedral elements. A series of convergence studies were conducted to determine the optimal mesh density with respect to the strains within the strain gauge surface region. Figure 4.11 provides and illustration of the finite element mesh used for this simulation. Contact elements were created between the shaft and rotor surfaces that contact one another. However, the contact between these two components was modeled as bonded contact in order to not simulate the stresses and strains associated with the shrink fit of the rotor onto the shaft.

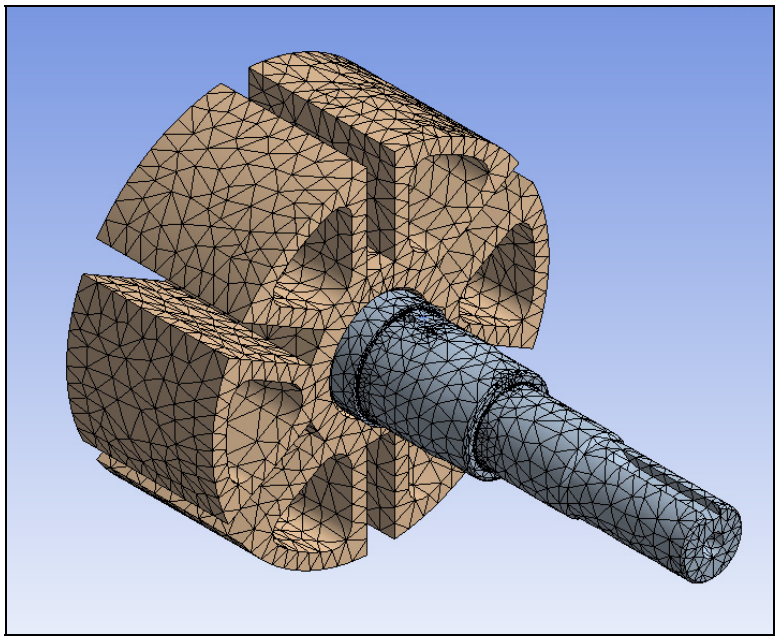

Figure 4.11: Bending and Torsion Simulation Finite Element Mesh

The boundary conditions for this model were a mixture surface constrains, symmetry constraints, and surface loads. The plane of symmetry for the rotor/shaft was constrained such that nodal displacements normal to the symmetry surface were prohibited. However, nodes lying on this symmetry surface could translate parallel to the symmetry plane. Figure 4.12(b) provides an illustration of the simulation model with the symmetry surface highlighted in blue. To simulate the pump bearings a cylindrical surface constraint was applied to the portion of the shaft where the bearing inner races are located. Figure 4.12(c) has the bearing surfaces highlighted in blue. On these surfaces radial translation was constrained, while axial and tangential translations relative to the pump shaft axis were unconstrained. Finally, to prevent rigid body rotation and to simulate the motor driven keyway one of the inner surfaces on the machined keyway in the shaft was constrained. Figure 4.12(d) shows the keyway surface highlighted in blue

where the constraint was applied. Nodes lying on this surface were constrained from any translation normal to the keyway surface; however, translations parallel to the highlighted keyway surface were unconstrained.

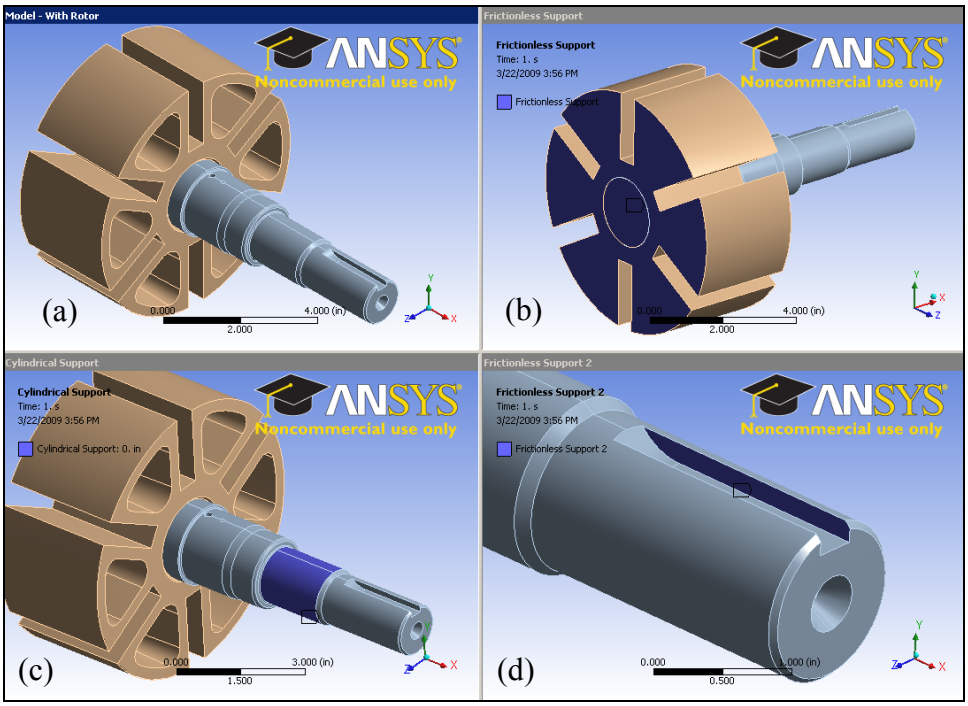

Figure 4.12: Bending and Torsion Finite Element Model Constraints (a) Overall Model, (b) Symmetry Surface Constrain, (c) Cylindrical Bearing Constraint, (d) Keyway Constraint

The only two numerical simulation model loads were the torsional load due to the applied torque from the motor and the resultant bending force due to the pressure differential across the rotor. Figure 4.13(a) shows partially the surfaces in which the moment load was applied highlighted in red. A total moment load of 2706 lbf-in was evenly distributed across six faces located in the vane slots of the rotor. Figure 4.13(b) illustrates the rotor surfaces highlighted in red in which the resultant bending load due to differential pressure was applied. The total resultant bending was calculated from

Equation 4.5 and the parameters listed in Table 4.5 where the total resultant bending force was based on the average pump discharge pressure multiplied by the cross sectional area of the rotor. The magnitude of the resultant bending load was 5069 lbf, however this magnitude was reduced by half to a value of 2534.5 lbf to account for the model symmetry

$$F = P(L_R d_R) \tag{4.5}$$

Parameter	Value
Pump Discharge Pressure (P)	125 psi
Length of Rotor (L_R)	5.912 in
Diameter of Rotor (d_R)	6.859 in

Table 4.5: Parameters for Equations 4.5

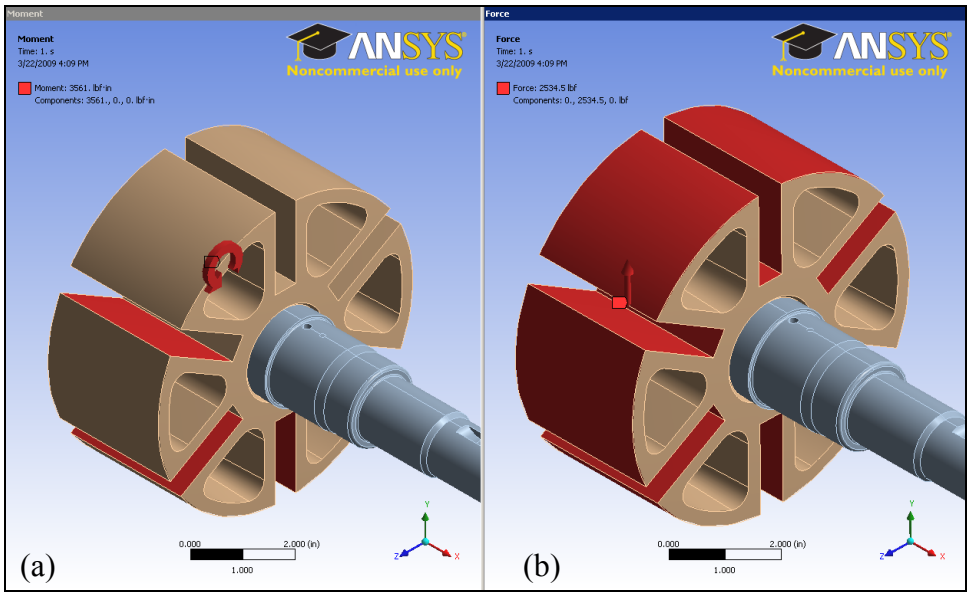

Figure 4.13: (a) Applied Moment Load and (b) Applied Force

The results from the numerical simulation of the strains in the region of the strain gauge for the bending and torsion model are shown in Figure 4.14. The strain values obtained in these results are an average of the maximum and minimum values obtained over the strain gauge surface region in the model. As one would expect, the results are sinusoidal in nature. In the next chapter these numerical simulation results will be overlaid upon the actual test data in order to evaluate correlation between the numerical model and the experimentation results.

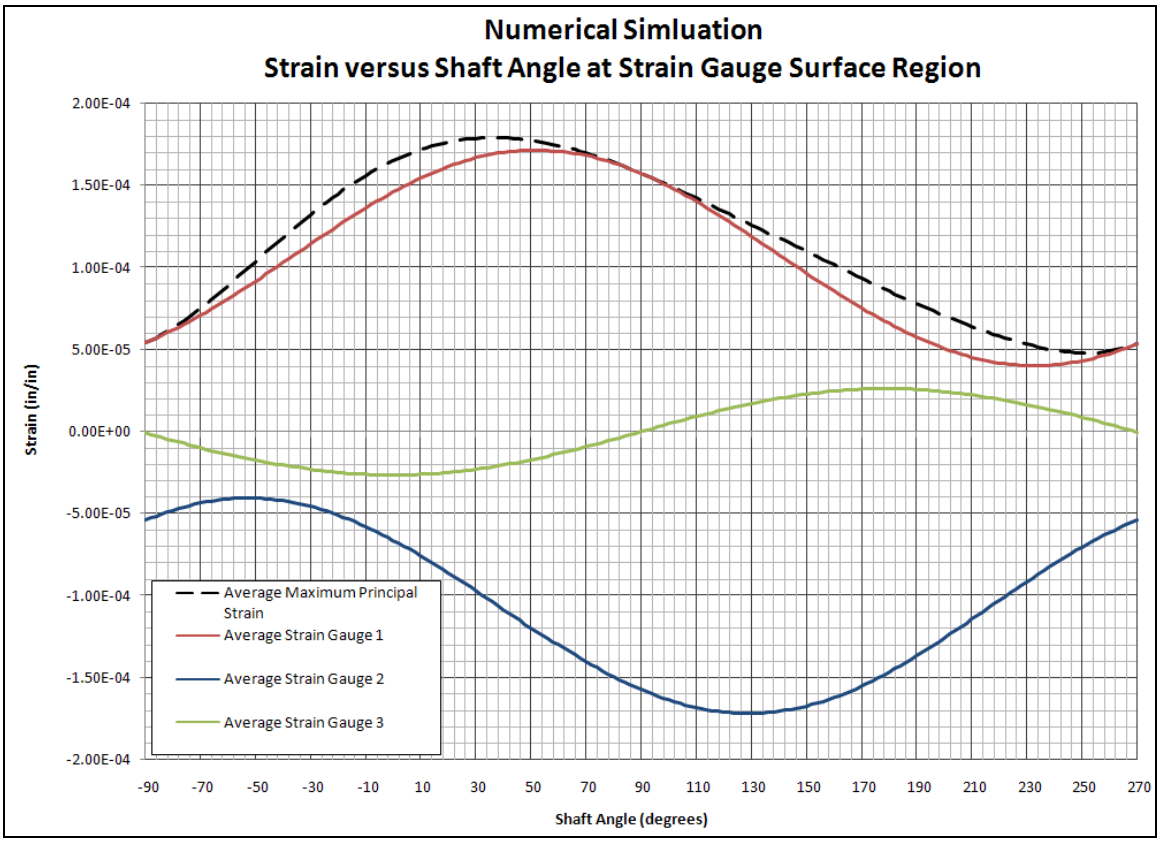

Figure 4.14: Numerical Simulation Results in the Region of the Strain Gauge

4.6 Total Stress Numerical Simulation Model

In order to determine the total state of stress of the pump shaft due to the press fit of the seal drive pin, the shrink fit of the rotor onto the shaft, and the bending and torsional load during operation of the pump a numerical simulation model must be created that includes provisions for all three of these loading scenarios. However, the stress state of the pump shaft will also be a function of the shaft angle. Therefore, this numerical study will be conducted in a similar manner to the simulation model described in Section 4.5 in that the load vector stemming from the pump discharge pressure will be varied angularly over a full 360° in 2°. At each angular increment the maximum 1st principal stress, equivalent plastic strain, and maximum 1st principal strain will be evaluated and plotted to create a graph of the structural response as a function of shaft angle. The results stemming from this numerical simulation will be used in comparison with the yield and fatigue properties of the pump shaft material to determine the likelihood of material yielding or fatigue failure.

The geometry utilized for this numerical simulation was an assembly model of the pump shaft, the rotor, and the seal drive pin. Due to symmetry, only half of the geometry assembly would be analyzed as shown in Figure 4.15. The elastic and plastic material properties for each of the components within this geometrical assembly are the same as those prescribed in Section 4.2.

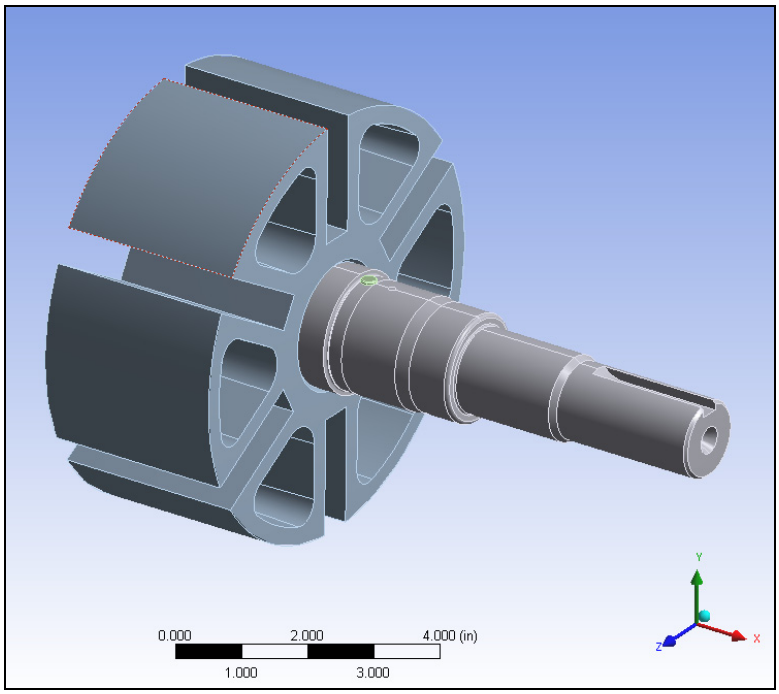

Figure 4.15: Geometry for Total Stress Numerical Simulation Model

The entire model was meshed with 10-node tetrahedral elements. The mesh was refined on the surfaces where the seal drive pin comes into contact with the pump shaft drill hole in order to adequately capture the stress gradients involved with plastic deformation. Figure 4.16 provides a graphic showing the simulation model mesh. Contact elements were created between the contacting surfaces of the rotor and the shaft and the contacting surfaces of the seal drive pin and the shaft.

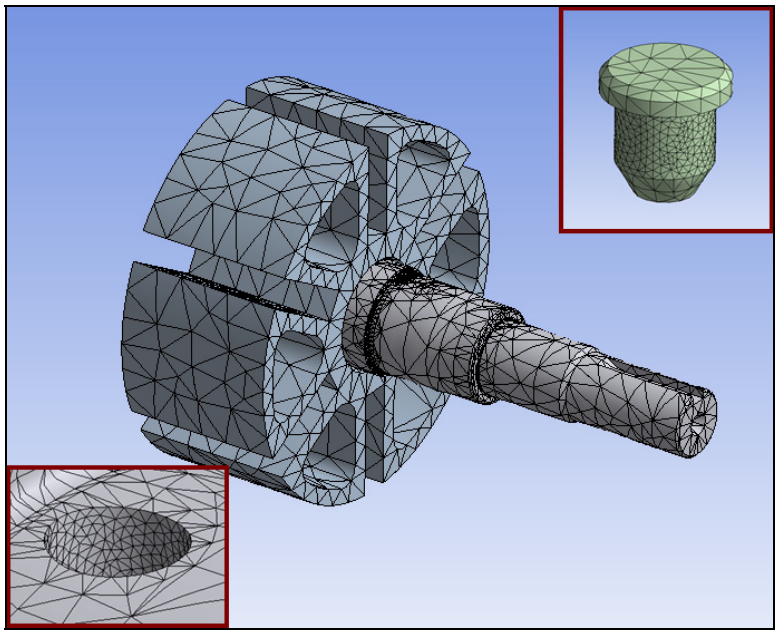

Figure 4.16: Finite Element Mesh of Pump Shaft Rotor Assembly with Pin

The displacement constraint boundary conditions for this numerical simulation model were identical to those prescribed Section 4.5 and graphically shown in Figure 4.12. The force and moment boundary conditions were also identical to those prescribed in Section 4.5 and shown graphically in Figure 4.13.

The results as a function of shaft angle are shown in Figure 4.17. The maximum 1st principal stress has a maximum value of 38,675 psi occurring at 2°, while having a minimum of 32,149 psi at 220°. Figure 4.18 provides a graphical illustration showing the orientation of the discharge pressure force vector at 0°. Positive angular values are CCW rotations, while negative angular values of CW rotations. The numerical simulation results versus shaft angle in Figure 4.17 also reveal that roughly at the angular location where the maximum 1st principal stress occurs the minimum occurs for the equivalent plastic strain. And, when the maximum 1st principal strain is at its minimum the equivalent plastic strain is roughly at its maximum. This is due in part because when the

1st principal stress values are at their maximum the tensile stress is acting to increase the seal drive pin hole diameter, thereby reducing the amount of radial interference between the pin and the drilled hole. This subsequently reduces the radial compressive stress and thus the corresponding plastic deformation is reduced. However, when the maximum 1st principal stress is at its minimum the equivalent plastic strain is approximately at its maximum due to the reduced tensile stresses around the pin hole. The reduced tensile stresses serve to maintain the seal drive pin hole's original shape, thereby maintaining the high compressive stresses due to the interference fit.

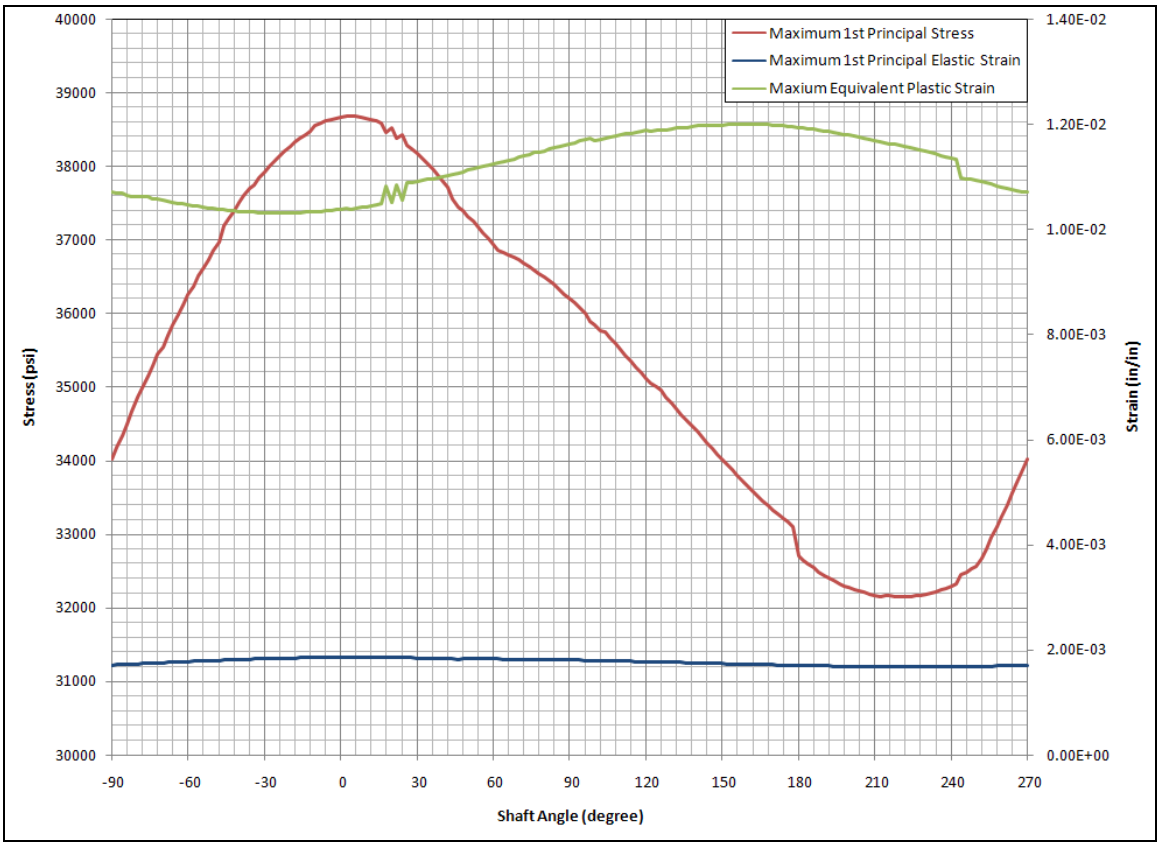

Figure 4.17: Numerical Simulation Results as a Function of Shaft Angle

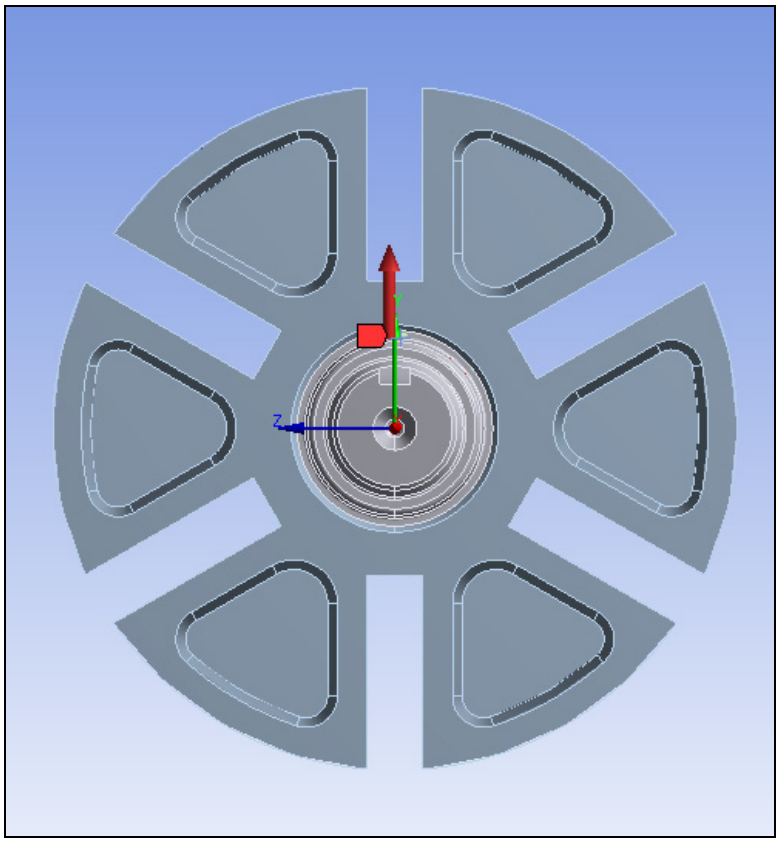

Figure 4.18: Illustration of Angular Reference for Numerical Simulation. The Vertical Red Arrow Shown Corresponds to 0°.

Figures 4.19 and 4.20 are 1st principal stress plots of the seal drive pin hole at a shaft angle of 2° when the principal stresses are highest. The peak 1st principal stress value is 56,176 psi and is seen to occur not on the outer surfaces of the shaft but within the interior of the shaft. When comparing this peak 1st principal stress value to the endurance limit established for this material it appears fatigue within the region of the seal drive pin would be likely. Figures 4.21 and 4.22 are plots of the stress acting in the direction of the pump shaft axis or the global X direction. The peak magnitudes of the axial stress are approximately the same as the 1st principal stress values shown in Figures 4.19 and 4.20. This indicates that within the region of the seal drive pin hole the

maximum 1st principal stresses act normal to the typical crack face associated with fatigue failures of this shaft.

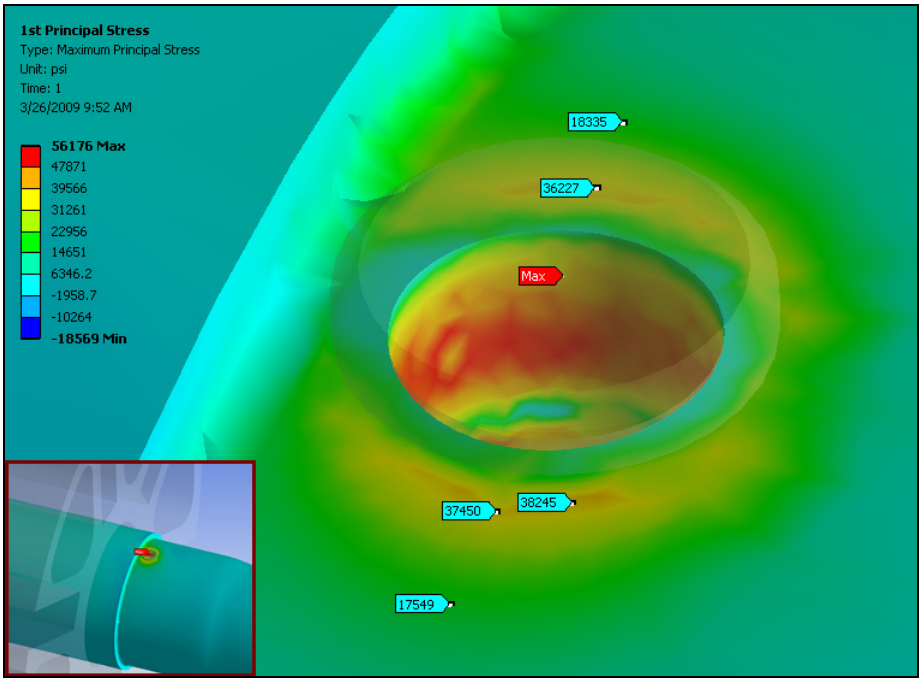

Figure 4.19: Plot of 1st Principal Stresses of Seal Drive Pin Hole Isometric View

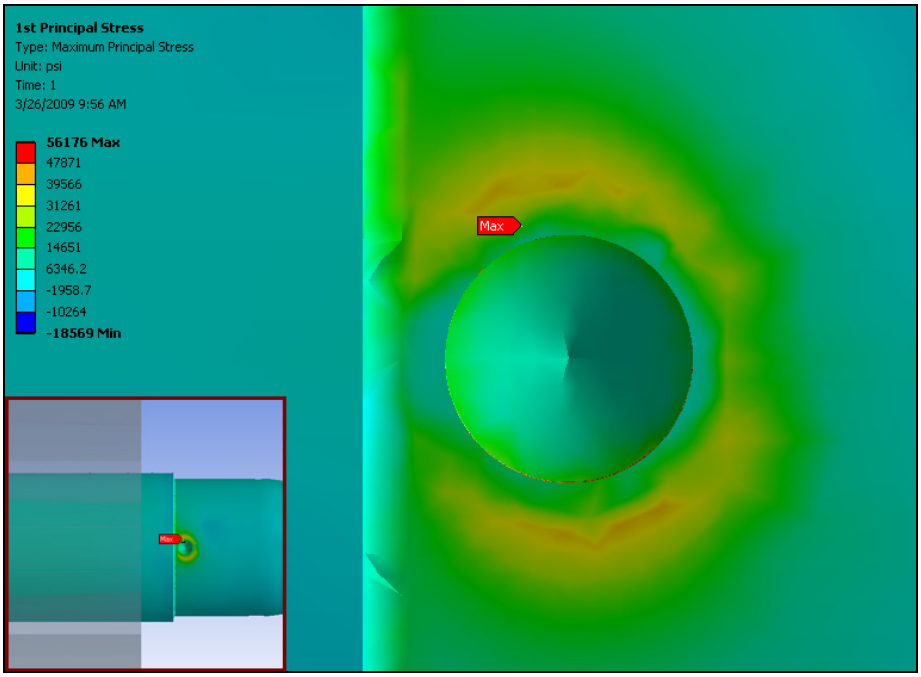

Figure 4.20: Plot of 1st Principal Stresses of Seal Drive Pin Hole Top View

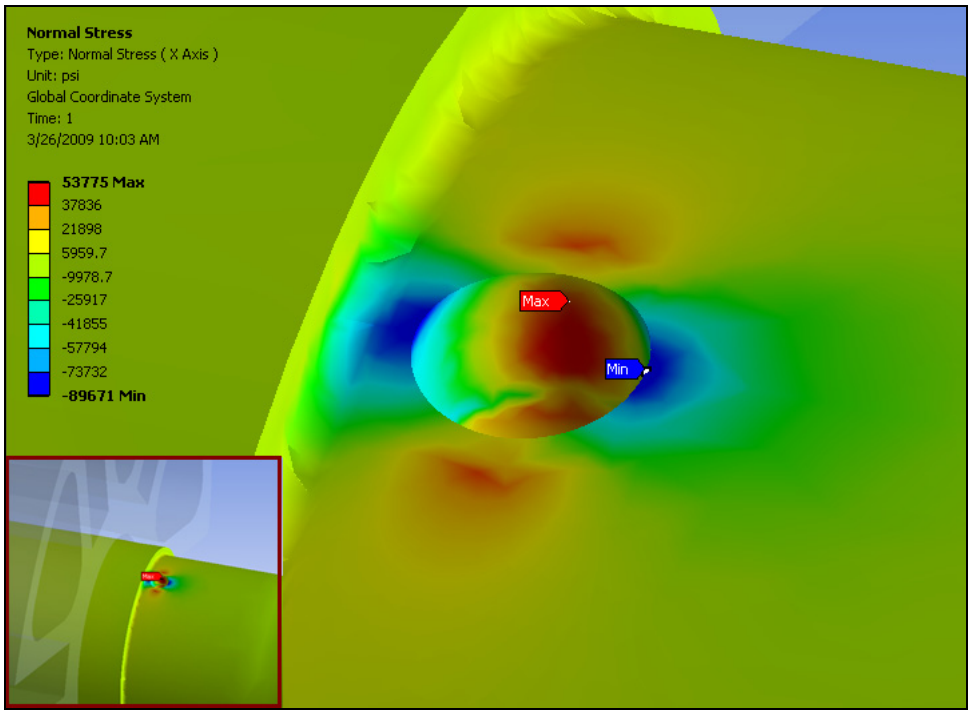

Figure 4.21: Plot of Axial Stresses Near the Seal Drive Pin Hole Isometric View

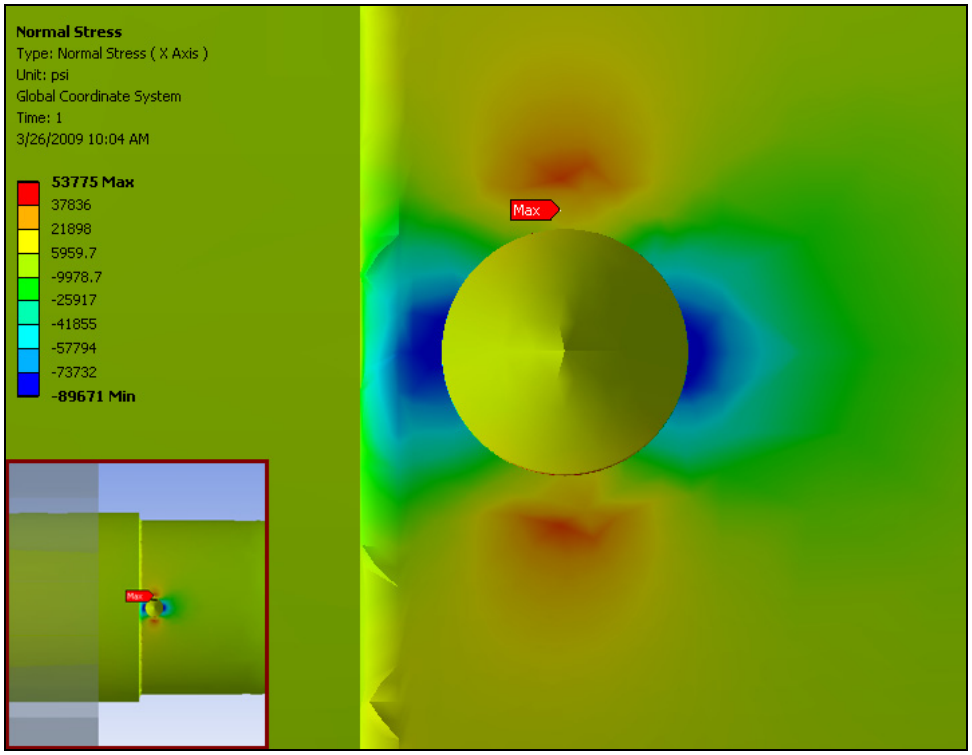

Figure 4.22: Plot of Axial Stresses Near the Seal Drive Pin Hole Top View

CHAPTER V

RESULTS AND OBSERVATIONS

The experiments that have been conducted can be compared to their numerical simulation counterpart in order to determine if the numerical models accurately represent the structural response they intend to characterize. If the results stemming from the numerical simulation models reasonably represent the true structural response of the pump shaft then those numerical models may be used to gain better insight into the entire stress and strain distribution throughout the entire pump shaft and could possibly be used to predict the structural response due to alternative loading scenarios. In addition, an accurate numerical simulation model may assist in developing a complete understanding regarding the stress state of the Z4500 pump shaft so that a possible determination into the root cause of the intermittent shaft failures can be made.

Even if the experimental results vary greatly from the numerical simulation results insight can still be achieved. These deviations between theoretical numerical simulation results and experimental results could reveal the existence of alternative or additional physical phenomena that may have not been previously considered.

5.1 Press Fit Experimentation and Simulation

The press fit experiments described in Chapter III were an attempt to physically observe the effects the interference fit of the seal drive pin into the pump shaft. Numerical simulations of this interference fit described in Chapter IV appeared to correlate well with the observed results stemming from experimentation. Figure 5.1 provides a side-by-side comparison of the deformed seal drive pin hole to a simulation results contour plot of the equivalent plastic strain.

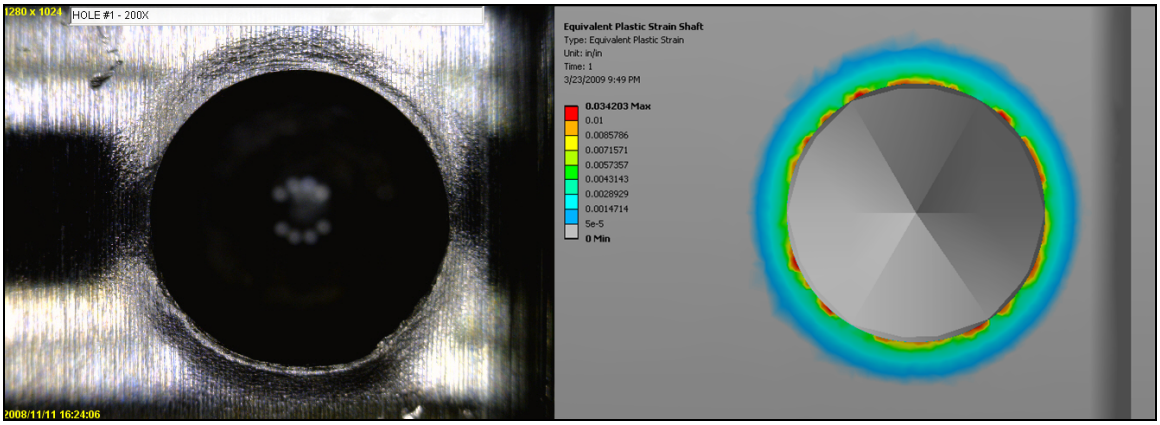

Figure 5.1: Press Fit Results Comparison

While the numerical simulation model did well modeling the general plastic deformation that occurred around the perimeter of the seal drive pin hole, the simulation model was not able to simulation the surface wrinkling that occurred. To have a numerical simulation model that would be capable of modeling plastic deformation of that nature would most likely require an extremely fine mesh. Figure 5.2 provides a side-by-side comparison of the deformed pin hole with surface wrinkling to the corresponding numerical simulation mesh.

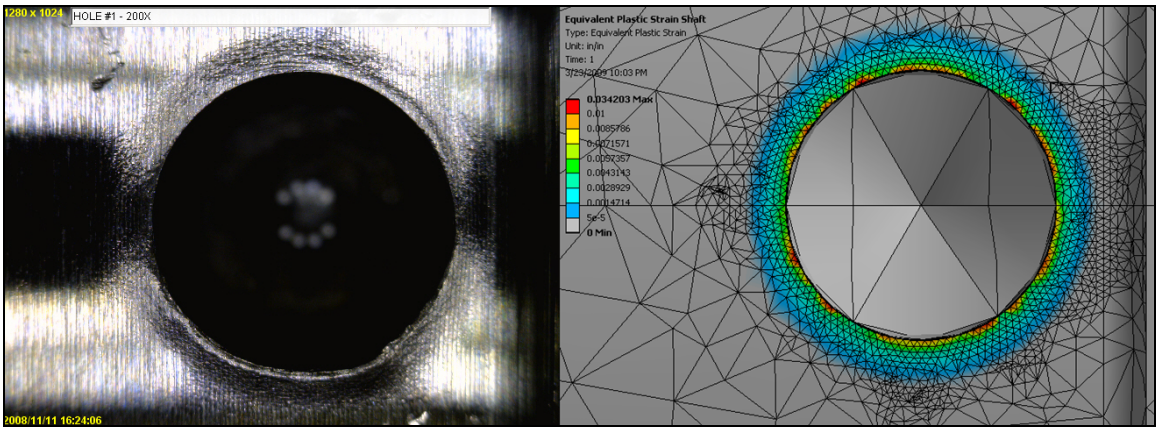

Figure 5.2: Actual Plastic Deformation Compared to Simulation Model Mesh

In addition, it is not immediately clear as to why the radial compressive plastic deformation around the perimeter of the seal drive pin hole appears to be minimized in the locations that coincide with the shaft axis as shown in Figures 3.5 and 3.7. The numerical simulation model results indicate that plastic deformation will occur, yet the photographs taken during experimentation do not appear to correlate.

It is perceived that the absence of plastically deformed surface wrinkles as shown in Figures 3.5 and 3.7 are the product of radial compression with respect to the pump shaft axis stemming from contact between the outer circumference of the shaft and the underside of the seal drive pin head during the press fit operation. It is believed that this compressive force acts to flatten the surface wrinkles after they have been formed during the initial penetration of the pin into the shaft.

While the interference fit is considered a static load the effect it has on the fatigue life is perceived as being detrimental. The fact that plastic deformation is occurring around the hole presents the opportunity for crack or void formation both on the surface and within the interior. In addition, the presence of the interference fit serves to increase the mean stress of any alternating load where it is known that any increase in mean stress

or R value according to equation 2.1 increases the fatigue crack propagation rate. Finally, an examination of the elastic stress field that exists beyond the immediate perimeter of the hole shows 1st principal stresses on the order of 35,000 psi to 45,000 psi acting normal to the typical crack face associated with fatigue failures of this shaft. This tensile stress is above the minimum fatigue limit previously established in Section 4.3 thereby indicating the likelihood of fatigue damage.

However, it must be noted that the numerical simulation model modeled the interference between the seal drive pin and the shaft as being the nominal 0.001 inches radially. Due to production tolerances the actual radial interference can vary from 0.000 inches to 0.002. The fact that the radial interference can vary from no interference to a maximum of 0.002 inches radially may explain the intermittent nature of the shaft failures. Additionally, it was described in Section 3.2 and shown in Figure 3.14 where shearing of the seal drive pin itself can occur during the press fit operation thereby reducing the diameter of the pin and subsequently reducing the magnitude of the interference fit. This shearing of the pin phenomenon could also contribute to the intermittent nature of the pump shaft failures through a wide variation in both stress and plastic deformation.

5.2 Pump Shaft Structural Response Experiments and Simulation

Chapter III described a series of experiments utilizing a strain gauge rosette and telemetry hardware to measure the structural response of the Z4500 pump shaft under typical operating conditions. Chapter IV described a set of numerical simulation models which attempted to model the structural response of the pump shaft based on pressure and

torque data acquired during the previous experimentation. Figure 5.3 provides a graphical overlay of the experimentation results at 100 RPM and 125 psi pump discharge pressure originally shown in Figure 3.41 with the numerical simulation results originally shown in Figure 4.13. The solid graph lines shown in Figure 4.13 are plots of the actual acquired data, while the dashed lines represent the results from the numerical simulation model.

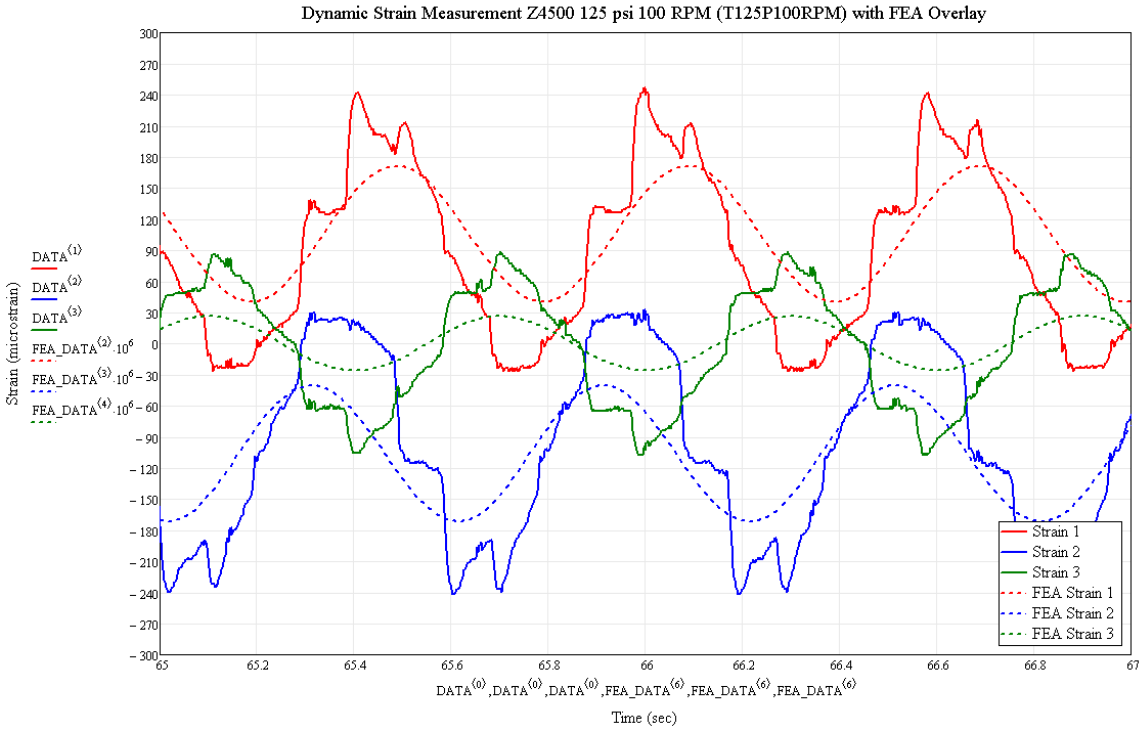

Figure 5.3: Overlay of Experimental and Numerical Data

Since the angular position of the shaft was not acquired simultaneously with the strain gauge measurements, the numerical simulation data had to be fitted to the experimental data by phasing the time scale of the numerical simulation data set. The fitting process was performed on strain gauge 3 data set (reference Figure 3.19 for gauge layout), given that the gauge 3 experimental data had fewer sharp data spikes combined

with lower magnitudes. Figure 5.4 provides an overlay of just the gauge 3 experimental data with the gauge 3 numerical simulation data.

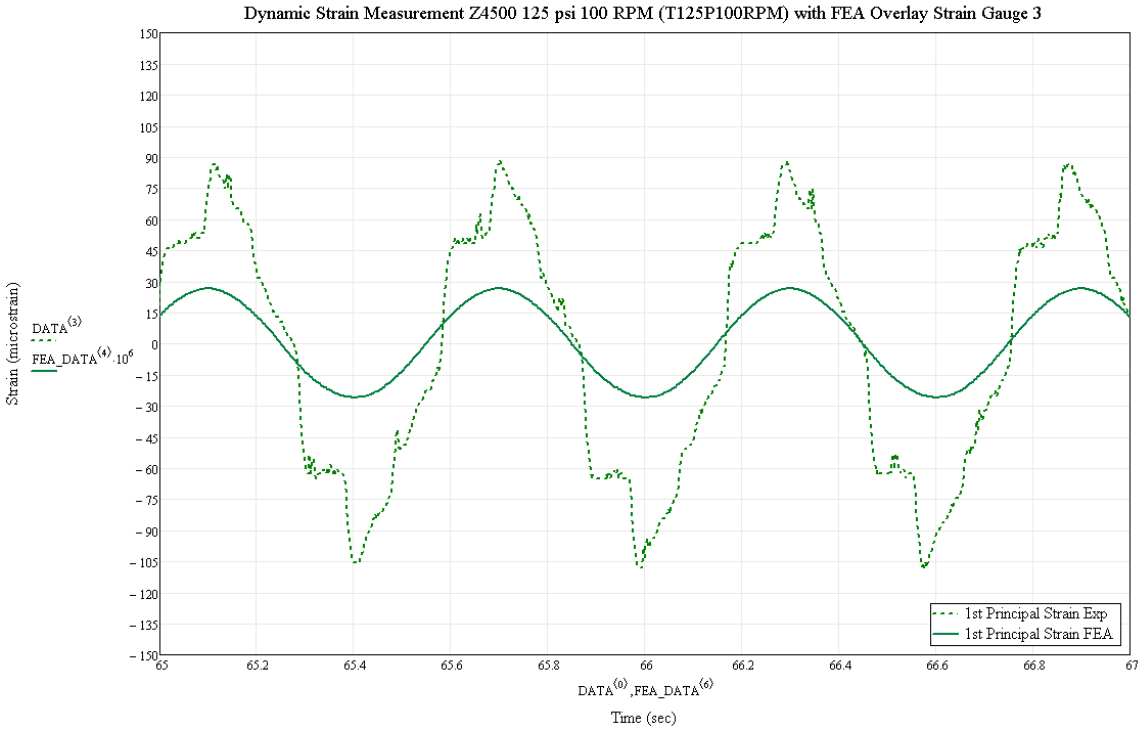

Figure 5.4: Overlay of Gauge 3 Experimental and Numerical Data

In Figure 5.4 the experimental data exhibits an appreciable amount of deviation from the numerical simulation model data throughout several rotational cycles. Abrupt changes in both the positive and negative direction occur periodically on all three gauge measurements, however the largest magnitudes are associated with gauge 1 and gauge 2 measurements (see Figure 3.19 for gauge layout). It is also noted that the abrupt changes are periodic in nature and very repeatable.

Treating the surface of the shaft where the strain gauge rosette is mounted as a two dimensional region in an effort to examine the response of each of the individual grids within the rosette can be performed. Figure 5.5 provides a graphical illustration of

the effect axial tensile and compressive strains have due to large shaft bending loads. Based on the rosette layout in Figure 3.19 and the rosette placement in Figure 3.22 it can be seen that large tensile strains will result in an increase in strain for gauges 1 and 2, but will result in a reduction in strain for gauge 1. Likewise, axial compressive strains due to shaft bending loads will result in a decrease in strain for gauges 1 and 2, while increasing the strain on gauge 3.

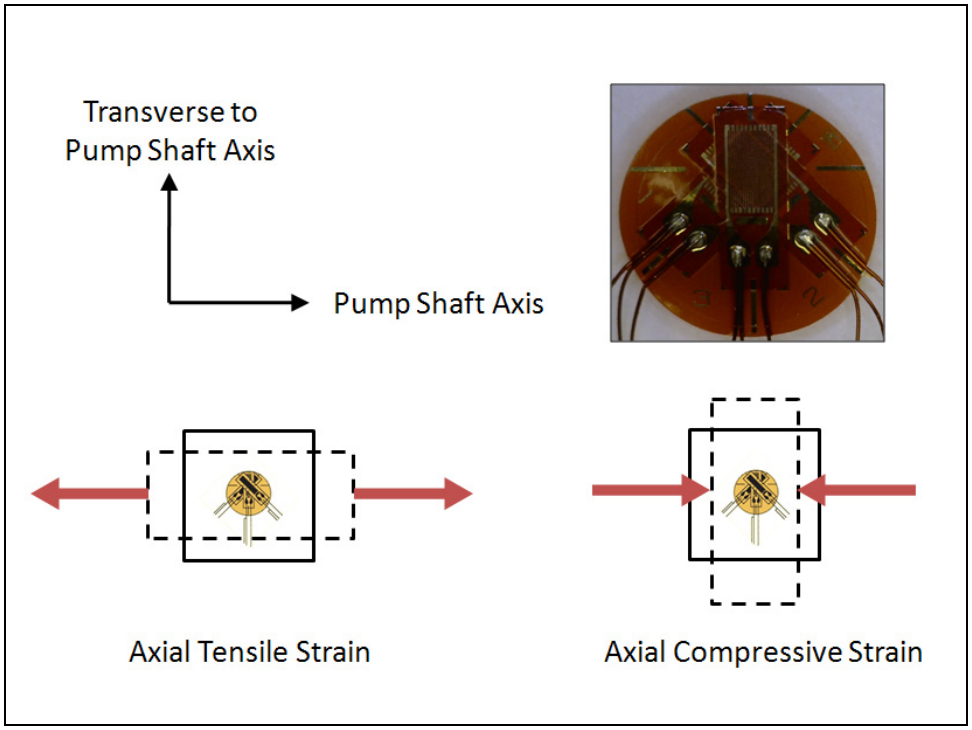

Figure 5.5: Graphic of Axial Tensile and Compressive Strains

Once again treating the surface of the shaft as a two dimensional region where the strain gauge rosette is mounted, an examination into the response of each individual grids to torsional shearing strains can be performed. Figure 5.6 provides a graphically illustration of the effect torsional shear strains will have. Based on the rosette layout in Figure 3.19 and the rosette placement in Figure 3.22 it can be seen that torsional shearing strains in the direction of normal rotation of the pump as illustrated will produce

increased strain on gauge 1, while decreasing the strain on gauge 2. Theoretically, gauge 3 will be insensitive to torsional strains; however, in practice some positive or negative straining could occur due to slight gauge misalignment with the axis of the shaft.

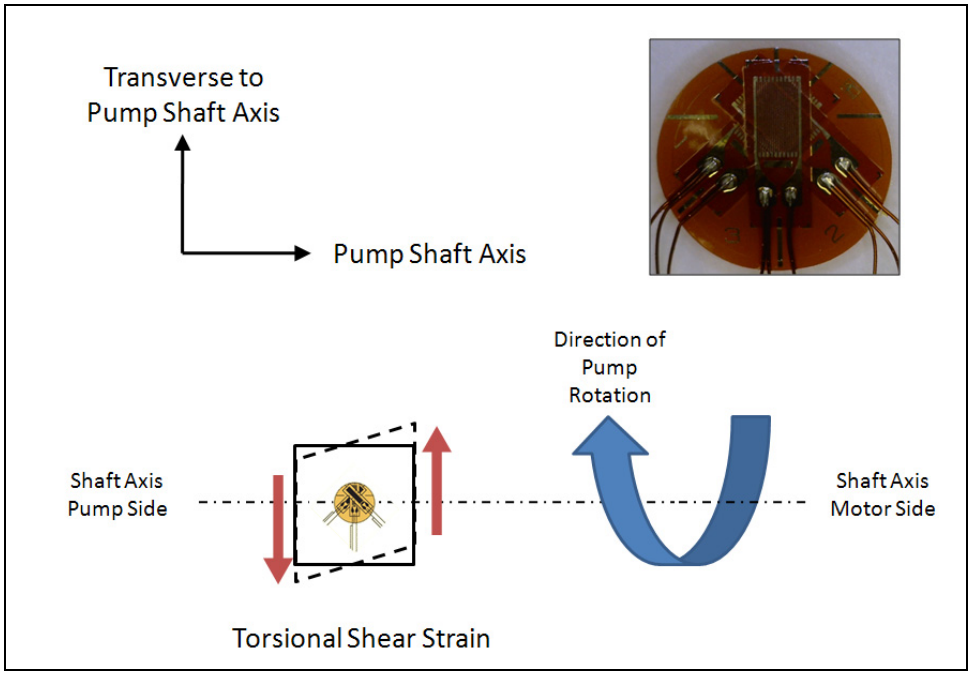

Figure 5.6: Graphic of Torsional Shear Strains

Table 5.1 provides the tabularized form of the individual strain grid responses to torsional, tensile, or compressive loading.

Loading Scenario	**Strain Gauge 1**	**Strain Gauge 2**	**Strain Gauge 3**
Torsional	Increase	Decrease	No Effect
Tensile	Increase	Increase	Decrease
Compressive	Decrease	Decrease	Increase

Table 5.1: Individual Gauge Response to Various Loading Scenarios

Figures 5.7 and 5.8 provide illustrations of where sudden changes in the experimental strain gauge data occurred. Applying the knowledge the affect both bending stresses and shearing stresses will have on the strain gauge rosette bonded on the pump shaft, it can be seen that the sharp increases and decreases in the measured strains on all three gauges corresponds to a sudden simultaneous increase in both bending and torsional strains. The main contributing factor regarding the direction of the sudden change in strain readings pertained to the compressive or tensile nature of the bending stresses with respect to the mounted strain gauge as it relates to the rotational angle of the shaft at the time the increase in bending and torsional stress occurred. It is also observed that these sudden increases and decreases in strain reading occurred periodically six times per revolution, which corresponds to the number of vanes within the pump.

The sudden increase and decrease in the measured strains, which subsequently resulted in increases in 1st principal stains and stresses, is believed to be associated with possible liquid compression within the pump. The basis for this assertion stems from the fact that the sudden change in strain readings occur six times per revolution, which corresponds to the number of pump vanes. Based on the strain data acquired, the sudden change in all three gauge readings are consistent with a sudden increase in combined torsion and bending. Finally, the pump discharge experimentation results described in Section 3.3 showed not only a mean pressure difference between the pumping chamber and the pump discharge, but also small pressure oscillations at a rate of 6 per revolution.

Therefore, it is perceived that liquid compression is likely occurring within the pump which would result in sudden and dramatic increases in internal pressure, subsequently increasing both the bending and torsional loads on the pump shaft. Liquid

compression within the pump would most certainly serve to decrease the fatigue life of the shaft. However, due to the sensitivity of the increase in bending and torsional loading on the pump shaft to the average pump discharge pressure as shown during experimentation in Section 3.5, a case could be made ascertaining that the effects from liquid compression contribute to the overall intermittent nature of the pump shaft failures due to widely varying customer applications where pump discharge pressure requirements vary as well.

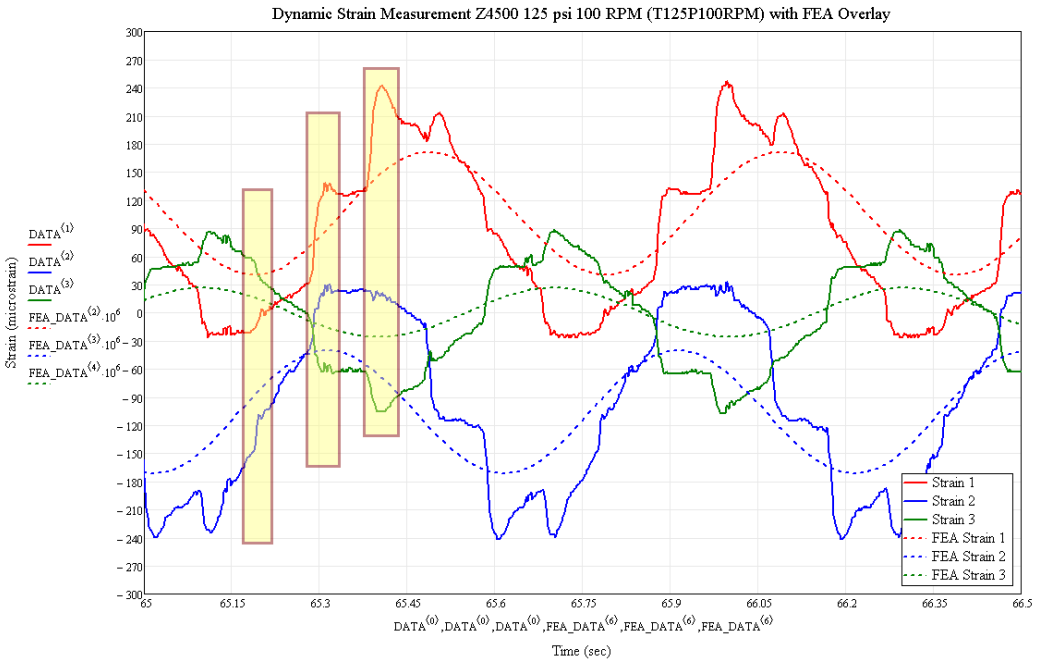

Figure 5.7: Regions of the Experimental Data Associated with Combined Positive Bending Strain and Torsional Strain with Respect to Gauge Location

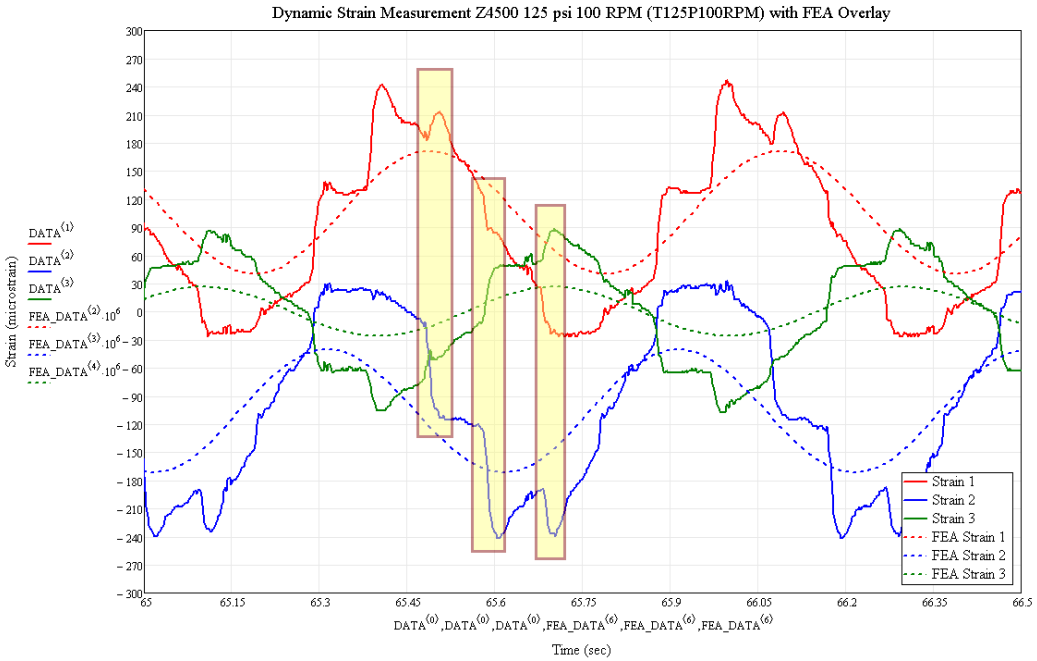

Figure 5.8: Regions of the Experimental Data Associated with Combined Negative Bending Strain and Torsional Strain with Respect to Gauge Location

5.3 Total Stress Numerical Simulation Model Results

Results stemming from the numerical simulation model of the total peak stress of the rotor/shaft assembly indicated that the 1st principal stresses near the region of the seal drive pin hole exceed the minimum fatigue limit established in 4.3 and at certain locations both on the surface and in the interior of the shaft the 1st principal stresses exceeded the upper fatigue limit as well. Figure 5.9(a) provides the 1st principal stresses above the minimum fatigue strength of 33,100 psi, while Figure 5.9(b) provides the 1st principal stresses above the maximum fatigue strength of 54,000 psi.

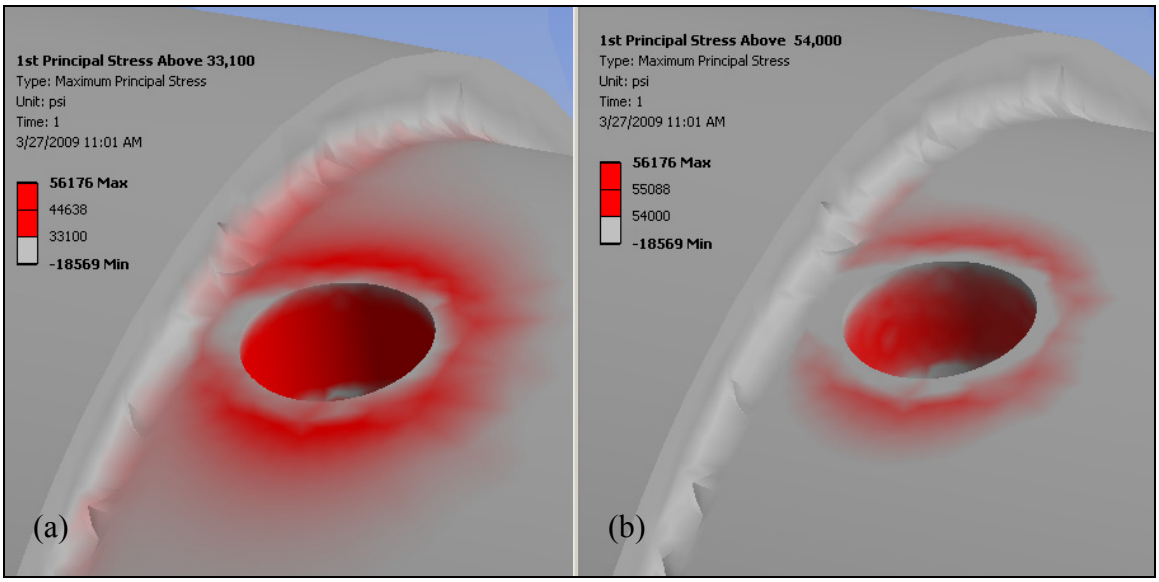

Figure 5.9: Fringe Plot of the 1st Principal Stresses (a) Above 33,100 psi and (b) Above 54,000 psi

Figure 5.9 illustrates a significant region around the seal drive pin hole is in a state of stress that has a high likelihood of fatigue failure. It must also be noted that the load boundary conditions modeled for this numerical simulation were nominal bending and torsional loading. The numerical model did not take into account any increase in both bending and torsional loading due to the occurrence of liquid compression. Therefore, the stress results presented in Figure 5.9 could be considered to have a lower magnitude than the actual stresses the pump shaft would be subjected to. Based on the results stemming from the total stress numerical simulation model, it is perceived that fatigue failure would be likely based on a combination of stresses due to the interference fit of the seal drive pin, bending and torsional stress during operation, and shrink fit of the rotor onto the shaft. However, actual bending/torsional loads and interference fit stresses will vary greatly. Thus, the likelihood of fatigue failure could vary greatly as well due to

stress state variations, which would also be a contributing factor to the intermittent nature of the pump shaft failures.

CHAPTER VI

CONCLUSION

6.1 Conclusions

The purpose of this study was to examine the stress state of the Corken Z4500 pump shaft during normal operating conditions to gain insight regarding the structural response of the shaft. In addition, the results stemming from the research conducted were to be used to assist in determine a possible root cause to intermittent shaft failure. Both laboratory experiments and numerical simulations were performed in order to examine the distribution and concentration of stresses and strains within the pump shaft. Based upon the research conducted the following conclusions can be made:

1. Interference fit of the seal drive pin into the shaft plays a key role in both the fatigue failure of the shaft and the intermittent nature of the shaft failures. Research showed the interference fit of the pin resulted in localized plastic deformation in the shaft, which served to reduce the fatigue life of the shaft due mechanical damage, and that the interference fit increased the stress field surrounding the seal drive pin hole, which served to raise the mean stress in an alternating stress environment, thereby reducing the fatigue life of the shaft.

Variations in manufacturing tolerance of both the seal drive pin hole and the seal drive pin itself introduced variations regarding the magnitude of the interference fit, thereby subsequently resulting in large variations in plastic deformation and the surrounding stress field. It was also shown that occasional shearing of the seal drive pin during the press fit operation can occur, thereby reducing the outer diameter of the pin and the subsequent plastic deformation and surrounding stress field.

2. Operation of the pump at the upper range of discharge pressures can introduce situations where pump shaft fatigue may become an issue. Due to combined loading from the pump discharge resulting in torsional and bending stresses with the large stresses due to the interference fit of the seal drive pin, pump shaft stresses can exceed the endurance limit of the shaft material. However, a large amount of variance exists pertaining to the peak shaft stresses due to varying magnitudes of interference between the seal drive pin and the shaft as well as varying end user applications of the pump where discharge pressures differ.

3. Liquid compression most likely is occurring within the positive displacement swept vane pump, which serves to reduce the overall fatigue life of the pump shaft and introduces a new degree of variability with respect to fatigue life of the shaft. Research has shown the presence of sharp increases in bending and torsional strains at a rate per revolution which matches the number of vanes within the pump. In addition, research has also shown a mean pressure difference

between the pump discharge pressure and the pump chamber pressure. Research also showed a strong dependence of the sharp increases in bending and torsional loads on the magnitude of the discharge pressure as opposed to the rotational speed of the pump.

6.2 Future Work

Since research showed that the seal drive pin played a key role in the fatigue life of the shaft, more work is needed in developing alternative designs which possibly eliminate the need for the seal drive pin entirely or reduce the magnitude of the stress resulting from the interference fit. While alternatives in seal designs could be explored where these designs would not required the use of a seal drive pin, most mechanical seal designs in use today throughout industry require some form of mechanical linkage between the seal assembly and the rotating pump shaft.

More work is also needed to explore further the possibility of liquid compression within this swept vane pump design. The particular cam design used within the Z4500 pump used during this study is present in other pump designs at Corken. Additional experimentation would need to be conducted to see if the signs of liquid compression exist in other pump designs. Furthermore, additional research would be needed to explore possible design alternatives that minimize or eliminate any possibility for liquid compression within the pump.

REFERENCES

1. F. Berndt, A. van Bennekom, Pump shaft failures -- a compendium of case studies, Engineering Failure Analysis, Volume 8, Issue 2, April 2001, Pages 135-144.

2. Xu Xiaolei, Yu Zhiwei, Failure analysis of a locomotive turbocharger main-shaft, Engineering Failure Analysis, Volume 16, Issue 1, January 2009, Pages 495-502.

3. A. m. Lancha, M. Serrano, D. Gomez Briceno, Failure analysis of a condensate pump shaft, Engineering Failure Analysis, Volume 6, Issue 5, October 1999, Pages 337-353.

4. A. M. Lancha, M. Serrano, J. Lapena, D. Gomez-Briceno, Failure analysis of a river water circulating pump shaft from a NPP, Engineering Failure Analysis, Volume 8, Issue 3, June 2001, Pages 271-291.

5. Fractography, ASM Metals Handbook, Volume 12, 9th Edition, American Society for Metals, 1987.

6. K. D. Thompson, S. D. Sheppard, Fatigue crack growth in notched and plain shafts subjected to torsion and axial loading, Engineering Fracture Mechanics, Volume 43, Issue 1, September 1992, Pages 55-71.

7. E. W. Smith and K. J. Pascoe, Fatigue crack initiation and growth in a high-strength ductile steel subject to in-plane biaxial loading, Multiaxial Fatigue, ASTM STP 853, 111-135 (1985).

8. M. Madia, S. Beretta, U. Zerbst, An investigation on the influence of rotary bending and press fitting on stress intensity factors and fatigue crack growth in railway axles, Engineering Fracture Mechanics, Volume 75, Issue 8, May 2008, Pages 1906-1920.

9. M. Madia, S. Beretta, U. Zerbst, An investigation on the influence of rotary bending and press fitting on stress intensity factors and fatigue crack growth in railway axles, Engineering Fracture Mechanics, Volume 75, Issue 8, May 2008, Pages 1906-1920.

10. A. Carpinteri, R. Brighenti, A. Spagnoli, Surface flaws in cylindrical shafts under rotary bending, Fatigue and Fracture of Engineering Materials and Structures, Volume 21, Issue 9, September 1998, Pages 1027-1035.

11. D. A. McClure, Shaft Analysis Metallurgical Report, Report Number 1082540, August 2008.

12. G. Beckwith, R. Marangoni, J. Lienhard V, Mechanical Measurements, 5th Edition, Addison-Wesley Publishing Company, 1993, Pages 506-516.

13. E. Oberg, F. Jones, H. Horton, H. Ryffel, Machinery's Handbook, 25th Edition, Industrial Press Inc., 1996, Pages 1399-1416.

14. R. Hertzberg, Deformation and Fracture Mechanics of Engineering Materials, 4th Edition, John Wiley & Sons, Inc, 1996.

15. R. I. Stephens, A. Fatemi, R. R. Stephens, H. Fuchs, Metal Fatigue in Engineering, 2nd Edition, John Wiley & Sons, Inc, 2001.

16. Corken, Inc., Z4500 Installation and Operation Manual (ID105G), June 2006.

17. Atlas of Fatigue Curves, 1st Edition, ASM International, 1986.

18. Properties and Selection: Irons, Steels, and High-Performance Alloys, ASM Metals Handbook, Volume 1, 10th Edition, American Society for Metals, 1990.

APPENDICES

Appendix A.1 LabView Pump Pressure Test Program

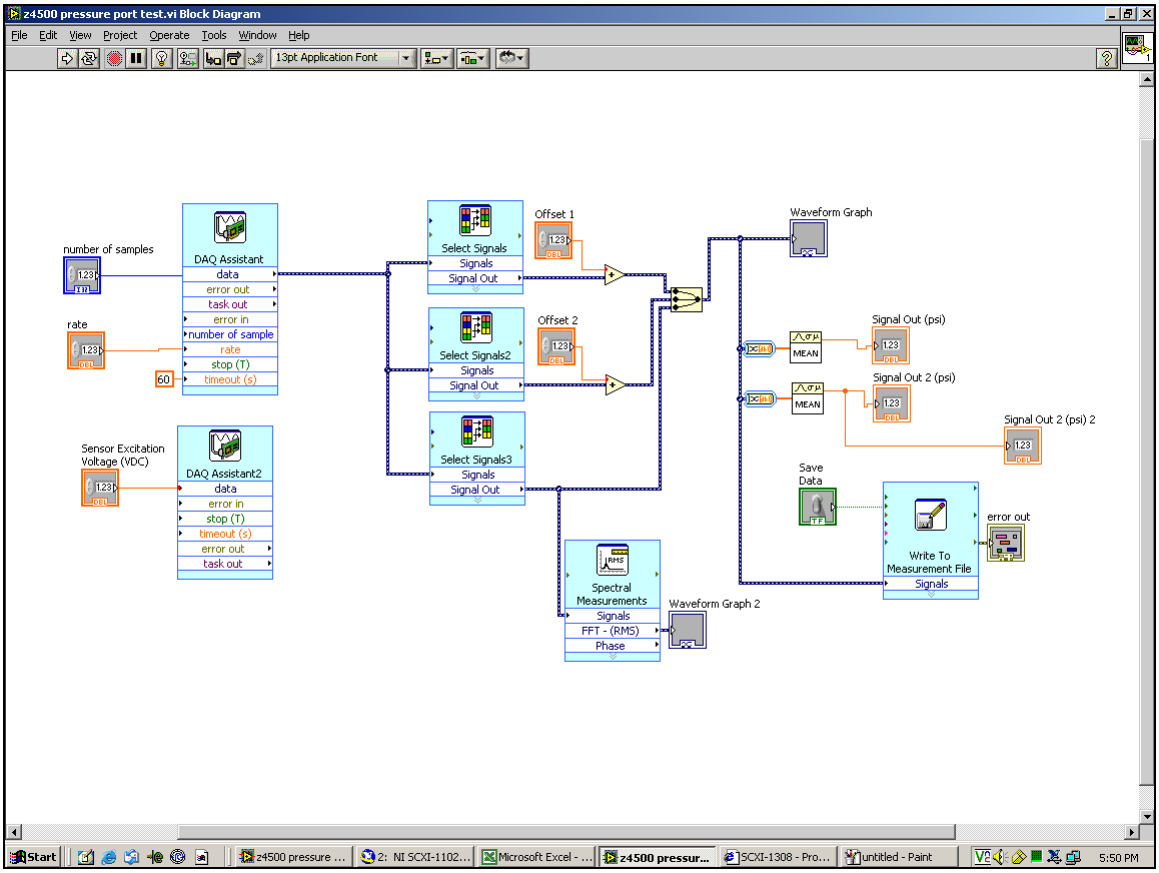

Appendix A.2 LabView Pump Pressure Test Program – Front Panel

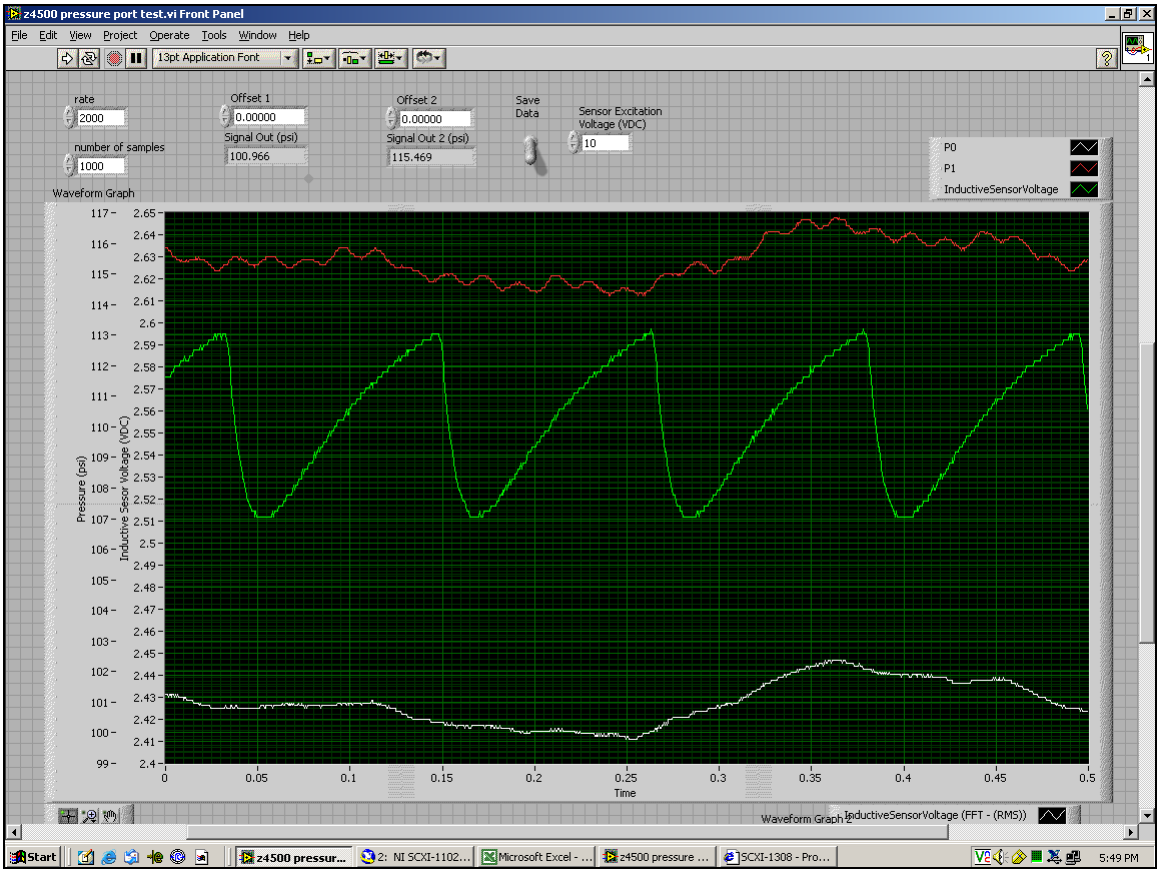

Appendix B.1 LabView Shaft Strain Program

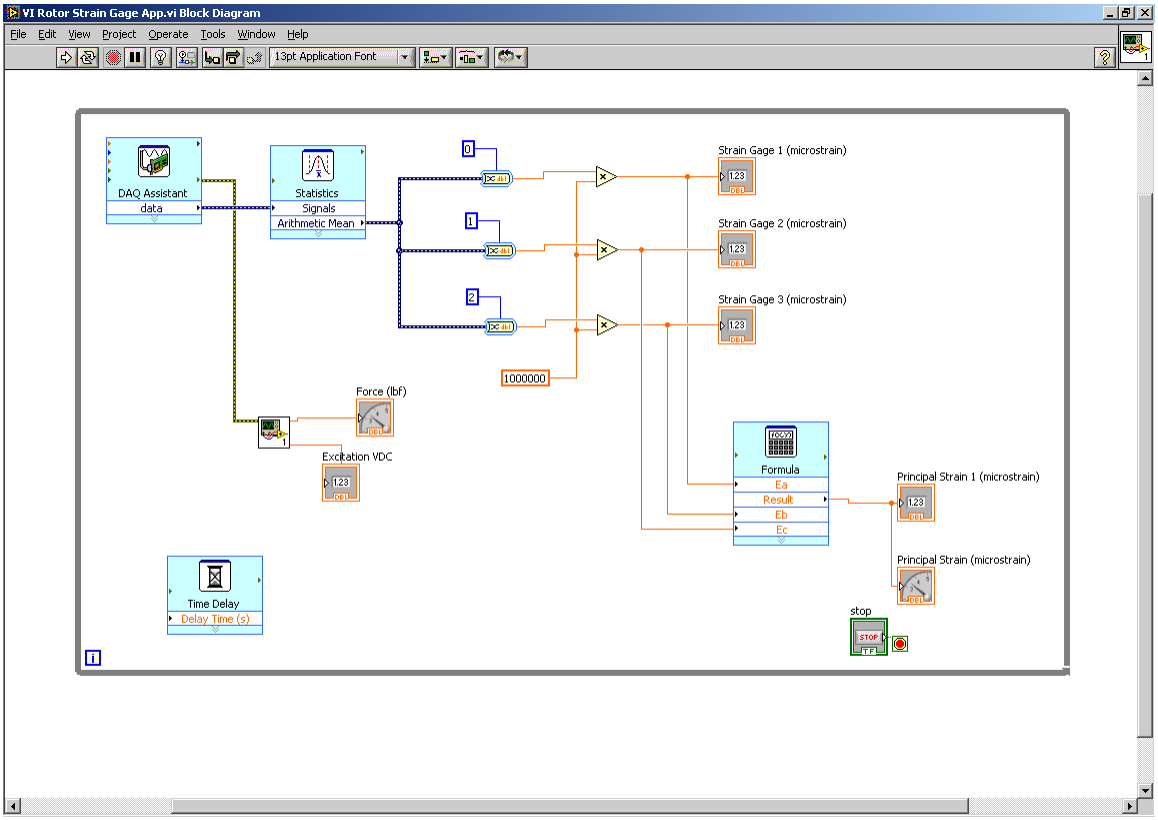

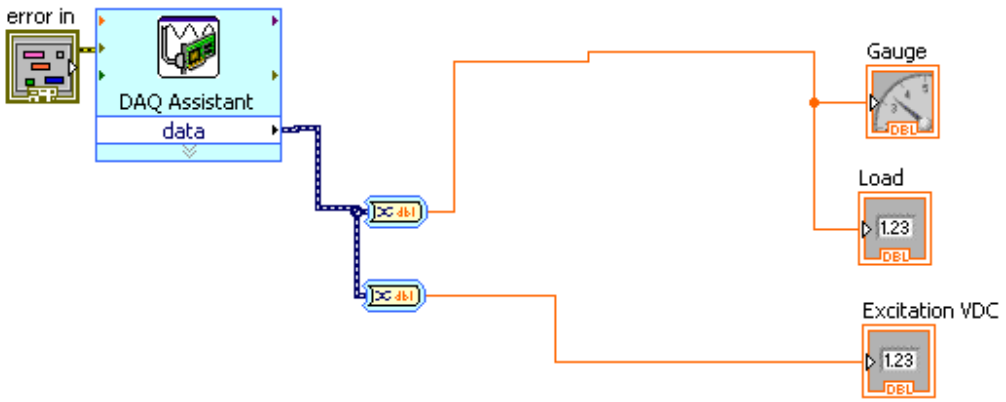

Appendix B.2 LabView Shaft Strain Program – Front Panel

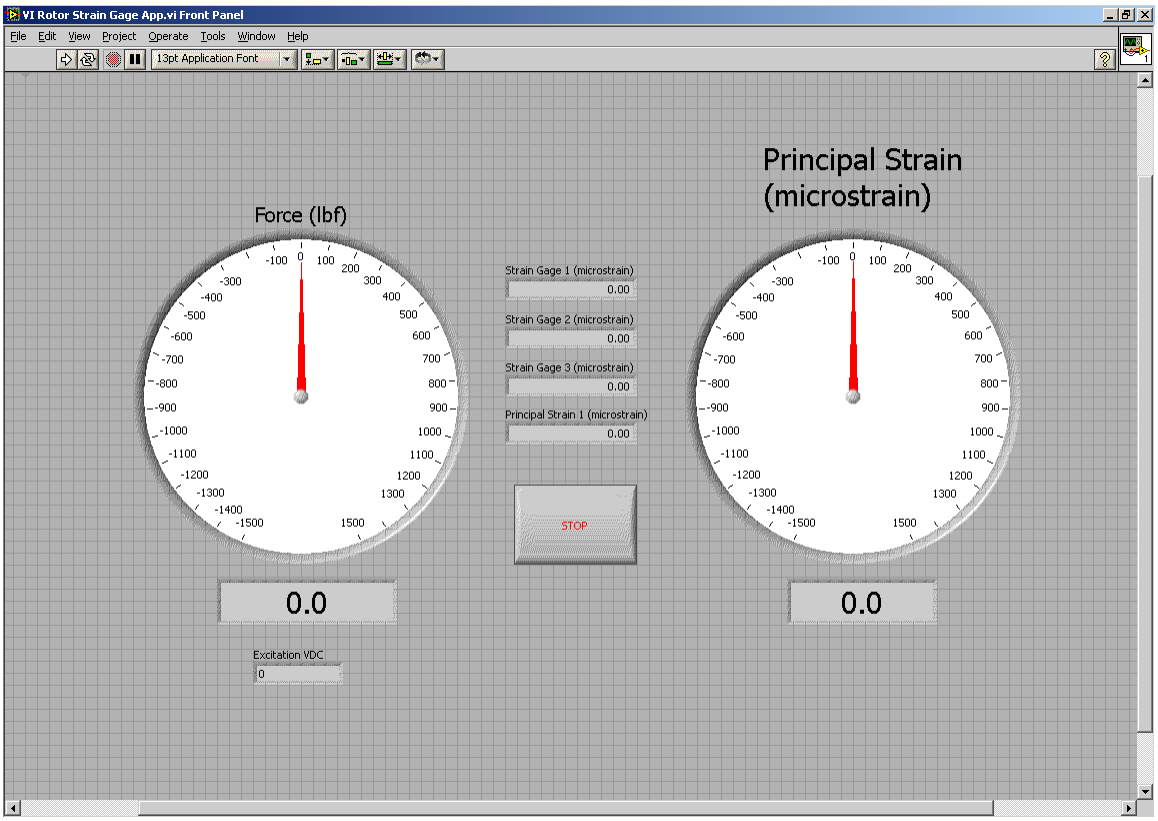

VITA

Stephen Seymour

Candidate for the Degree of

Master of Science

Thesis: SLIDING VANE PUMP SHAFT STRUCTURAL RESPONSE AND INTERMITTENT FAILURE INVESTIGATION

Major Field: Mechanica Engineering

Biographical:

Personal Data: Born in Tulsa, Oklahoma on October 15, 1976. Married to Toni Hill on September 7, 2002. First son Logan Stephen Seymour born October 13th, 2007. Second son Lucas Daniel Seymour to be born August 7th, 2009.

Education:
Graduated from Bishop Kelly High School in Tulsa, Oklahoma May 1995; received Bachelor of Science in Mechanical Engineering Technology from Oklahoma State University, Stillwater, Oklahoma, in December 2000; completed the requirements for the Master of Science in Mechanical Engineering at Oklahoma State University, Stillwater, Oklahoma in May 2009.

Experience: Design Engineer, Fluid Technologies Inc., 1998-1999; Design Engineer, MerCruiser, 1999-2001; Design Engineer, International Environmental Corp., 2001-2002; Design Engineer, Corken Inc., 2002-2004; Project Engineer, MerCruiser 2004-2006; Project Engineer, Corken Inc., 2006-present

Professional Memberships: Licensed Professional Engineer in the state of Oklahoma (PE# 23092)

Name: Stephen Seymour Date of Degree: May, 2009

Institution: Oklahoma State University Location: Stillwater, Oklahoma

Title of Study: SLIDING VANE PUMP SHAFT STRUCTURAL RESPONSE AND INTERMITTENT FAILURE INVESTIGATION

Pages in Study: 118 Candidate for the Degree of Master of Science

Major Field: Mechanical Engineering

Scope and Method of Study: The objectives of this study were to examine the structural response of a swept vane pump shaft subject to normal operational loading and use the results obtained from laboratory experimentation and numerical simulations to determine possible root cause pertaining to intermittent structural failure. Microscopic and SEM photographs were taken to examine the effects of the seal drive pin press fit operation on the pump shaft. Dynamic measurements of the pump discharge and pump chamber pressure were acquired at a high sample rate to study the pressures the pump shaft would be subjected to. Dynamic strain measurements of the pump shaft during the operation of the pump were also gathered through the use of telemetry data acquisition hard. Numerical simulation models involving both elastic and plastic deformations were created to simulate the press fit operation, the dynamic strain measurement experiments, and to examine the total stress when all applicable loads and interferences were applied.

Findings and Conclusions: Research concluded that the interference fit between the seal drive pin and the pump shaft resulted in an appreciable amount of plastic deformation pertaining to the pump shaft and also resulted in levels of stress that were approaching the endurance limit of the material. Subsequent numerical simulation models that included all applicable loads and interference fits revealed stress levels that exceeded the endurance limit of the material. However, all experimentation and numerical simulation models were conducted on geometry at the nominal design dimensions. Tolerance analysis revealed a wide range of interference between the seal drive pin and the shaft, which would result in dramatic changes in the amount of plastic deformation and the magnitudes of the surrounding stresses. The press fit operation was perceived as being a major source of variability, which would contribute to the overall intermittent nature of the pump shaft failures. In addition, results stemming from the pump discharge/pump chamber pressure testing and the dynamic strain measurement experimentation revealed the presence of liquid compression, which serve to increase the levels of stress and reduce the overall serviceable life of the pump shaft.

ADVISER'S APPROVAL: Dr. J. K. Good